Synergistic Approach to the Stable Production of Solar Fuels by Coupling Urea Oxidation with Hydrogen Generation

by

Rong Zhao

A dissertation submitted to the Graduate Faculty of
Auburn University
in partial fulfillment of the
requirements for the Degree of
Doctor of Philosophy

Auburn, Alabama

December 15, 2018

Approved by

James Radich, Chair, Assistant Professor of Chemical Engineering
Robert Ashurst, Associate Professor of Chemical Engineering
Bruce Tatarchuk, Professor of Chemical Engineering
Bart Prorok, Professor of Material Engineering

Abstract

A solar waste-to-fuels concept was presented to synergistically produce hydrogen fuel from visible sunlight while remediating urea wastewater. A cascade semiconductor-catalyst electrode assembly was designed to drive the photoconversion of urea to hydrogen. Proper band energy alignment facilitates catalyst activation *via* hole transfer across the semiconductor-catalyst interface. Specifically, CdS-sensitized TiO_2 with $Ni(OH)_2$ urea electrocatalyst on fluorine-doped tin oxide (FTO) coated glass was employed as the photoanode. The steady-state response of the semiconductor-catalyst electrode was investigated in a photoelectrochemical cell, and charge transfer and recombination kinetics were elucidated to identify limiting charge transfer reactions within the electrode architecture. Back electron transfer from semiconductor to catalyst was found to be competitive with the urea oxidation reaction, which hindered steady-state photoconversion efficiency. Furthermore, the photoanode rapidly decomposed in urea electrolyte solutions due to the water-mediated photocorrosion of chalcogenide electrodes.

Photocorrosion of photoelectrodes is an issue limiting the application of semiconductors. Thin dielectric layers ZnS and SiO_2 were employed to reduce photocorrosion and improve performance of photoelectrodes. ZnS and SiO_2 were deposited onto CdS to study the photostability and performance of this system. ZnS and SiO_2 thin layers were deposited on TiO_2-CdS photoelectrodes by successive ionic layer absorption and reaction (SILAR) and sol-gel methods, respectively. The photocurrent stability of CdS with ZnS and SiO_2 improved 4 and 3

times respectively compared to bare CdS. Transient absorption results showed slower bleach and absorption decay due to reduced trap-mediated recombination when ZnS or SiO_2 was present on CdS photoelectrodes. Higher charge transfer resistance in the presence of ZnS or SiO_2 was indicated from electrochemical impedance measurements. Tafel plots showed that the photocorrosion current decreased 55% for ZnS-coated CdS and 63% for SiO_2-coated CdS compared to bare CdS.

Charge kinetics and photoresponses of TiO_2-CdS photoelectrodes were dependent on the CdS nanoparticle size. The non-radiative recombination and electron transfer rate reduced with increased CdS nanoparticle size. The photocurrent density increased 4 times when SILAR cycles of CdS increased from 3 to 9, and then decreased with increased SILAR cycles. The stability of photocurrent improved with increased CdS nanoparticle size.

The effect of solvent on charge kinetics in CdS quantum dots (QDs) were investigated. Inorganic Na_2SO_4 aqueous solution and organic DMSO were employed to dissolve urea. The transient absorption spectroscopy measurements showed that, the lifetime of electrons and holes in CdS was shortest in vacuum, followed by in inorganic Na_2SO_4 and longest in organic DMSO. Fluorescence and transient absorption spectroscopy measurement results indicated that urea could passivate CdS surface states and donate electrons to CdS. Polarity and viscosity of the electrolyte affected charge kinetics. Hole transfer rate constant from CdS to urea in Na_2SO_4-urea solution was 10 times of that in DMSO-urea solution.

Acknowledgments

I would like to give my great gratitude and appreciation to my academic advisor, Dr. James G. Radich for his guidance and support throughout my doctoral study.

I also thank my committee members, Dr. Robert Ashurst, Dr. Bruce Tatarchuk and Dr. Bart Prorok for their professional advice and kind help. Thank Dr. Zhongyang Cheng for being the university reader of my dissertation.

I appreciate my labmates Animesh Mondal, Rohit Kanungo and Fatima Hamade for their discussions and collaborations.

I would like to express my special gratitude to my parents. Thanks for having my back.

Thank all people who helped me.

Table of Contents

List of Tables

List of Figures

Chapter 1 Introduction

1.1 Motivations and Objectives

To solve the energy crisis and environment pollution, the overall objective of this project is to realize simultaneous urea oxidation and hydrogen generation in a hybrid photoelectrochemical (PEC) reactor by employing visible-light absorbing semiconductors and urea oxidation catalysts. As urea, a major component of urine, is used as the source to produce hydrogen by solar-driven method, this project produces clean energy from waste water by employing inexhaustible solar energy.

One objective of this research is to solve a critical issue in PEC reactors: photocorrosion of light absorbing semiconductors. Semiconductors with straddled conduction and valence band positions relative to the water reduction and oxidation potentials have been used for solar-driven water splitting for decades. However, the photocorrosion is kinetically favorable compared to water oxidation at the semiconductor-electrolyte interface, which deteriorates the performance of the PEC reactor. This research focuses on CdS due to its visible-light absorption ability, tunable optoelectronic properties, facile preparation method and well- known photophysical and photochemical behaviors. Dielectric barrier layer (DBL) is proposed to be deposited on the semiconductor surface to prevent the direct contact of semiconductor and electrolyte to suppress the photocorrosion in semiconductors. CdS is a n-type semiconductor, the photogenerated holes will diffuse to the semiconductor-electrolyte interface upon photoexcitation. The blocking of direct contact of CdS and the electrolyte will prevent the water-mediated anodic corrosion. In

addition, the dielectric layer is sufficiently thin, which promotes spatial separation of electrons and holes and reduce the interfacial electron-hole recombination.

Another objective of this research is to probe the charge transfer kinetics as a function of DBL thickness, CdS QDs size, and pH value of the electrolyte in the semiconductor-catalyst photoelectrodes to determine the most beneficial material interface parameters for promoting charge transfer and suppressing recombination. This research incorporates semiconductor TiO_2 as the mesoscopic acceptor for photosensitizer CdS, DBL and urea oxidation catalyst $Ni(OH)_2$ to promote simultaneous urea oxidation and hydrogen generation. Various electron and hole transfer and recombination rates are measured at interfaces such as TiO_2-CdS, CdS-DBL, DBL-electrolyte and $Ni(OH)_2$-electrolyte. The valence and conduction band positions of CdS can be influenced by the quantum confinement effect, that is, the band positions will change with the size of CdS nanocrystals when their radii are less than Bohr exciton radius. The band positions of CdS relative to the acceptor species represent a thermodynamic driving force for charge transfer. The band offset between donor (i.e. CdS) and acceptor (i.e. $Ni(OH)_2$) will determine the driving force for charge transfer, and this driving force can be modulated by changing the size of CdS nanocrystals within the quantum confinement regime. The pH value of the electrolyte can also affect the band positions of TiO_2 nanocrystals and hence change the driving force for charge transfer from CdS to TiO_2. The electron and holes transfer kinetics can also be influenced by the thickness of DBL. The obtained carrier dynamics can provide information of the competitive kinetic processes such as charge transfer and/or recombination within the system and hence provide guidance on the rational selection of suitable materials and structural design for a PEC system.

1.2 Background

Energy is a vital key element for the world in last 40 years and has significant effect on nature, society and economy.[1] According to Global Energy Statistical Yearbook 2018, the total energy consumption of the highest 3 countries exceeded 6000 million tonnes of Oil Equivalent in 2017, and the acceleration in energy consumption in 2017 was +2.3% compared to +1.1% in 2016. The demand for energy is increasing, however, the fossil fuels reserves are decreasing. It is urgent to find renewable and clean energy as alternatives to fossil fuels.

Hydrogen is a potential candidate for an alternative source of energy. It is clean, efficient, and can be derived from various resources, containing fossil fuels, nuclear energy and renewables such as biomass, hydro, wind, solar and geothermal. Hydrogen can be used as a direct energy source in transport such as automobiles, as power sources in homes and as feedstock for the industry. Hydrogen is naturally abundant on Earth in both organic and inorganic compounds such as hydrocarbons and water, therefore, hydrogen can be produced from these hydrogen-containing substances. For example, currently the most used industrial process for hydrogen production is water electrolysis. This method employs an electrolyzer unit to decompose water to produce hydrogen. This method is energy-consuming as it needs electricity. Hydrogen can also be obtained by thermal decomposition of water, however, the process is energy-consuming too, as the temperature needs to be higher than 2500 K.[2] Today, approximately 96% of the global hydrogen production is based on steam reforming of fossil fuels.[3] Economical methods are the prerequisite for sustainable hydrogen production. Several possible ways for sustainable hydrogen production are under investigation, including fermentation of biomass,[4] thermochemical processes,[5] photobiological water splitting[4] and PEC water splitting.[6] Of which, the hydrogen production from a PEC cell gains most attention as the

energy source it uses is inexhaustible solar energy. Solar energy that can be captured and utilized on Earth is enormous. About 3.9 $\times 10^{24}$ MJ incident solar energy is received on Earth's surface every year, which is about 10000 times more than current global energy consumption. Thus, even only 1% of solar energy is absorbed, it is enough to meet all human energy needs.[7]

Of all sources to produce hydrogen, urea is gaining attention due to its nature of wastewater. If hydrogen is produced from urea, not only the clean energy is obtained, the wastewater is degraded. Urea has a gravimetric hydrogen content of 6.71 wt%.[8] More importantly, it is a major component of urine. Urine is the most abundant waste on Earth. About 11 millions of tons of urine are produced every day. Urea available in these urines is about 500 times more than the market need of 0.5 Mt every day. Urine is considered as a wastewater that bring environmental issues such as nitrate contamination of ground water and soil. It is economical and environment-friendly to produce hydrogen from urea in urine.

Steam reforming of urea was first reported in 2010.[8] Nickel was employed as the catalyst and simple hydrogen rich synthesis gas was obtained. A method to produce hydrogen from a urea production plant was also reported in 2010. Nickel-alumina catalyst bed and palladium membrane was combined, and 4588 tons per year hydrogen was produced and at the same time, the environmental issue of the urea plant was solved.[9] In 2009, a research reported that hydrogen could also be produced by electrolysis of urea alkaline solution by employing $Ni(OH)_2$ as the catalyst. In 2010, a direct urea fuel cell was reported.[10] Urea is therefore considered for both indirect hydrogen storage and direct fuel cell supply. In 2012, urea and urine were reported to produce hydrogen in a PEC cell without external bias by employing TiO_2 and α-Fe_2O_3 as photoelectrode and $Ni(OH)_2$ as catalyst,[11] starting the new chapter of hydrogen production from urea by solar energy.

1.3 Photoelectrochemical Cells

1.3.1 Principles

Photoelectrochemical (PEC) cells are liquid-junction solar cells that utilize a photoelectrode consisting of semiconductors to convert light energy into electricity.[12–14] There are 3 steps in a PEC device needed to convert light energy into electrical current: (1) light absorption in the photoelectrode, (2) generation, separation and transport of photogenerated electrons and holes, (3) reduction and oxidation reactions in electrolyte. Upon photoexcitation, semiconductors generate electrons and holes.[15] The minority carriers are transported toward photoelectrode-electrolyte interface to drive a redox half-reaction, and the majority carriers are transported toward the counter electrode via external circuit to drive the other redox half-reaction. For n-type semiconductors, holes are the minority carriers, and they are transferred across the photoelectrode-electrolyte interface to drive oxidation reactions. For p-type semiconductors, electrons are the minority carriers, and they drive reduction reactions at the photoelectrode-electrolyte interface. The simplest PEC device consists of a photoelectrode made of one semiconductor and an electrolyte. Photoelectrodes consist of multiple semiconductors, catalysts and conduction layers are more frequently used to maximize the light absorption and overall PEC performance. A schematic illustration of PEC is shown in Figure 1-1.[16,17]

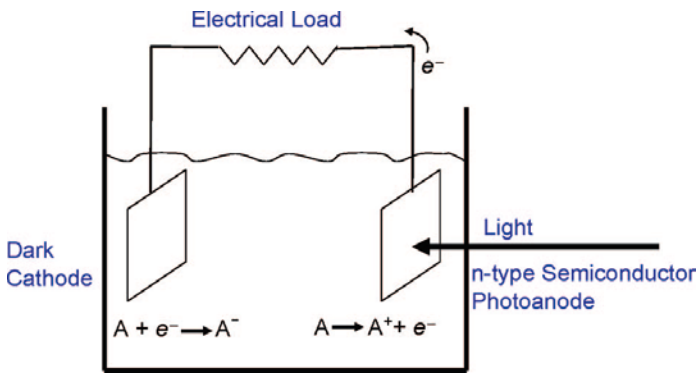

Figure 1-1. Schematic illustration of a photoelectrochemical cell to convert light energy into electricity. This figure is reprinted from reference 16.

1.3.2 QDs-sensitized Photoelectrodes

Solar cell technologies have evolved into 3 generations. The first generation is based on a single crystalline semiconductor wafer. The second generation is based on inorganic thin films. They are cheaper to produce but the efficiency is lower than the first generation. The third generation is emerged to reach a higher efficiency at a lower cost, such as dye-sensitized solar cells (DSSCs) and quantum dots-sensitized solar cells (QDSSCs). Low- cost and high-efficiency solar cells were first introduced as dye-sensitized solar cells with inorganic ruthenium-based dyes in early 90s.[18] From then on, extensive researches have been focused on the development and characterization of different dyes for application in DSSCs, such as nature dye materials[19] and synthetic organic dyes.[20] Based on the DSSC's structure, QDs were first introduced as a replacement of dye due to its excellent opto-electronic properties and facile QDs fabrication methods.[21–32]

QDs sensitizers have many advantages compared to dye sensitizers.[33–35] First, semiconductor QDs can absorb light with energy equal to or larger than their bandgap, which means one QDs sensitizer can absorb a wide range of solar spectrum,[36] while one dye sensitizer usually has a narrow absorption band.[37] Second, dyes absorb on mesoporous substrate by

monolayer, while multilayer QDs can be deposited, which extends light absorption.[38] Charges are then transported through the thin film of QDs.[39–41] Third, the tunable light absorption properties of QDs are highly desirable for specialty solar cell design. The quantum confinement effect enables a variety of unique optoelectronic properties and is applicable to very small nanocrystals with a single spatial dimension less than the Bohr radius/length.

Appropriate sequential size arrangement of QDs can absorb the entire solar spectrum and obtain higher electron transfer rates.[42] QDs can also transfer "hot" electrons.[43–45] "Hot" electrons and holes generate upon photoexcitation of QDs, and electrons transfer to the mesoporous metal oxide layer before "cooling," which can generate higher open circuit potentials. Finally, QDs exhibit multiple exciton generation,[46,47] where more than one pair of electron-hole pairs are generated upon absorption of a single photon.[48] Each of these unique characteristics can serve to enhance the conversion efficiency of photoelectrodes employed in a multitude of solar conversion applications.

Nanostructured semiconductor films have been employed in PEC devices to generate photocurrent.[49–51] DSSCs and QDSSCs were developed based on the nanostructure semiconductor film. A mesoporous wide band gap semiconductor layer on a conducting glass is used as the photoelectrode to attach QDs. Typically, TiO_2 is chosen as the mesoporous semiconductor. The mesoporous TiO_2 is coated with these QDs using colloidal QD or in situ fabrication.[52,53] Upon photoexcitation, semiconductor nanoparticles generate electrons and holes. Unlike single crystal semiconductor, nanoparticles are usually smaller than 10 nm that there is no space charge layer in which electrons and holes are separated. Nanostructured semiconductor assemblies like TiO_2-CdS separate charges via kinetics of the interfacial charge transfer reactions being faster than the recombination kinetics. Photogenerated holes are scavenged by the

electrolyte to drive the oxidation reaction, and electrons transport through the nanoparticles and reach the counter electrode via external circuit and drive the reduction reaction. TiO_2 is one of the most and earlies semiconductors researched in the form of suspensions,[54] nanostructured films[55] and dye and semiconductor QDs-sensitized solar cells. [56] Figure 1-2 takes QDs-sensitized TiO_2 as the example to schematically show the working principles of a PEC cell.[57]

To improve the charge separation, composite films with two or more semiconductors with appropriate band alignment are used to constitute the nanostructured photoelectrode, and QDs-sensitized photoelectrode is one type of composite films. The composite films have the staggered band alignment[58] as is shown in Figure 1-2 to facilitate the separation of electrons and holes, such as in TiO_2-CdSe QDs-sensitized photoelectrodes.[59] In staggered configuration, electrons will be injected into the lower lying conduction band of the large bandgap semiconductor, this is, TiO_2 in TiO_2-CdSe composite film, increasing the separation of electrons and hole. Besides, the light absorption range is expanded in staggered configuration since it consists of semiconductors with different bandgap. In addition, the high porosity and surface area of mesoscopic TiO_2 semiconductor films enables the incorporation of QDs such as CdS and CdSe[60–62] as well as increase the contact area of the photoelectrode with the electrolyte, and hence increase the light absorption. The staggered configuration has been extensively researched in past decades, containing metal chalcogenide-metal oxide such as CdS-TiO_2,[63,64] CdSe-TiO_2,[65–68] CdS-ZnO,[69–72] ZnSe-ZnO,[73] ZnO-ZnS,[74] CdS-SnO_2,[75–77] CdSe-SnO_2,[78–81] metal oxide-metal oxide such as SnO_2-TiO_2,[82,83] and metal chalcogenide-metal chalcogenide such as CdS-PbS.[84]

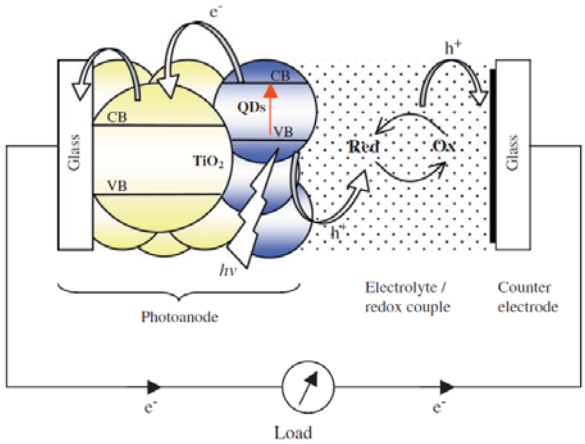

Figure 1-2. Schematic illustration of a photoelectrochemical cell consisting of QDs-sensitized photoelectrode. This figure is reprinted from reference 57.

1.3.3 Preparation of QDs-sensitized Photoelectrodes

Different preparation methods yield particles or films with different surface area, morphology and grain boundary density, which affect the performance of photoelectrodes. For example, high surface area films consisting of nanoparticles have high density of grain boundary, which increase electron and hole recombination.[85,86] Thus, various film preparation methods have been developed to achieve various functionalities. Generally, these methods can be divided into two categories: surface attachment through molecular linkers of ex-situ pre-synthesized colloidal nanoparticles and in-situ fabrication.

For ex-situ fabrication, QDs are pre-synthesized and adsorbed on the mesoporous semiconductor surface directly or by employing molecular linkers that have various functional groups. Before attachment of QDs on the electrode, QDs are first pre-synthesized in solution by employing capping agents. Capping agents are used to control the nanoparticle size and shape. The most used capping agents in QDs synthesis such as CdS and CdSe QDs are trioctylphosphine oxide (TOPO) and mercaptopropionic acid (MPA). QDs are usually washed several times before attachment after synthesis. The electrode is then immersed in a solution of

QDs containing bifunctional molecular linkers, one functional group of the linker attaches onto the electrode surface and the other attaches to the QDs. The functional linker molecules are employed for assisting dispersion and stabilization of the QDs.[87] The advantage of the ex-situ fabrication is the controllability of the QDs particle size. The drawback is that it typically takes anywhere from a few hours to a few days to attach the QDs onto the electrode, greatly lengthening the fabrication time.

In situ fabrication is the most used method to deposit QDs on mesoporous semiconductors. This technique is facile and cost-effective and can be used in large scale production. Chemical bath deposition (CBD) and successive ionic layer adsorption and reaction (SILAR) are the most used technique for in-situ deposition. CBD deposits QDs in solution and involves nucleation and particle growth. In a typical process of CBD, cationic and anionic are separately prepared and then placed together to form the bath deposition solution. The electrode is then immersed in the bath, slow reactions occur and QDs are deposited on the electrode. The amount of QDs deposited can be controlled by immersion time, bath temperature, pH of the solution and concentration of reactants. Various QDs such as CdS and CdSe have been successfully deposited on semiconductors.[88] The main disadvantage of this technique is the wastage of bath after every deposition.

SILAR is a subclass of CBD. SILAR is fast, reproducible and less expensive. In SILAR method, QDs are in-situ deposited on mesoporous semiconductor with wide band gap. TiO_2 is the most used mesoporous semiconductor in QDs-sensitized photoelectrode. In a typical preparation, TiO_2-coated photoelectrode is first dipped into the cationic precursor solution for a certain time, followed by rinsing and drying. The photoelectrode then is dipped into the anionic precursor solution followed by rinsing and drying. The two-step dipping is regarded as 1 cycle of

SILAR. The size of the deposited QDs on TiO_2 can be controlled by the number of SILAR cycles. This method has been used to synthesize CdS, CdSe and CdTe onto TiO_2 films. CdS-sensitized electrodes have been prepared using SILAR for a long time because the precursors Cd^{2+} and S^{2-} are simple and stable in air. For example, successively immersing a TiO_2 film in Cd^{2+} and S^{2-} solutions will get a thin film of CdS nanocrystals. The color changes from light yellow to orange with increased SILAR cycles, indicating the formation of CdS on TiO_2. Compared to ex-situ preparation method, SILAR gives a larger distribution of particle size.[89] SILAR is especially useful to fabricate electrodes with coupled or multicomponent films. Several layers of semiconductor film with staggered band alignment and co-sensitization can be easily fabricated by SILAR. This sequential band alignment ensures efficient light absorption, electron and hole separation and extension of electrons and holes lifetime, which makes high efficiency of QDSSCs.

1.3.4 Corrosion of Photoelectrodes

The durability, reliability, and robustness of photoelectrodes are key factors for advancing large-scale production of economical solar cells. However, 3 types of corrosion can take place at the photoelectrode-electrolyte interface: chemical, electrochemical, and photoelectrochemical.[90] Chemical corrosion of semiconductors is due to chemical interactions with the surrounding environment and does not involve charge transfer across the semiconductor-electrolyte interface, and this type of corrosion can occur without irradiation. For example, corrosion of silicon occurs in alkaline media.[91] Electrochemical and photoelectrochemical corrosion both require net charge transfer across the semiconductor-electrolyte interface. For the electrochemical corrosion, majority charge carriers are involved in corrosion reactions. For the photoelectrochemical corrosion, photoexcited minority charge

carriers, that is, holes in n-type semiconductor, electrons in p-type semiconductor, are involved in corrosion reactions. The photoelectrochemical corrosion is one of the biggest issues limiting the performance of photoelectrochemical cells.

For a n-type compound semiconductor MX (M = Cd, Zn, Ga, Ti, X = S, Se, Te, N, etc.) used as the photoanode for water splitting, the valence band maximum (VBM) should be lower than the water oxidation potential. However, the photogenerated holes may oxidize the semiconductor itself, the so-called photocorrosion, leading to the decomposition of the semiconductor (Figure 1-3):[92]

$MX + zh^+ \rightleftharpoons M^{z+} + X$

Similarly, the photocathode will be reduced by photogenerated electrons:

$MX + ze^- \rightleftharpoons M + X^{z-}$

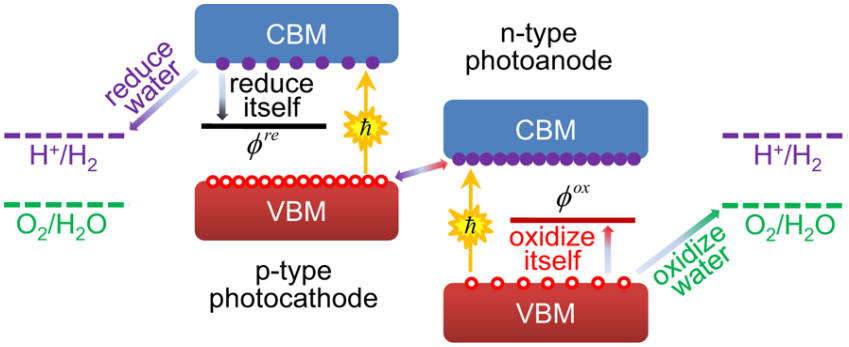

Figure 1-3. Schematic representation of the band alignment of the p-type and n-type photoelectrode relative to the water redox potentials. ϕ^{ox} and ϕ^{re} represents the oxidation potential of the photoanode and reduction potential of the photocathode in aqueous solution, respectively. This figure is reprinted from reference 92.

For most semiconductors, the photocorrosion products are non-photoactive. The insoluble products form a thin layer on the photoelectrode surface, which hinders the photoelectrode light absorption and charge transfer at the photoelectrode-electrolyte interface.

The thin layer formation leads to deterioration in the performance of the PEC cell.[93] Continuous photocorrosion leads to the accumulation of insoluble products and dissolution of ions, which destroy the photoelectrode and induce failure of the PEC cell. In order to maintain the stability of the photoelectrode, the cathodic decomposition potential of the semiconductor should be less positive than the reduction potential, that is, $E(H^+/H_2)$ in water splitting, and the anodic decomposition potential of the semiconductor should be more positive than the oxidative potential, that is, $E(O_2/H_2O)$ in water splitting,

Researchers[92] have revealed that all commercial non-oxide semiconductors have the tendency to the anodic corrosion, and only a few can resist the cathodic corrosion. For example, Young[94] showed unmodified GaAs photocathodes were stable for a maximum of 120 h in 3 M sulfuric acid. Oxide semiconductors are usually stable against cathodic decomposition, but only a few of them such as TiO_2, $BiVO_4$ and Co_3O_4 are stable against anodic decomposition.[92] Some semiconductors can maintain good stability regardless of photocorrosion. For example, Zhou[95] showed $Cu_2V_2O_7$ photoanode was stable in alkaline electrolyte. Even though the photocorrosion occurred, a passivation film was generated on the surface, which protected the photoanode. There is a critical thickness of the passivation film where the charge transfer resistance at the electrode-electrolyte interface reaches a point where the performance of the electrode is impacted. When the passivation layer is thinner than a critical thickness, the impact of the passivation layer on performance of the photoanode is not significant. However, if the passivation layer is thicker than a critical thickness, charge transport is prohibited, and recombination of electrons and holes increases because of vacancy defects, leading to the significant reduction of performance. Various kinetic factors need to be studied to reveal the dissolve rate of photoelectrodes. For example, addition of co-catalysts is one way to limit the rate and selectivity of the

photodecomposition.[96] However, it is noted that the degradation of the co-catalyst may accelerate the corrosion of photoelectrodes. Some researchers studied the passivation rate of photoelectrodes. For example, Lai *et al*[97] employed the scanning electron microscope (SEM) to study the kinetics of photodecomposition of the n-type GaAs photoelectrode-electrolyte $Fe_2(SO_4)_3/H_2SO_4$ interface. The results showed that the rate constant was 0.5-order dependent on the concentration of Fe^{3+}. They found that at low irradiation intensity, passivation formation was limited by the electrons and holes generated and transportation of charges to the photoelectrode-electrolyte interface, while at high irradiation intensity, it was limited by the mass transfer rate in the electrolyte. The research on the passivation formation rate can predict the lifetime of a PEC cell and help to improve the design of device.

1.3.5 Protection of Photoelectrodes

1.3.5.1 Hole or Electron Scavengers

Researches have shown that in semiconductors, different electron and hole transfer rates into the electrolyte will lead to the accumulation of one carrier within the film.[98,99] For instant, for n-type photoelectrodes, electrons accumulate in the semiconductor film in the presence of a hole scavenger, and accumulated electrons subsequently transport through grain boundaries to the conductive glass, and then transfer to counter electrode via external circuit. As the hole scavenger takes the holes, photooxidation by photogenerated holes will be significantly reduced or eliminated. Sacrificial redox scavengers such as halides,[100] EDTA,[101] $Fe(CN)_6^{4-}$,[102] $S^{2-}$and SO_3^{2-},[103] were employed to capture photogenerated holes and prohibit the photocorrosion. Besides, the recombination of electrons and holes is greatly reduced, and the efficiency of photocurrent is enhanced. Similarly, for those p-type photoelectrodes, the addition of electron scavenger will prevent the reduction of the semiconductor by photogenerated electrons.

1.3.5.2 Protective Layers

Techniques to Deposit Protective Layers

The deposition method will affect the uniformity, structural and electronic properties and hence influence the stability and performance of photoelectrodes.[104] Different thin film deposition techniques such as physical vapor deposition (PVD), chemical vapor deposition (CVD), atomic layer deposition (ALD), electrophoretic deposition (ED) and sol-gel have been employed to deposit protective films with high quality.[105,106]

PVD techniques, such as magnetron sputtering, thermal evaporation, electron-beam evaporation can control the thickness and composition of the protective film. The main disadvantage of this technique is that it may result in inhomogeneous deposition on structured semiconductor surfaces. Conditions such as chamber pressure can be altered to solve this problem. Magnetic sputtering is the most used PVD methods, however, it has drawbacks too. For example, it may cause damage to the semiconductor surface because of its high-energy ions.[107]

CVD techniques have also been employed to deposit protective layers on photoelectrodes. In a typical CVD, the semiconductor is exposed to one or more volatile precursors, which react with each other or decompose to deposit a thin layer on photoelectrodes. During the reaction process, volatile by-products are also generated, which can be removed by gas flow through the deposition chamber. CVD has its limitations, for example, the precursor volatility, stability and reactions between precursors will affect the stoichiometry and composition of deposited film. CVD is usually used to deposit conformal films on surfaces where other surface modification methods are not effective.

ALD is a subclass of CVD. It employs sequential and self-limiting reactions on the semiconductor surface, and it is suitable to deposit conformal and uniform thin layers on high aspect-ratio or porous semiconductors.[108] Compared to PVD and CVD, ALD can precisely control the thickness of deposited film. Due to these merits, it is extensively employed to deposit protective thin layers on mesoporous photoelectrodes, leading to enhancement in stability and efficiency of PEC cells.[105]

ED is a well-known method that utilizes an electric current to deposit thin layers on a material. It can deposit films on high aspect-ratio materials. The limitation of this technique is its deposition conditions such as the liquid environment, and this technique can't be employed to deposit compact and pinhole-free coatings. It is extensively studied on catalyst formation such as electrodeposition of Co and Ni oxides,[109] as this technique is frequently used to deposit porous films, which can maximize the number of sites for catalysis. However, the porosity of the deposited film limits its application on protection of photoelectrodes.

Sol-gel involves conversion of monomers into a colloidal solution (sol), and this sol is the precursor to further form integrated network (gel) of particles. This technique attracts interest due to its low cost and easy implementation. It has been applied to deposit thin protective films on semiconductors, such as ultrathin films of ZnS, Mn-doped ZnS, ZnO, and SiO_2 on silicon substrates.[110] However, thin films obtained by sol-gel are usually porous, limiting its use in protective films.[111,112]

Materials of Protective Layers

Metals. Metal films such as Pt, Pd, Ni, Au and Ru need to meet two requirements to be used as the protective layer: thermodynamic stability and transparency to incident illumination. Anodic corrosions occur on some metal films, resulting in a porous structure in the film.[91] The

protective films should be thicker than the anodization depth, which can be measured by employing X-ray photoelectron spectroscopy (XPS).[113] However, the protective film should be thin enough to be transparent to ensure the light absorption. That is, there is a thickness balance between optical transparency and protection. Besides, these metals are excellent catalysts for reactions such as the hydrogen evolution reaction and oxygen evolution reaction, and therefore, they can be the protective layer as well as co-catalyst for reactions. In the late 1970s, metal thin layers of Au, Pd, and Ag were deposited by electron-beam evaporation or sputtering on GaP and Si photoanodes to prevent photocorrosion.[114] A thin layer of nickel with a thickness of 2 nm was deposited by electron beam evaporation to protect Si photoanodes in 1 M KOH for 12 h and in a borate buffer for 80 h.[115] The nickel film deposited functioned as the surface protection layer and electrocatalyst for the oxygen evolution reaction. An Ir thin film with a thickness of 4 nm was also used to protect Si photoanodes in 1.0 M H_2SO_4 for 18 h.[116]

Metal oxide protective layers. Metal oxides are the most used thin layers to protect photoelectrodes due to their chemical stability and optical transparency. There are three subcategories of metal oxides: (1) transparent conductive oxides (TCO), (2) catalytically active metal oxides, and (3) catalytically inactive metal oxides.[104] TCOs such as indium-doped tin oxide (ITO) and fluorine-doped tin oxide (FTO) can protect semiconductors in near-neutral pH aqueous electrolytes. ITO in combination with electrocatalysts such as RuO_2 and Fe_2O_3 have been employed as the protective layer on both n-type and p-type Si photoelectrodes,[117,118] showing stability of more than 3 h in 1.0 M potassium borate buffer. n-GaAs and GaP[119] were also protected by ITO. ITO was also combined with Au and NiO_x thin films to protect the Si p−n junction, showing stability longer than 2.5 h in 1.0 M NaOH.[120]

Catalytically active metal oxides have also been widely studied as protective coatings. The metal oxide films have two functions: protection and catalysis. Researchers have employed techniques such as ALD and PVD to deposit transition-metal oxide thin layers such as cobalt oxide,[121] nickel oxide,[122] iron oxide[123] and manganese oxide[123] on Si photoanodes. A nickel oxide layer was sputtered onto Si photoanodes to be the protective layer and electrocatalyst for the oxygen evolution reaction in aqueous alkaline solutions. The nickel oxide-coated Si photoanodes showed an excellent stability of 1200 h against corrosion with almost constant efficiency.[124] Oxygen-evolution catalyst $IrO_x \cdot nH_2O$ was prepared by hydrolysis and applied on a CdSe/CdS QDs co-sensitized ZnO nanowire photoanode in a PEC hydrogen generation system. The deposition of $IrO_x \cdot nH_2O$ on photoelectrode surface significantly enhanced photoelectrode stability. The photocurrent was about 95% of the initial value after 3 h illumination.[125] Nb_2O_5 nanoparticles with diameter around 3, 6 and 9 nm were synthesized and linked to CdS films via thioglycerol as an organic linker. The nano-Nb_2O_5-modified photoanode showed a 23-fold higher power conversion efficiency compared to that of bare CdS. Nanoparticles on the CdS surface protected CdS, and the CdS photoanode was stable for more than 4 h, while the bare CdS decomposed completely in tens of minutes.[126]

Catalytically inactive metal oxides with wide band gap such as TiO_2, ZnO, and Al_2O_3 have been studied as barrier layers to protect photoanodes. The thin layer of metal oxides is used as a barrier to photogenerated holes transport due to the valence band offset between the protective metal oxides and photoelectrode semiconductors.[127] Chen et al[128] employed ALD technique to deposit a uniform layer of TiO_2 with a thickness of 2 nm on Si. Optically transmitting layer of 3 nm iridium was used as the catalyst for water oxidation. The TiO_2 and iridium coated electrode was stable in many hours in harsh pH environments, while the one

without protective layer quickly failed. Hu et al[129] deposited TiO_2 coatings with a thickness of 4 to 143 nm by ALD on Si, and a thin layer of NiO_x was used as electrocatalysts for water oxidation. The protective Si photoelectrode showed stability of more than 100 h in oxidation of 1.0 M aqueous KOH. Similarly, combination of Pt or other electrocatalysts and TiO_2 films deposited by ALD have been used to stabilize Cu_2O[130] and InP[131] photocathodes in aqueous acidic solutions. II–VI semiconductors such as CdS, CdTe, CdSe, ZnTe are the most used semiconductors due to excellent photocatalytic properties. However, they all have photocorrosion in aqueous electrolytes and need protection layers if employed as photoanodes. TiO_2 is the most used metal oxide to passivate surface to reduce charge recombination at surface states, increase the reaction kinetics and protect the semiconductor from corrosion. Yu [132] employed ALD to deposit a TiO_2 thin film with a thickness of 2 nm on the CdS QDs-sensitized photoelectrode. TiO_2 protective layer was thin enough that it didn't affect the charge transfer, and at the same time, it reduced the charge recombination, enhanced the efficiency and prevented the photocorrosion of CdS QDs in the I^-/I_3^- electrolyte. The photoelectrode was completely stable for at least 20 min under irradiation and reduced to about 70% of its original value after 1 h of irradiation. Lewis et al.[101] deposited an amorphous TiO_2 layer with a thickness of about 140 nm on CdTe by employing ALD and incorporated a thin layer of NiO as the oxygen-evolution electrocatalyst. The photoelectrode was stable for 4 days under the protection of the double layers.

1.4 Solar-driven Hydrogen Production from Urea

1.4.1 Hydrogen Production by PEC Water Splitting

Hydrogen is considered a promising alternative energy source and can be produced from different renewable energy sources. It can also be stored and efficiently converted into electrical and thermal power.[133] Solar energy is the largest renewable energy source, providing energy

greater by an order of magnitude than current energy needed by human being.[134] During the last few decades, the PEC research has focused on the development of earth abundant materials for the PEC hydrogen production.[135–138] Of which, photoelectrochemical water splitting is an attractive and clean method for the hydrogen production.[15]

The thermodynamic requirement for solar-driven hydrogen production *via* water splitting is that the semiconductor conduction and valence band positions straddle the water reduction and oxidation potentials, respectively. This translates to the necessity for the semiconductor conduction band to be more negative on the electrochemical energy scale than the water reduction potential, i.e. 0 V *vs.* NHE. A number of n-type semiconductors demonstrate the ability for hydrogen evolution from reduction of water.[139] Under irradiation, the semiconductor will absorb light and undergo an electronic transition that promotes an energetically excited electron into the conduction band, which generates electron-hole pairs to carry out the interfacial chemical redox reactions. If we introduce the semiconductor into a photoelectrode and assemble a photoelectrochemical reactor, electrons will then transfer to the cathode through the connecting wire to reduce water while holes diffuse to the semiconductor-electrolyte interface and oxidize water.[140] The photogenerated electrons and holes can also recombine, however, if the electron and hole transfer rate is higher than the recombine rate, the reduction and oxidation reactions are kinetically favored and chemical products can be obtained.

The wide band gap semiconductor TiO_2 has been researched extensively in unbiased water splitting since the pioneer work of Fujishima and Honda in 1972[141] because of its stability and environmentally benign nature. However, its wide band gap of ~3.2 eV (anatase) limits its visible-light absorption and therefore the overall rate of water splitting. Photosensitizers that can absorb visible light were then proposed to improve the efficiency of TiO_2. CdS has a band gap of

~2.4 eV and straddled conduction and valence band positions relative to the water reduction and oxidation potentials, hence it has been investigated as the water splitting hydrogen production photocatalyst for decades.[142] Photosensitization of mesoscopic TiO_2 by semiconductor nanocrystals with narrow band gap such as CdS (~2.4 eV, bulk) and CdSe (~1.8 eV, bulk) extends the photoresponse of TiO_2 through the formation of a donor-acceptor heterostructure. This configuration allows photoexcited electrons to transfer from the photosensitizer conduction band to the acceptor (i.e. TiO_2) conduction band, which is at a more positive position. The mesoscopic TiO_2 network also significantly increases the total surface area of the photosensitizer-TiO_2 interface and reduces the diffusion length a charge carrier must travel to reach the interface.

CdS-sensitized TiO_2 has been investigated extensively and shown improved incident photo-to-current efficiency.[158] The transfer rate from CdS can be accelerated by increasing the thermodynamic driving force by increasing the band position offset between CdS and TiO_2. The band positions can be tuned through quantum confinement effects of CdS and pH value of the electrolyte. CdS has the self-oxidation by photogenerated holes. This occurs on the surface of CdS in an aqueous environment because the CdS corrosion potential lies above the valence band on the electrochemical energy level,[159] which provides the thermodynamic driving force for hole transfer to the corrosion states. Also, the oxygen evolution reaction is inherently slow,[160] causing difficulty kinetically competing with the water-mediated surface corrosion.

1.4.2 Hydrogen Production from Urea

Urea [$CO(NH_2)_2$], a major component of human urine, has been proposed as a source of hydrogen as it has a gravimetric hydrogen content of 6.71%.[8] Also, it is stable, non-toxic and is environmentally benign. Direct conversion of urine and urea to hydrogen via electrochemical

oxidation by employing an inexpensive nickel catalyst was reported in 2009.[161] In an alkaline urea electrolytic cell, urea is oxidized at the anode. During the hydrogen production process, Ni-containing catalysts are needed to decompose the urea. Results reveal that urea dissociates at the nickel and hydroxide group and NiOOH can catalyze urea in electrochemical research. The catalyst $Ni(OH)_2$ was oxidized to NiOOH at the anode at 0.49 V vs. standard hydrogen electrode (SHE), and then NiOOH oxidized urea and was reduced to $Ni(OH)_2$. On the cathode, alkaline reduction of water occurred at -0.83 V vs. SHE. The overall electrolytic cell potential of 0.37 V is thermodynamically required to electrolyze urea at standard conditions. Compared to the potential needed to electrolyze water 1.23 V, hydrogen production from urea is theoretically 70% cheaper. The electrochemical method to produce hydrogen from urea requires external power and hence is energy-consuming.

Solar-driven hydrogen production from urea as a renewable and energy-saving way was proposed in 2012.[11] Hydrogen directly released from urea and human urine in a PEC cell, with the assistance of $Ni(OH)_2$ modified photoanodes TiO_2 and α-Fe_2O_3. Upon photoexcitation, TiO_2 and α-Fe_2O_3 generated electrons and holes. Photoexcited holes were captured by urea and oxidized urea, while photoexcited electrons transferred to the counter electrode via external circuit to reduce water to produce hydrogen. Continuous and stable hydrogen was observed at the counter electrode in both urea and urine electrolyte under irradiation of 100 mW/ cm^2. Hydrogen production from urea driven by solar energy is a sustainable, safe, energy-saving and environmental-friendly technique.

References

(1) Bozoglan, E.; Midilli, A.; Hepbasli, A. Sustainable Assessment of Solar Hydrogen Production Techniques. *Energy Exergy Model. Adv. Energy Syst.* **2012**, *46* (1), 85–93.

(2) Dincer, I.; Acar, C. Review and Evaluation of Hydrogen Production Methods for Better Sustainability. *Int. J. Hydrog. Energy* **2015**, *40* (34), 11094–11111.

(3) Ewan, B. C. R.; Allen, R. W. K. A Figure of Merit Assessment of the Routes to Hydrogen. *Int. J. Hydrog. Energy* **2005**, *30* (8), 809–819.

(4) Hallenbeck, P. C.; Benemann, J. R. Biological Hydrogen Production; Fundamentals and Limiting Processes. *Biohydrogen* **2002**, *27* (11), 1185–1193.

(5) Onuki, K.; Kubo, S.; Terada, A.; Sakaba, N.; Hino, R. Thermochemical Water-Splitting Cycle Using Iodine and Sulfur. *Energy Environ. Sci.* **2009**, *2* (5), 491–497.

(6) Jacobsson, T. J.; Fjällström, V.; Edoff, M.; Edvinsson, T. Sustainable Solar Hydrogen Production: From Photoelectrochemical Cells to PV-Electrolyzers and Back Again. *Energy Environ. Sci.* **2014**, *7* (7), 2056–2070.

(7) Joshi, A. S.; Dincer, I.; Reddy, B. V. Solar Hydrogen Production: A Comparative Performance Assessment. *Int. Conf. Hydrog. Prod. ICH2P-2010* **2011**, *36* (17), 11246–11257.

(8) Rollinson, A. N.; Jones, J.; Dupont, V.; Twigg, M. V. Urea as a Hydrogen Carrier: A Perspective on Its Potential for Safe, Sustainable and Long-Term Energy Supply. *Energy Environ. Sci.* **2011**, *4* (4), 1216–1224.

(9) Rahimpour, M. R.; Mottaghi, H. R.; Barmaki, M. M. Hydrogen Production from Urea Wastewater Using a Combination of Urea Thermal Hydrolyser–desorber Loop and a Hydrogen-Permselective Membrane Reactor. *Fuel Process. Technol.* **2010**, *91* (6), 600-612.

(10) Lan, R.; Tao, S.; Irvine, J. T. S. A Direct Urea Fuel Cell – Power from Fertiliser and Waste. *Energy Environ. Sci.* **2010**, *3* (4), 438–441.

(11) Wang, G.; Ling, Y.; Lu, X.; Wang, H.; Qian, F.; Tong, Y.; Li, Y. Solar Driven Hydrogen Releasing from Urea and Human Urine. *Energy Environ. Sci.* **2012**, *5* (8), 8215–8219.

(12) Nozik, A. J. Photoelectrochemistry: Applications to Solar Energy Conversion. *Annu. Rev. Phys. Chem.* **1978**, *29* (1), 189–222.

(13) MILLER, B.; HELLER, A. Semiconductor Liquid Junction Solar Cells Based on Anodic Sulphide Films. *Nature* **1976**, *262*, 680.

(14) Bard, A. J. Photoelectrochemistry. *Science* **1980**, *207* (4427), 139.

(15) Dumortier, M.; Tembhurne, S.; Haussener, S. Holistic Design Guidelines for Solar Hydrogen Production by Photo-Electrochemical Routes. *Energy Environ. Sci.* **2015**, *8* (12), 3614–3628.

(16) Ellis, A. B.; Kaiser, S. W.; Bolts, J. M.; Wrighton, M. S. Study of N-Type Semiconducting Cadmium Chalcogenide-Based Photoelectrochemical Cells Employing Polychalcogenide Electrolytes. *J. Am. Chem. Soc.* **1977**, *99* (9), 2839–2848.

(17) Bard, A. J.; Bocarsly, A. B.; Fan, F. R. F.; Walton, E. G.; Wrighton, M. S. The Concept of Fermi Level Pinning at Semiconductor/liquid Junctions. Consequences for Energy Conversion Efficiency and Selection of Useful Solution Redox Couples in Solar Devices. *J. Am. Chem. Soc.* **1980**, *102* (11), 3671–3677.

(18) O'Regan, B.; Grätzel, M. A Low-Cost, High-Efficiency Solar Cell Based on Dye-Sensitized Colloidal TiO_2 Films. *Nature* **1991**, *353*, 737.

(19) Ayalew, W. A.; Ayele, D. W. Dye-Sensitized Solar Cells Using Natural Dye as Light-Harvesting Materials Extracted from Acanthus Sennii Chiovenda Flower and Euphorbia Cotinifolia Leaf. *J. Sci. Adv. Mater. Devices* **2016**, *1* (4), 488–494.

(20) Lee, C.-P.; Li, C.-T.; Ho, K.-C. Use of Organic Materials in Dye-Sensitized Solar Cells. *Mater. Today* **2017**, *20* (5), 267–283.

(21) Krauss, T. D.; O'Brien, S.; Brus, L. E. Charge and Photoionization Properties of Single Semiconductor Nanocrystals. *J. Phys. Chem. B* **2001**, *105* (9), 1725–1733.

(22) Chuang, C.-H.; Lo, S. S.; Scholes, G. D.; Burda, C. Charge Separation and Recombination in CdTe/CdSe Core/Shell Nanocrystals as a Function of Shell Coverage: Probing the Onset of the Quasi Type-II Regime. *J. Phys. Chem. Lett.* **2010**, *1* (17), 2530–2535.

(23) Kelley, A. M. Electron−Phonon Coupling in CdSe Nanocrystals. *J. Phys. Chem. Lett.* **2010**, *1* (9), 1296–1300.

(24) Abel, K. A.; Qiao, H.; Young, J. F.; van Veggel, F. C. J. M. Four-Fold Enhancement of the Activation Energy for Nonradiative Decay of Excitons in PbSe/CdSe Core/Shell versus PbSe Colloidal Quantum Dots. *J. Phys. Chem. Lett.* **2010**, *1* (15), 2334–2338.

(25) Scholes, G. D. Insights into Excitons Confined to Nanoscale Systems: Electron–Hole Interaction, Binding Energy, and Photodissociation. *ACS Nano* **2008**, *2* (3), 523–537.

(26) Nirmal, M.; Brus, L. Luminescence Photophysics in Semiconductor Nanocrystals. *Acc. Chem. Res.* **1999**, *32* (5), 407–414.

(27) Klimov, V. I. Mechanisms for Photogeneration and Recombination of Multiexcitons in Semiconductor Nanocrystals: Implications for Lasing and Solar Energy Conversion. *J. Phys. Chem. B* **2006**, *110* (34), 16827–16845.

(28) McGuire, J. A.; Joo, J.; Pietryga, J. M.; Schaller, R. D.; Klimov, V. I. New Aspects of Carrier Multiplication in Semiconductor Nanocrystals. *Acc. Chem. Res.* **2008**, *41* (12), 1810–1819.

(29) Sykora, M.; Petruska, M. A.; Alstrum-Acevedo, J.; Bezel, I.; Meyer, T. J.; Klimov, V. I. Photoinduced Charge Transfer between CdSe Nanocrystal Quantum Dots and Ru−Polypyridine Complexes. *J. Am. Chem. Soc.* **2006**, *128* (31), 9984–9985.

(30) Araci, Z. O.; Shallcross, C. R.; Armstrong, N. R.; Saavedra, S. S. Potential-Modulated Attenuated Total Reflectance Characterization of Charge Injection Processes in Monolayer-Tethered CdSe Nanocrystals. *J. Phys. Chem. Lett.* **2010**, *1* (12), 1900–1905.

(31) Schaller, R. D.; Petruska, M. A.; Klimov, V. I. Tunable Near-Infrared Optical Gain and Amplified Spontaneous Emission Using PbSe Nanocrystals. *J. Phys. Chem. B* **2003**, *107* (50), 13765–13768.

(32) Wang, D.; Zhao, H.; Wu, N.; El Khakani, M. A.; Ma, D. Tuning the Charge-Transfer Property of PbS-Quantum Dot/TiO_2-Nanobelt Nanohybrids via Quantum Confinement. *J. Phys. Chem. Lett.* **2010**, *1* (7), 1030–1035.

(33) Shalom, M.; Rühle, S.; Hod, I.; Yahav, S.; Zaban, A. Energy Level Alignment in CdS Quantum Dot Sensitized Solar Cells Using Molecular Dipoles. *J. Am. Chem. Soc.* **2009**, *131* (29), 9876–9877.

(34) Barea, E. M.; Shalom, M.; Giménez, S.; Hod, I.; Mora-Seró, I.; Zaban, A.; Bisquert, J. Design of Injection and Recombination in Quantum Dot Sensitized Solar Cells. *J. Am. Chem. Soc.* **2010**, *132* (19), 6834–6839.

(35) Gómez-Navarro, C.; Weitz, R. T.; Bittner, A. M.; Scolari, M.; Mews, A.; Burghard, M.; Kern, K. Electronic Transport Properties of Individual Chemically Reduced Graphene Oxide Sheets. *Nano Lett.* **2007**, *7* (11), 3499–3503.

(36) Semonin, O. E.; Johnson, J. C.; Luther, J. M.; Midgett, A. G.; Nozik, A. J.; Beard, M. C. Absolute Photoluminescence Quantum Yields of IR-26 Dye, PbS, and PbSe Quantum Dots. *J. Phys. Chem. Lett.* **2010**, *1* (16), 2445–2450.

(37) Nazeeruddin, M. K.; Humphry-Baker, R.; Liska, P.; Grätzel, M. Investigation of Sensitizer Adsorption and the Influence of Protons on Current and Voltage of a Dye-Sensitized Nanocrystalline TiO_2 Solar Cell. *J. Phys. Chem. B* **2003**, *107* (34), 8981–8987.

(38) Wang, J.; Qu, S.; Zhong, Z.; Wang, S.; Liu, K.; Hu, A. Fabrication of TiO_2 Nanoparticles/nanorod Composite Arrays via a Two-Step Method for Efficient Dye-Sensitized Solar Cells. *Prog. Nat. Sci. Mater. Int.* **2014**, *24* (6), 588–592.

(39) Yao, W.-T.; Yu, S.-H.; Liu, S.-J.; Chen, J.-P.; Liu, X.-M.; Li, F.-Q. Architectural Control Syntheses of CdS and CdSe Nanoflowers, Branched Nanowires, and Nanotrees via a Solvothermal Approach in a Mixed Solution and Their Photocatalytic Property. *J. Phys. Chem. B* **2006**, *110* (24), 11704–11710.

(40) Talgorn, E.; Moysidou, E.; Abellon, R. D.; Savenije, T. J.; Goossens, A.; Houtepen, A. J.; Siebbeles, L. D. A. Highly Photoconductive CdSe Quantum-Dot Films: Influence of Capping Molecules and Film Preparation Procedure. *J. Phys. Chem. C* **2010**, *114* (8), 3441–3447.

(41) Shalom, M.; Albero, J.; Tachan, Z.; Martínez-Ferrero, E.; Zaban, A.; Palomares, E. Quantum Dot−Dye Bilayer-Sensitized Solar Cells: Breaking the Limits Imposed by the Low Absorbance of Dye Monolayers. *J. Phys. Chem. Lett.* **2010**, *1* (7), 1134–1138.

(42) Bard, A. J.; Bocarsly, A. B.; Fan, F. R. F.; Walton, E. G.; Wrighton, M. S. The Concept of Fermi Level Pinning at Semiconductor/liquid Junctions. Consequences for Energy Conversion Efficiency and Selection of Useful Solution Redox Couples in Solar Devices. *J. Am. Chem. Soc.* **1980**, *102* (11), 3671–3677.

(43) Kamat, P. V. Capturing Hot Electrons. *Nat. Chem.* **2010**, *2*, 809–810.

(44) Pandey, A.; Guyot-Sionnest, P. Hot Electron Extraction from Colloidal Quantum Dots. *J. Phys. Chem. Lett.* **2010**, *1* (1), 45–47.

(45) Tisdale, W. A.; Williams, K. J.; Timp, B. A.; Norris, D. J.; Aydil, E. S.; Zhu, X.-Y. Hot-Electron Transfer from Semiconductor Nanocrystals. *Science* **2010**, *328* (5985), 1543-1547.

(46) Ellingson, R. J.; Beard, M. C.; Johnson, J. C.; Yu, P.; Micic, O. I.; Nozik, A. J.; Shabaev, A.; Efros, A. L. Highly Efficient Multiple Exciton Generation in Colloidal PbSe and PbS Quantum Dots. *Nano Lett.* **2005**, *5* (5), 865–871.

(47) Beard, M. C.; Knutsen, K. P.; Yu, P.; Luther, J. M.; Song, Q.; Metzger, W. K.; Ellingson, R. J.; Nozik, A. J. Multiple Exciton Generation in Colloidal Silicon Nanocrystals. *Nano Lett.* **2007**, *7* (8), 2506–2512.

(48) Trinh, M. T.; Houtepen, A. J.; Schins, J. M.; Hanrath, T.; Piris, J.; Knulst, W.; Goossens, A. P. L. M.; Siebbeles, L. D. A. In Spite of Recent Doubts Carrier Multiplication Does Occur in PbSe Nanocrystals. *Nano Lett.* **2008**, *8* (6), 1713–1718.

(49) Hagfeldt, A.; Graetzel, M. Light-Induced Redox Reactions in Nanocrystalline Systems. *Chem. Rev.* **1995**, *95* (1), 49–68.

(50) Rajeshwar, K.; de Tacconi, N. R.; Chenthamarakshan, C. R. Semiconductor-Based Composite Materials: Preparation, Properties, and Performance. *Chem. Mater.* **2001**, *13* (9), 2765–2782.

(51) Choi, K.-S. Shape Effect and Shape Control of Polycrystalline Semiconductor Electrodes for Use in Photoelectrochemical Cells. *J. Phys. Chem. Lett.* **2010**, *1* (15), 2244–2250.

(52) Zaban, A.; Mićić, O. I.; Gregg, B. A.; Nozik, A. J. Photosensitization of Nanoporous TiO_2 Electrodes with InP Quantum Dots. *Langmuir* **1998**, *14* (12), 3153–3156.

(53) Vogel, R.; Pohl, K.; Weller, H. Sensitization of Highly Porous, Polycrystalline TiO_2 Electrodes by Quantum Sized CdS. *Chem. Phys. Lett.* **1990**, *174* (3), 241–246.

(54) Ward, M. D.; White, J. R.; Bard, A. J. Electrochemical Investigation of the Energetics of Particulate Titanium Dioxide Photocatalysts. The Methyl Viologen-Acetate System. *J. Am. Chem. Soc.* **1983**, *105* (1), 27–31.

(55) Kochev, K. D. Preparation and Protoelectrochemical Properties of TiO_2 Thin Binder Layers. *Sol. Energy Mater.* **1985**, *12* (4), 249–256.

(56) O'Regan, B.; Grätzel, M. A Low-Cost, High-Efficiency Solar Cell Based on Dye-Sensitized Colloidal TiO2 Films. *Nature* **1991**, *353*, 737.

(57) Jun, H. K.; Careem, M. A.; Arof, A. K. Quantum Dot-Sensitized Solar Cells—perspective and Recent Developments: A Review of Cd Chalcogenide Quantum Dots as Sensitizers. *Renew. Sustain. Energy Rev.* **2013**, *22*, 148–167.

(58) Harrison, S.; Hayne, M. Photoelectrolysis Using Type-II Semiconductor Heterojunctions. *Sci. Rep.* **2017**, *7* (1), 11638.

(59) Liu, D.; Kamat, P. V. Photoelectrochemical Behavior of Thin Cadmium Selenide and Coupled Titania/cadmium Selenide Semiconductor Films. *J. Phys. Chem.* **1993**, *97* (41), 10769–10773.

(60) Mora-Seró, I.; Bisquert, J. Breakthroughs in the Development of Semiconductor-Sensitized Solar Cells. *J. Phys. Chem. Lett.* **2010**, *1* (20), 3046–3052.

(61) Kumar, S.; Scholes, G. D. Colloidal Nanocrystal Solar Cells. *Microchim. Acta* **2008**, *160* (3), 315–325.

(62) Kamat, P. V. Quantum Dot Solar Cells. Semiconductor Nanocrystals as Light Harvesters. *J. Phys. Chem. C* **2008**, *112* (48), 18737–18753.

(63) Serpone, N.; Borgarello, E.; Grätzel, M. Visible Light Induced Generation of Hydrogen from H_2S in Mixed Semiconductor Dispersions; Improved Efficiency through Inter-Particle Electron Transfer. *J. Chem. Soc. Chem. Commun.* **1984**, *6*, 342–344.

(64) Gopidas, K. R.; Bohorquez, M.; Kamat, P. V. Photophysical and Photochemical Aspects of Coupled Semiconductors: Charge-Transfer Processes in Colloidal Cadmium Sulfide-Titania and Cadmium Sulfide-silver(I) Iodide Systems. *J. Phys. Chem.* **1990**, *94* (16), 6435–6440.

(65) Lu, C.; Zhang, L.; Zhang, Y.; Liu, S. Electrodeposition of TiO_2/CdSe Heterostructure Films and Photocatalytic Degradation of Methylene Blue. *Mater. Lett.* **2016**, *185*, 342–345.

(66) Narayanan, R.; Deepa, M.; Srivastava, A. K. Nanoscale Connectivity in a TiO_2/CdSe Quantum Dots/functionalized Graphene Oxide nanosheets/Au Nanoparticles Composite for Enhanced Photoelectrochemical Solar Cell Performance. *Phys. Chem. Chem. Phys.* **2012**, *14* (2), 767–778.

(67) Kim, J.; Choi, S.; Noh, J.; Yoon, S.; Lee, S.; Noh, T.; Frank, A. J.; Hong, K. Synthesis of CdSe−TiO_2 Nanocomposites and Their Applications to TiO_2 Sensitized Solar Cells. *Langmuir* **2009**, *25* (9), 5348–5351.

(68) Pawar, S. A.; Patil, D. S.; Jung, H. R.; Park, J. Y.; Mali, S. S.; Hong, C. K.; Shin, J.-C.; Patil, P. S.; Kim, J.-H. Quantum Dot Sensitized Solar Cell Based on TiO_2/CdS/CdSe/ZnS Heterostructure. *Electrochimica Acta* **2016**, *203*, 74–83.

(69) Velanganni, S.; Pravinraj, S.; Immanuel, P.; Thiruneelakandan, R. Nanostructure CdS/ZnO Heterojunction Configuration for Photocatalytic Degradation of Methylene Blue. *Phys. B Condens. Matter* **2018**, *534*, 56–62.

(70) Vaishnav, J. K.; Arbuj, S. S.; Rane, S. B.; Amalnerkar, D. P. One Dimensional CdS/ZnO Nanocomposites: An Efficient Photocatalyst for Hydrogen Generation. *RSC Adv.* **2014**, *4* (88), 47637–47642.

(71) Kim, Y. G.; Jo, W.-K. Photodeposited-metal/CdS/ZnO Heterostructures for Solar Photocatalytic Hydrogen Production under Different Conditions. *Int. J. Hydrog. Energy* **2017**, *42* (16), 11356–11363.

(72) An, L.; Wang, G.; Cheng, Y.; Zhao, L.; Gao, F.; Cheng, Y. Synthesis of CdS/ZnO Nanocomposite and Its Enhanced Photocatalytic Activity in Degradation of Methyl Orange. *Russ. J. Phys. Chem. A* **2015**, *89* (10), 1878–1883.

(73) Kamat, P. V.; Patrick, B. Photophysics and Photochemistry of Quantized Zinc Oxide Colloids. *J. Phys. Chem.* **1992**, *96* (16), 6829–6834.

(74) Rabani, J. Sandwich Colloids of Zinc Oxide and Zinc Sulfide in Aqueous Solutions. *J. Phys. Chem.* **1989**, *93* (22), 7707–7713.

(75) Trindade, T. N. S.; Silva, L. A. Cd-Doped SnO_2/CdS Heterostructures for Efficient Application in Photocatalytic Reforming of Glycerol to Produce Hydrogen under Visible Light Irradiation. *J. Alloys Compd.* **2018**, *735*, 400–408.

(76) Kumar, V.; Rajaram, P.; Goswami, Y. C. Sol–gel Synthesis of SnO_2/CdS Heterostructures Using Various Cd:S Molar Ratio Solutions and Its Application in Photocatalytic Degradation of Organic Dyes. *J. Mater. Sci. Mater. Electron.* **2017**, *28* (12), 9024–9031.

(77) Kar, A.; Kundu, S.; Patra, A. Photocatalytic Properties of Semiconductor SnO_2/CdS Heterostructure Nanocrystals. *RSC Adv.* **2012**, *2* (27), 10222–10230.

(78) Naushad, M.; Khan, M. R.; Bhande, S. S.; Shaikh, S. F.; Alfadul, S. M.; Shinde, P. V.; Mane, R. S. High Current Density Cation-Exchanged SnO_2–CdSe/ZnSe and SnO_2–CdSe/SnSe Quantum-Dot Photoelectrochemical Cells. *New J. Chem.* **2018**, *42* (11), 9028–9036.

(79) Kumar, V.; Rajaram, P.; Goswami, Y. C. Sol Gel Synthesis of SnO_2/CdSe Nanocomposites and Their Optical Structural and Morphological Characterizations. *Opt. - Int. J. Light Electron Opt.* **2016**, *127* (5), 2490–2494.

(80) Unni, G. E.; Deepak, T. G.; Sreekumaran Nair, A. Fabrication of CdSe Sensitized SnO_2 Nanofiber Quantum Dot Solar Cells. *Mater. Sci. Semicond. Process.* **2016**, *41*, 370–377.

(81) Lin, Y.; Yu Lin; Meng, Y.; Tu, Y.; Zhang, X. CdS/CdSe Co-Sensitized SnO_2 Photoelectrodes for Quantum Dots Sensitized Solar Cells. *Opt. Commun.* **2015**, *346*, 64–68.

(82) Bedja, I.; Kamat, P. V. Capped Semiconductor Colloids. Synthesis and Photoelectrochemical Behavior of TiO_2 Capped SnO_2 Nanocrystallites. *J. Phys. Chem.* **1995**, *99* (22), 9182–9188.

(83) Vinodgopal, K.; Bedja, I.; Kamat, P. V. Nanostructured Semiconductor Films for Photocatalysis. Photoelectrochemical Behavior of SnO_2/TiO_2 Composite Systems and Its Role in Photocatalytic Degradation of a Textile Azo Dye. *Chem. Mater.* **1996**, *8* (8), 2180–2187.

(84) Vogel, R.; Hoyer, P.; Weller, H. Quantum-Sized PbS, CdS, Ag_2S, Sb_2S_3, and Bi_2S_3 Particles as Sensitizers for Various Nanoporous Wide-Bandgap Semiconductors. *J. Phys. Chem.* **1994**, *98* (12), 3183–3188.

(85) Nakade, S.; Kubo, W.; Saito, Y.; Kanzaki, T.; Kitamura, T.; Wada, Y.; Yanagida, S. Influence of Measurement Conditions on Electron Diffusion in Nanoporous TiO_2 Films: Effects of Bias Light and Dye Adsorption. *J. Phys. Chem. B* **2003**, *107* (51), 14244–14248.

(86) Mori, S.; Sunahara, K.; Fukai, Y.; Kanzaki, T.; Wada, Y.; Yanagida, S. Electron Transport and Recombination in Dye-Sensitized TiO_2 Solar Cells Fabricated without Sintering Process. *J. Phys. Chem. C* **2008**, *112* (51), 20505–20509.

(87) Qian, S.; Wang, C.; Liu, W.; Zhu, Y.; Yao, W.; Lu, X. An Enhanced CdS/TiO_2 Photocatalyst with High Stability and Activity: Effect of Mesoporous Substrate and Bifunctional Linking Molecule. *J. Mater. Chem.* **2011**, *21* (13), 4945–4952.

(88) Liu, D.; Kamat, P. V. Photoelectrochemical Behavior of Thin Cadmium Selenide and Coupled Titania/cadmium Selenide Semiconductor Films. *J. Phys. Chem.* **1993**, *97* (41), 10769–10773.

(89) Moon, S.-J.; Itzhaik, Y.; Yum, J.-H.; Zakeeruddin, S. M.; Hodes, G.; Grätzel, M. Sb_2S_3-Based Mesoscopic Solar Cell Using an Organic Hole Conductor. *J. Phys. Chem. Lett.* **2010**, *1* (10), 1524–1527.

(90) Fredy Nandjou and Sophia Haussener. Degradation in Photoelectrochemical Devices: Review with an Illustrative Case Study. *J. Phys. Appl. Phys.* **2017**, *50* (12), 124002.

(91) Hu, S.; Lewis, N. S.; Ager, J. W.; Yang, J.; McKone, J. R.; Strandwitz, N. C. Thin-Film Materials for the Protection of Semiconducting Photoelectrodes in Solar-Fuel Generators. *J. Phys. Chem. C* **2015**, *119* (43), 24201–24228.

(92) Chen, S.; Wang, L.-W. Thermodynamic Oxidation and Reduction Potentials of Photocatalytic Semiconductors in Aqueous Solution. *Chem. Mater.* **2012**, *24* (18), 3659–3666.

(93) Caccamo, L.; Cocco, G.; Martín, G.; Zhou, H.; Fundling, S.; Gad, A.; Mohajerani, M. S.; Abdelfatah, M.; Estradé, S.; Peiró, F.; et al. Insights into Interfacial Changes and Photoelectrochemical Stability of $In_xGa_{1-x}N$ (0001) Photoanode Surfaces in Liquid Environments. *ACS Appl. Mater. Interfaces* **2016**, *8* (12), 8232–8238.

(94) Young, J. L.; Steirer, K. X.; Dzara, M. J.; Turner, J. A.; Deutsch, T. G. Remarkable Stability of Unmodified GaAs Photocathodes during Hydrogen Evolution in Acidic Electrolyte. *J. Mater. Chem. A* **2016**, *4* (8), 2831–2836.

(95) Zhou, L.; Yan, Q.; Yu, J.; Jones, R. J. R.; Becerra-Stasiewicz, N.; Suram, S. K.; Shinde, A.; Guevarra, D.; Neaton, J. B.; Persson, K. A.; et al. Stability and Self-Passivation of Copper Vanadate Photoanodes under Chemical, Electrochemical, and Photoelectrochemical Operation. *Phys. Chem. Chem. Phys.* **2016**, *18* (14), 9349–9352.

(96) Aguiar, J. A.; Anderson, N. C.; Neale, N. R. Revealing the Semiconductor–catalyst Interface in Buried Platinum Black Silicon Photocathodes. *J. Mater. Chem. A* **2016**, *4* (21), 8123–8129.

(97) Lai, J.; Yuan, D.; Huang, P.; Zhang, J.; Su, J.-J.; Tian, Z.-W.; Zhan, D. Kinetic Investigation on the Photoetching Reaction of N-Type GaAs by Scanning Electrochemical Microscopy. *J. Phys. Chem. C* **2016**, *120* (30), 16446–16452.

(98) Vinodgopal, K.; Hotchandani, S.; Kamat, P. V. Electrochemically Assisted Photocatalysis: Titania Particulate Film Electrodes for Photocatalytic Degradation of 4-Chlorophenol. *J. Phys. Chem.* **1993**, *97* (35), 9040–9044.

(99) Bedja, I.; Hotchandani, S.; Kamat, P. V. Preparation and Photoelectrochemical Characterization of Thin SnO_2 Nanocrystalline Semiconductor Films and Their

Sensitization with Bis(2,2'-bipyridine) (2,2'-bipyridine-4,4'-dicarboxylic acid) ruthenium (II) Complex. *J. Phys. Chem.* **1994**, *98* (15), 4133–4140.

(100) Inoue, T.; Watanabe, T.; Fujishima, A.; Honda, K.; Kohayakawa, K. Suppression of Surface Dissolution of CdS Photoanode by Reducing Agents. *J. Electrochem. Soc.* **1977**, *124* (5), 719–722.

(101) Lichterman, M. F.; Carim, A. I.; McDowell, M. T.; Hu, S.; Gray, H. B.; Brunschwig, B. S.; Lewis, N. S. Stabilization of N-Cadmium Telluride Photoanodes for Water Oxidation to O2(g) in Aqueous Alkaline Electrolytes Using Amorphous TiO_2 Films Formed by Atomic-Layer Deposition. *Energy Environ. Sci.* **2014**, *7* (10), 3334–3337.

(102) He, Y.; Thorne, J. E.; Wu, C. H.; Ma, P.; Du, C.; Dong, Q.; Guo, J.; Wang, D. What Limits the Performance of Ta_3N_5 for Solar Water Splitting? *Chem* **2016**, *1* (4), 640–655.

(103) Colmenares, J. C.; Luque, R.; Campelo, J. M.; Colmenares, F.; Karpiński, Z.; Romero, A. A. Nanostructured Photocatalysts and Their Applications in the Photocatalytic Transformation of Lignocellulosic Biomass: An Overview. *Materials* **2009**, *2* (4), 2228–2258.

(104) Hu, S.; Lewis, N. S.; Ager, J. W.; Yang, J.; McKone, J. R.; Strandwitz, N. C. Thin-Film Materials for the Protection of Semiconducting Photoelectrodes in Solar-Fuel Generators. *J. Phys. Chem. C* **2015**, *119* (43), 24201–24228.

(105) Scheuermann, A. G.; McIntyre, P. C. Atomic Layer Deposited Corrosion Protection: A Path to Stable and Efficient Photoelectrochemical Cells. *J. Phys. Chem. Lett.* **2016**, *7* (14), 2867–2878.

(106) Rovelli, L.; Tilley, S. D.; Sivula, K. Optimization and Stabilization of Electrodeposited Cu2ZnSnS4 Photocathodes for Solar Water Reduction. *ACS Appl. Mater. Interfaces* **2013**, *5* (16), 8018–8024.

(107) Tsai, M.; Fahrenbruch, A.; H. Bube, R. Sputtered Oxide/indium Phosphide Junctions and Indium Phosphide Surfaces. *J. Appl. Phys.* **1980**, *51* (5), 2696–2705.

(108) George, S. M. Atomic Layer Deposition: An Overview. *Chem. Rev.* **2010**, *110* (1), 111–131.

(109) Kanan, M. W.; Surendranath, Y.; Nocera, D. G. Cobalt–phosphate Oxygen-Evolving Compound. *Chem. Soc. Rev.* **2009**, *38* (1), 109–114.

(110) Kovtyukhova, N. I.; Buzaneva, E. V.; Waraksa, C. C.; Martin, B. R.; Mallouk, T. E. Surface Sol−Gel Synthesis of Ultrathin Semiconductor Films. *Chem. Mater.* **2000**, *12* (2), 383–389.

(111) Lev, O.; Wu, Z.; Bharathi, S.; Glezer, V.; Modestov, A.; Gun, J.; Rabinovich, L.; Sampath, S. Sol−Gel Materials in Electrochemistry. *Chem. Mater.* **1997**, *9* (11), 2354–2375.

(112) Yuan, J.; Tsujikawa, S. Characterization of Sol-Gel-Derived TiO_2 Coatings and Their Photoeffects on Copper Substrates. *J. Electrochem. Soc.* **1995**, *42* (10), 3444–3450.

(113) Mei, B.; Permyakova, A. A.; Frydendal, R.; Bae, D.; Pedersen, T.; Malacrida, P.; Hansen, O.; Stephens, I. E. L.; Vesborg, P. C. K.; Seger, B.; et al. Iron-Treated NiO as a Highly Transparent P-Type Protection Layer for Efficient Si-Based Photoanodes. *J. Phys. Chem. Lett.* **2014**, *5* (20), 3456–3461.

(114) Nakato, Y.; Ohnishi, T.; Tsubomura, H. Photo-electrochemical Behaviors of Semiconductor Electrodes Coated with Thin Metal Films. *Chem. Lett.* **1975**, *4* (8), 883–886.

(115) Kenney, M. J.; Gong, M.; Li, Y.; Wu, J. Z.; Feng, J.; Lanza, M.; Dai, H. High-Performance Silicon Photoanodes Passivated with Ultrathin Nickel Films for Water Oxidation. *Science* **2013**, *342* (6160), 836.

(116) Mei, B.; Seger, B.; Pedersen, T.; Malizia, M.; Hansen, O.; Chorkendorff, I.; Vesborg, P. C. K. Protection of P+-N-Si Photoanodes by Sputter-Deposited Ir/IrO_x Thin Films. *J. Phys. Chem. Lett.* **2014**, *5* (11), 1948–1952.

(117) Hodes, G.; Thompson, L.; DuBow, J.; Rajeshwar, K. Heterojunction Silicon/indium Tin Oxide Photoelectrodes: Development of Stable Systems in Aqueous Electrolytes and Their Applicability to Solar Energy Conversion and Storage. *J. Am. Chem. Soc.* **1983**, *105* (3), 324–330.

(118) Badawy, W. A. Improved N-Si/oxide Junctions for Environmentally Safe Solar Energy Conversion. *Sol. Energy Mater. Sol. Cells* **2002**, *71* (3), 281–294.

(119) Yamane, S.; Kato, N.; Kojima, S.; Imanishi, A.; Ogawa, S.; Yoshida, N.; Nonomura, S.; Nakato, Y. Efficient Solar Water Splitting with a Composite "n-Si/p-CuI/n-I-P a-Si/n-P GaP/RuO_2" Semiconductor Electrode. *J. Phys. Chem. C* **2009**, *113* (32), 14575–14581.

(120) Sun, K.; Shen, S.; Cheung, J. S.; Pang, X.; Park, N.; Zhou, J.; Hu, Y.; Sun, Z.; Noh, S. Y.; Riley, C. T.; et al. Si Photoanode Protected by a Metal Modified ITO Layer with Ultrathin NiO_x for Solar Water Oxidation. *Phys. Chem. Chem. Phys.* **2014**, *16* (10), 4612–4625.

(121) Yang, J.; Walczak, K.; Anzenberg, E.; Toma, F. M.; Yuan, G.; Beeman, J.; Schwartzberg, A.; Lin, Y.; Hettick, M.; Javey, A.; et al. Efficient and Sustained Photoelectrochemical Water Oxidation by Cobalt Oxide/Silicon Photoanodes with Nanotextured Interfaces. *J. Am. Chem. Soc.* **2014**, *136* (17), 6191–6194.

(122) Sun, K.; Park, N.; Sun, Z.; Zhou, J.; Wang, J.; Pang, X.; Shen, S.; Noh, S. Y.; Jing, Y.; Jin, S.; et al. Nickel Oxide Functionalized Silicon for Efficient Photo-Oxidation of Water. *Energy Environ. Sci.* **2012**, *5* (7), 7872–7877.

(123) Hiroshi Morisaki and Hiroshi Ono and Hitoshi Dohkoshi and Kazuhiko Yazawa. Iron-Oxide Coated N-Si as a Heterostructure Photoanode for the Photoelectrolysis of Water. *Jpn. J. Appl. Phys.* **1980**, *19* (3), L148.

(124) Sun, K.; McDowell, M. T.; Nielander, A. C.; Hu, S.; Shaner, M. R.; Yang, F.; Brunschwig, B. S.; Lewis, N. S. Stable Solar-Driven Water Oxidation to O_2(g) by Ni-Oxide-Coated Silicon Photoanodes. *J. Phys. Chem. Lett.* **2015**, *6* (4), 592–598.

(125) Seol, M.; Jang, J.-W.; Cho, S.; Lee, J. S.; Yong, K. Highly Efficient and Stable Cadmium Chalcogenide Quantum Dot/ZnO Nanowires for Photoelectrochemical Hydrogen Generation. *Chem. Mater.* **2013**, *25* (2), 184–189.

(126) Pareek, A.; Paik, P.; Borse, P. H. Nanoniobia Modification of CdS Photoanode for an Efficient and Stable Photoelectrochemical Cell. *Langmuir* **2014**, *30* (51), 15540–15549.

(127) Robertson, J. Band Offsets of High Dielectric Constant Gate Oxides on Silicon. *J. Non-Cryst. Solids* **2002**, *303* (1), 94–100.

(128) Chen, Y. W.; Prange, J. D.; Dühnen, S.; Park, Y.; Gunji, M.; Chidsey, C. E. D.; McIntyre, P. C. Atomic Layer-Deposited Tunnel Oxide Stabilizes Silicon Photoanodes for Water Oxidation. *Nat. Mater.* **2011**, *10*, 539.

(129) Hu, S.; Shaner, M. R.; Beardslee, J. A.; Lichterman, M.; Brunschwig, B. S.; Lewis, N. S. Amorphous TiO_2 Coatings Stabilize Si, GaAs, and GaP Photoanodes for Efficient Water Oxidation. *Science* **2014**, *344* (6187), 1005.

(130) Paracchino, A.; Laporte, V.; Sivula, K.; Grätzel, M.; Thimsen, E. Highly Active Oxide Photocathode for Photoelectrochemical Water Reduction. *Nat. Mater.* **2011**, *10*, 456.

(131) Lee, M. H.; Takei, K.; Zhang, J.; Kapadia, R.; Zheng, M.; Chen, Y.-Z.; Nah, J.; Matthews, T. S.; Chueh, Y.-L.; Ager, J. W.; et al. P-Type InP Nanopillar Photocathodes for Efficient Solar-Driven Hydrogen Production. *Angew. Chem. Int. Ed.* **2012**, *51* (43), 10760–10764.

(132) Yu, K.; Lin, X.; Lu, G.; Wen, Z.; Yuan, C.; Chen, J. Optimized CdS Quantum Dot-Sensitized Solar Cell Performance through Atomic Layer Deposition of Ultrathin TiO_2 Coating. *RSC Adv.* **2012**, *2* (20), 7843–7848.

(133) Barreto, L.; Makihira, A.; Riahi, K. The Hydrogen Economy in the 21st Century: A Sustainable Development Scenario. *Int. J. Hydrog. Energy* **2003**, *28* (3), 267–284.

(134) Lewis, N. S. Powering the Planet. *MRS Bull.* **2007**, *32* (10), 808–820.

(135) Khaselev, O.; Turner, J. A. A Monolithic Photovoltaic-Photoelectrochemical Device for Hydrogen Production via Water Splitting. *Science* **1998**, *280* (5362), 425.

(136) Abdi, F. F.; Han, L.; Smets, A. H. M.; Zeman, M.; Dam, B.; van de Krol, R. Efficient Solar Water Splitting by Enhanced Charge Separation in a Bismuth Vanadate-Silicon Tandem Photoelectrode. *Nat. Commun.* **2013**, *4*, 2195.

(137) Licht, S.; Wang, B.; Mukerji, S.; Soga, T.; Umeno, M.; Tributsch, H. Efficient Solar Water Splitting, Exemplified by RuO_2-Catalyzed AlGaAs/Si Photoelectrolysis. *J. Phys. Chem. B* **2000**, *104* (38), 8920–8924.

(138) Luo, J.; Im, J.-H.; Mayer, M. T.; Schreier, M.; Nazeeruddin, M. K.; Park, N.-G.; Tilley, S. D.; Fan, H. J.; Grätzel, M. Water Photolysis at 12.3% Efficiency via Perovskite Photovoltaics and Earth-Abundant Catalysts. *Science* **2014**, *345* (6204), 1593.

(139) Walter, M. G.; Warren, E. L.; McKone, J. R.; Boettcher, S. W.; Mi, Q.; Santori, E. A.; Lewis, N. S. Solar Water Splitting Cells. *Chem. Rev.* **2010**, *110* (11), 6446–6473.

(140) Bard, A. J. Photoelectrochemistry. *Science* **1980**, *207* (4427), 139.

(141) Fujishima, A.; Honda, K. Electrochemical Photolysis of Water at a Semiconductor Electrode. *Nature* **1972**, *238*, 37.

(142) Li, Q.; Guo, B.; Yu, J.; Ran, J.; Zhang, B.; Yan, H.; Gong, J. R. Highly Efficient Visible-Light-Driven Photocatalytic Hydrogen Production of CdS-Cluster-Decorated Graphene Nanosheets. *J. Am. Chem. Soc.* **2011**, *133* (28), 10878–10884.

(143) Gao, X.-F.; Sun, W.-T.; Hu, Z.-D.; Ai, G.; Zhang, Y.-L.; Feng, S.; Li, F.; Peng, L.-M. An Efficient Method To Form Heterojunction CdS/TiO_2 Photoelectrodes Using Highly Ordered TiO_2 Nanotube Array Films. *J. Phys. Chem. C* **2009**, *113* (47), 20481–20485.

(144) Tachibana, Y.; Umekita, K.; Otsuka, Y.; Kuwabata, S. Charge Recombination Kinetics at an in Situ Chemical Bath-Deposited CdS/Nanocrystalline TiO_2 Interface. *J. Phys. Chem. C* **2009**, *113* (16), 6852–6858.

(145) Zhu, W.; Liu, X.; Liu, H.; Tong, D.; Yang, J.; Peng, J. Coaxial Heterogeneous Structure of TiO_2 Nanotube Arrays with CdS as a Superthin Coating Synthesized via Modified Electrochemical Atomic Layer Deposition. *J. Am. Chem. Soc.* **2010**, *132* (36), 12619–12626.

(146) Hwang, I.; Baek, M.; Yong, K. Core/Shell Structured TiO_2/CdS Electrode to Enhance the Light Stability of Perovskite Solar Cells. *ACS Appl. Mater. Interfaces* **2015**, *7* (50), 27863–27870.

(147) Dibbell, R. S.; Watson, D. F. Distance-Dependent Electron Transfer in Tethered Assemblies of CdS Quantum Dots and TiO_2 Nanoparticles. *J. Phys. Chem. C* **2009**, *113* (8), 3139–3149.

(148) Nakamura, R.; Makuta, S.; Tachibana, Y. Electron Injection Dynamics at the SILAR Deposited CdS Quantum Dot/TiO_2 Interface. *J. Phys. Chem. C* **2015**, *119* (35), 20357–20362.

(149) Shao, Z.; Zhu, W.; Li, Z.; Yang, Q.; Wang, G. One-Step Fabrication of CdS Nanoparticle-Sensitized TiO_2 Nanotube Arrays via Electrodeposition. *J. Phys. Chem. C* **2012**, *116* (3), 2438–2442.

(150) Zhu, G.; Pan, L.; Xu, T.; Sun, Z. One-Step Synthesis of CdS Sensitized TiO_2 Photoanodes for Quantum Dot-Sensitized Solar Cells by Microwave Assisted Chemical Bath Deposition Method. *ACS Appl. Mater. Interfaces* **2011**, *3* (5), 1472–1478.

(151) Mazumdar, S.; Roy, K.; Srihari, V.; Umapathy, S.; Bhattacharyya, A. J. Probing Ultrafast Photoinduced Electron Transfer to TiO_2 from CdS Nanocrystals of Varying Crystallographic Phase Content. *J. Phys. Chem. C* **2015**, *119* (30), 17466–17473.

(152) Jin-nouchi, Y.; Naya, S.; Tada, H. Quantum-Dot-Sensitized Solar Cell Using a Photoanode Prepared by in Situ Photodeposition of CdS on Nanocrystalline TiO_2 Films. *J. Phys. Chem. C* **2010**, *114* (39), 16837–16842.

(153) Xie, Y.; Ali, G.; Yoo, S. H.; Cho, S. O. Sonication-Assisted Synthesis of CdS Quantum-Dot-Sensitized TiO_2 Nanotube Arrays with Enhanced Photoelectrochemical and Photocatalytic Activity. *ACS Appl. Mater. Interfaces* **2010**, *2* (10), 2910–2914.

(154) Banerjee, S.; Mohapatra, S. K.; Das, P. P.; Misra, M. Synthesis of Coupled Semiconductor by Filling 1D TiO_2 Nanotubes with CdS. *Chem. Mater.* **2008**, *20* (21), 6784–6791.

(155) Liu, S.; Zhang, N.; Tang, Z.-R.; Xu, Y.-J. Synthesis of One-Dimensional CdS@TiO_2 Core–Shell Nanocomposites Photocatalyst for Selective Redox: The Dual Role of TiO_2 Shell. *ACS Appl. Mater. Interfaces* **2012**, *4* (11), 6378–6385.

(156) Zhang, H.; Zhang, D.; Qin, X.; Cheng, C. Three-Dimensional CdS-Sensitized Sea Urchin Like TiO2-Ordered Arrays as Efficient Photoelectrochemical Anodes. *J. Phys. Chem. C* **2015**, *119* (50), 27875–27881.

(157) Luo, J.; Ma, L.; He, T.; Ng, C. F.; Wang, S.; Sun, H.; Fan, H. J. TiO_2/(CdS, CdSe, CdSeS) Nanorod Heterostructures and Photoelectrochemical Properties. *J. Phys. Chem. C* **2012**, *116* (22), 11956–11963.

(158) Lee, Y.-L.; Chi, C.-F.; Liau, S.-Y. CdS/CdSe Co-Sensitized TiO_2 Photoelectrode for Efficient Hydrogen Generation in a Photoelectrochemical Cell. *Chem. Mater.* **2010**, *22* (3), 922–927.

(159) Awatani, T.; McQuillan, A. J. Adsorbed Thiosulfate Intermediate of Cadmium Sulfide Aqueous Photocorrosion Detected and Characterized by in Situ Infrared Spectroscopy. *J. Phys. Chem. B* **1998**, *102* (21), 4110–4113.

(160) Burke, M. S.; Zou, S.; Enman, L. J.; Kellon, J. E.; Gabor, C. A.; Pledger, E.; Boettcher, S. W. Revised Oxygen Evolution Reaction Activity Trends for First-Row Transition-Metal (Oxy)hydroxides in Alkaline Media. *J. Phys. Chem. Lett.* **2015**, *6* (18), 3737–3742.

(161) Boggs, B. K.; King, R. L.; Botte, G. G. Urea Electrolysis: Direct Hydrogen Production from Urine. *Chem. Commun.* **2009**, No. 32, 4859–4861.

Chapter 2 $Ni(OH)_2$ as Hole Mediator for Visible Light-Induced Urea Splitting

2.1 Introduction

Increasing depletion of fossil fuels and concerns about the environment drive the demand for clean and renewable energy. Hydrogen is a potential substitute for fossil energy due to its ubiquity and environmentally friendly properties.[1-2] Solar-driven methods for the production of hydrogen from water present an ideal path forward since solar energy flux is more than 6,000 times greater than current global energy demand.[3-4] However, direct solar water splitting employing photoelectrochemical reactors suffer predominately from photocorrosion as a result of the slow oxygen evolution reaction (OER) kinetics, which facilitates the more rapid photocorrosion reaction in nearly all visible absorbing semiconductors with appropriate band energies to carry out the necessary redox half reactions. In fact there exists a theoretical relationship between the potential for a semiconductor to undergo photocorrosion and the magnitude of its band gap. Hence, wide band gap semiconductors such as TiO_2 offer stability against photocorrosion in water splitting reactions but are significantly constrained by their inability to capture and convert visible sunlight.

Urea [$CO(NH_2)_2$] is a major component of human urine with a gravimetric hydrogen content of 6.71% and has been proposed as a renewable source of hydrogen.[5] Urea is chemically stable, widely available in global excess, non-toxic, non-flammable, and is the predominant component of human and animal urine, which is produced at rates of millions of tons per day. An economical means to produce hydrogen from urea has been a topic of increasing interest as the

world looks to renewable sources of energy. Decomposition of urea to ammonia with subsequent high temperature cracking is not cost effective for hydrogen extraction, however electrolysis of urea solutions to produce hydrogen has garnered significant research focus.[6-9] Ni-based oxides have been shown to exhibit catalytic behavior toward urea decomposition, which is inspired from the Ni-containing urease metalloenzyme responsible for the hydrolysis of urea in nature. For example, $Ni(OH)_2$ can be employed at the anode while water is reduced at the cathode of a urea electrolysis reactor. Urea has a theoretical oxidation potential (based on Gibb's free energy) of -0.46 V vs. SHE, which brings the thermodynamic operating potential for such an electrolyzer down from 1.23 V to 0.37 V. Mechanisms of biocatalytic[10-12] and electrochemical decomposition of urea over nickel-based catalysts[7] have been investigated experimentally and theoretically and is thought to proceed through NiOOH catalytic intermediate.[6, 9, 11, 13] A photoelectrochemical reactor provides an opportunity to directly convert urea to hydrogen gas, which translates into simultaneous conversion and storage of solar energy. This concept was previously demonstrated using a TiO_2-$Ni(OH)_2$ coupled semiconductor-catalyst architecture.[14] The reactor demonstrated stable photocurrent in 3-electrode configuration over the course of several days, but stability is not an issue for the robust TiO_2 system in aqueous solutions. The limitation presented by TiO_2 in practical solar conversion is its lack of visible light absorption due to wide band gap at 3.5 eV.

In this chapter, we extend the light absorption of the TiO_2-$Ni(OH)_2$ photoelectrode through photosensitization with CdS nanocrystals. CdS-sensitized TiO_2 has been researched extensively as photoanode in quantum dot sensitized solar cells.[15-31] CdS was also an early candidate for solar water splitting, given its straddled conduction and valence band positions relative to the water reduction and oxidation potentials.[32-44] However, OER cannot compete with the water-mediated photocorrosion reaction at the electrode-electrolyte interface, leading to

electrode disintegration and failure.[45-59] The current approach represents a maiden effort in developing a mid-band gap semiconductor-catalyst architecture (CdS-$Ni(OH)_2$) that can harness urea as sacrificial electron donor for the sustainable production of hydrogen by side-stepping OER. We have probed the charge carrier transfer and recombination kinetics to provide insight into the photoelectrochemical performance of the semiconductor-catalyst architecture.

2.2 Experimental

2.2.1 Materials and Methods

Quantum dot-sensitized photoanodes were constructed using a fluorine-doped tin oxide (FTO) as substrate. FTO was cut to 6 cm × 0.8 cm (length × width) and subjected to ultrasonication in detergent solution, deionized water (DI) and ethanol for 30 mins, respectively. Cleaned FTO substrates were immersed in $TiCl_4$ solution (40 mM) and heated to 70 °C for 30 min to deposit a blocking layer, followed by DI and ethanol rinse and then annealed at 500 °C for 30 min. DSL 18NR-T TiO_2 paste was bladed onto a 0.8 cm^2 active area and dried at ambient temperature for 1 h and 80 °C for 1 h, then annealed at 500 °C for 1 h. Finally, a post-$TiCl_4$ solution treatment was conducted to increase the roughness of surface following the same procedure as to deposit the blocking layer. CdS-sensitized TiO_2 photoanodes were prepared via the successive ionic layer absorption and reaction (SILAR) by using cadmium sulfate (0.1 M) solution and sodium sulfide (0.1 M) solution for ten cycles (1 min immersion and 30 s rinse with DI water). $Ni(OH)_2$ was prepared via SILAR by using nickel chloride (0.1 M) solution and sodium hydroxide (0.1 M) solution for 1 cycle (1 min immersion and 30 s rinse with DI water).

2.2.2 Materials Characterization

X-ray diffraction (XRD) analysis was performed using a Bruker D8 diffractometer with Cu Kα as the source. Morphology and composition analysis were carried out by employing a

JEOS JSM-7000F scanning electron microscope (SEM) equipped with energy dispersive X-ray spectroscopy (EDS).

2.2.3 Electrochemical and PEC Measurements

Electrochemical and photoelectrochemical measurements were carried out using a Gamry Interface 1000 potentiostat in a three-electrode configuration. The active area of the photoanode for electrochemical and photoelectrochemical measurement is 0.8 cm^2 and 0.2 cm^2, respectively. A 150 W Xe lamp with an AM 1.5G filter was used to irradiate cells at 100 mW/cm^2. Cyclic voltammetry and linear sweep voltammetry measurements were recorded by sweeping potential at 10 mV/s and 50 mV/s, respectively.

2.2.4 Optical Measurements

An Agilent Cary 60 spectrophotometer was used to record UV - visible absorption spectra of CdS-sensitized TiO_2 electrode (with and without $Ni(OH)_2$). Transient absorption (TA) measurements were recorded using a Clark MXR CPA-2010 (fundamental wavelength 775 nm, pulse duration 150 fs, pulse energy 1 mJ, repetition rate 1 kHz) incorporating Helios software provided by Ultrafast Systems. The fundamental laser output was split into a pump light and a probe light, which account for 95% and 5%, respectively. The probe light beam passed through an optical delay stage and then was focused on a Ti: sapphire crystal to provide a white light continuum. The pump light beam was directed through a second harmonic frequency doubler to produce the 387 nm pump light beam. All samples investigated were placed in a quartz cell. Based on the designed experiment, the quartz cell was pumped vacuum or filled with degassed solution.

2.3 Results and Discussions

2.3.1 Photoanode Fabrication and Characterization

Photoanodes were prepared by employing the successive ionic layer adsorption and reaction (SILAR) procedure for CdS deposition onto mesoscopic TiO_2 architecture to form FTO-TiO_2-CdS electrode. The $Ni(OH)_2$ catalyst layer was subsequently deposited using SILAR with successive immersion into Ni^{2+} ($NiCl_2$) and OH^- (NaOH) baths (CdS-Ni hereafter referring to FTO-TiO_2-CdS-$Ni(OH)_2$ electrode). XRD results presented in Figure 2-1A show peaks associated with crystalline phases on the CdS-Ni electrode, and we observe the successful deposition of β-$Ni(OH)_2$ on cubic CdS film. UV-Visible absorption spectroscopy (UV-Vis) was carried out to evaluate the light absorption of the photoelectrode with and without $Ni(OH)_2$ catalyst layer. Ideally, non-photoactive components of the electrode are transparent to the photons in the region of the semiconductor band gap; otherwise, parasitic light absorption by the catalyst layer reduces the maximum obtainable photoconversion by the semiconductor. A comparison of the UV-Vis spectra for CdS and CdS-Ni electrodes presented in Figure 2-1B show the $Ni(OH)_2$ layer is transparent at all relevant wavelengths, and the CdS absorption onset is ~525 nm. Further characterization using scanning electron microscopy shows the CdS film consists of a highly porous architecture with aggregates of CdS-$Ni(OH)_2$ decorating the surface as observed in Figures 2-1C and 2-1D. EDS analysis further confirms the presence of Ni on the CdS-Ni electrode (Figure 2-1E and table 2-1). The Ni content is minimal (~0.3 atomic %) since $Ni(OH)_2$ was prepared in this sample by 1 immersion cycle using SILAR.

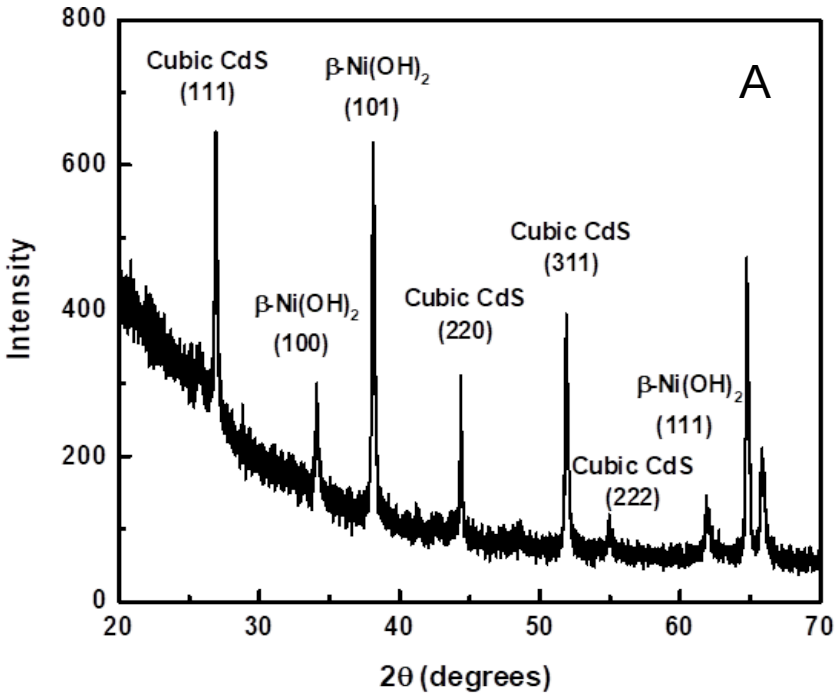
A
Cubic CdS
(111)
β-Ni(OH)2
(101)
β-Ni(OH)2
(100)
Cubic CdS
(220)
Cubic CdS
(311)
Cubic CdS
(222)
β-Ni(OH)2
(111)
Intensity
2θ (degrees)
0
200
400
600
800
20
30
40
50
60
70

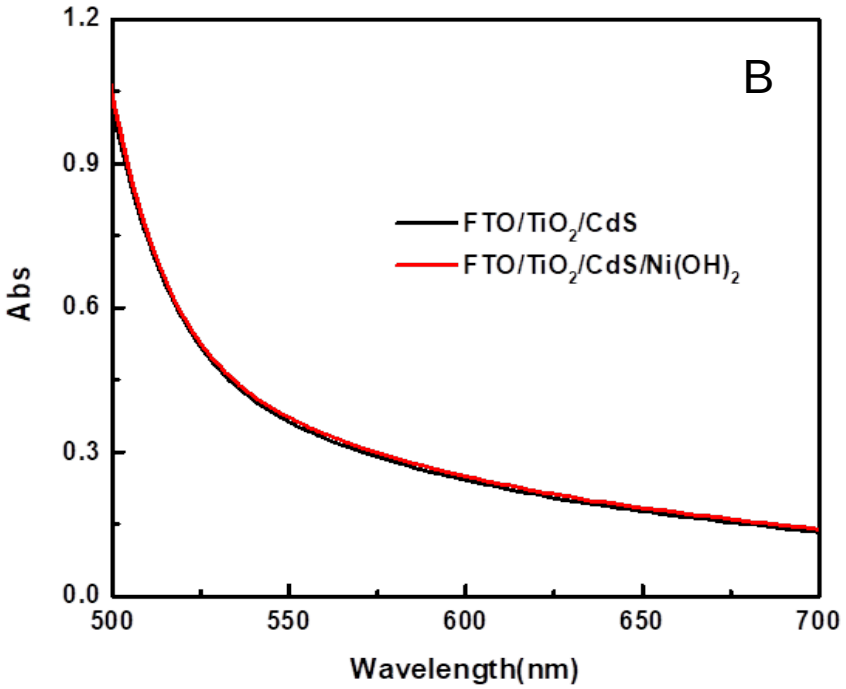
B
FTO/TiO2/CdS
FTO/TiO2/CdS/Ni(OH)2
Abs
Wavelength(nm)
0.0
0.3
0.6
0.9
1.2
500
550
600
650
700

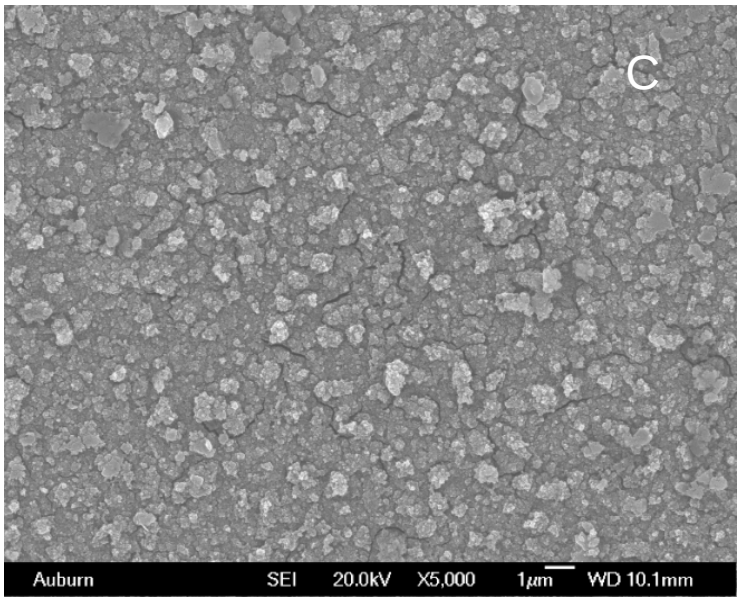
C
Auburn SEI 20.0kV X5,000 1μm WD 10.1mm

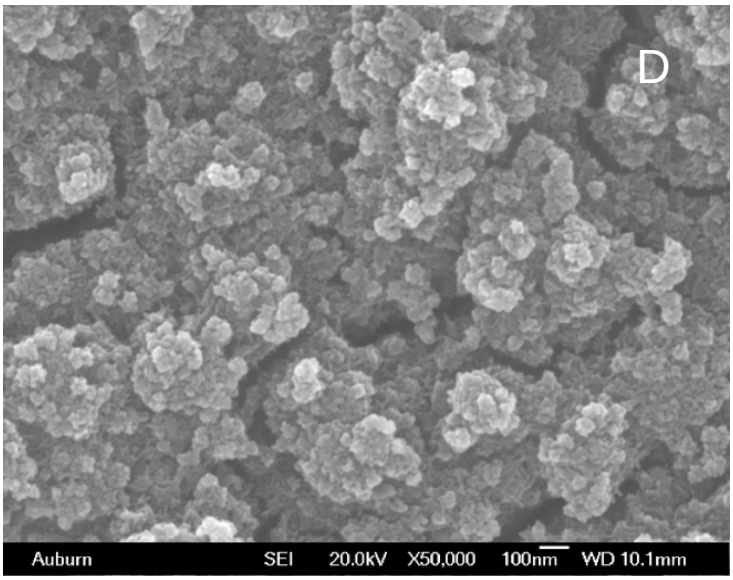
D
Auburn SEI 20.0kV X50,000 100nm WD 10.1mm

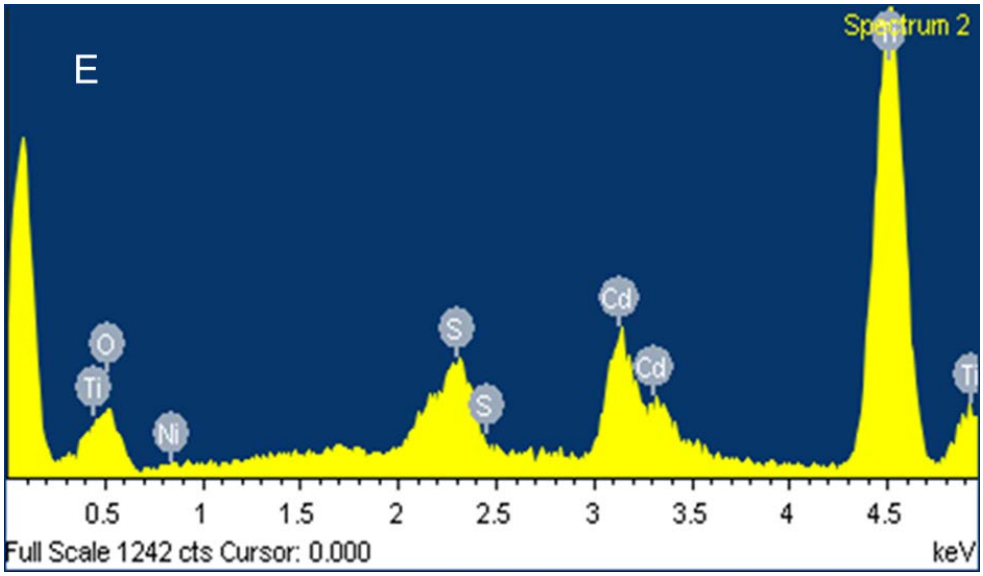

Figure 2-1. Characterization of CdS-Ni photoanode prepared on TiO_2 mesoscopic support. (A) XRD results with characteristic peaks identified for CdS and β-$Ni(OH)_2$, (B) UV-visible absorption spectra comparison between (a) CdS and (b) CdS-Ni, (C-D) scanning electron micrographs of the CdS electrode following $Ni(OH)_2$ deposition. (E) EDS results corresponding to TiO_2/CdS/$Ni(OH)_2$ photoanode. Nickel is detected at very low concentrations as a result of the minimal thickness of the catalyst after only 1 immersion cycle following the SILAR deposition method.

Table 2-1. Composition of TiO_2/CdS/$Ni(OH)_2$

Element	**Weight %**	**Atomic %**
O K	34.20	64.26
S K	3.33	3.12
Ti K	43.78	27.48
Ni K	0.56	0.29
Cd L	18.14	4.85
Totals	100.00	

We employed the SILAR deposition procedure to maximize surface coverage of the TiO_2 architecture and eliminate the insulating surface ligands that accompany pre-synthesized CdS nanocrystals in hot injection methods. SILAR deposition also enables one to build cascade architectures with relative ease. In the present study $Ni(OH)_2$ was subsequently deposited onto CdS nanocrystals based on electrostatic associations between Ni^{2+} and terminal sulfur atoms at the CdS interface to form a cascade energy structure that promotes hole transfer across the semiconductor-catalyst interface. While passivation effects of surface ligands considerably improve photoluminescence yield, provide ideal size control, and enable facile solution handling with regard to the nanocrystals, direct precipitation at the photoanode surface *via* SILAR provides maximum interfacial conformity in the highly tortuous TiO_2 mesoporous support.

2.3.2 Electrochemical and PEC Urea Oxidation

We first subjected a TiO_2-$Ni(OH)_2$ electrode (TiO_2-Ni) prepared without CdS to evaluate the electrochemical response of the catalyst in 1 M NaOH and 1 M NaOH/0.33 M urea electrolyte solutions using cyclic voltammetry (CV). Figure 2-2A depicts the CV scan for the TiO_2-Ni electrode in NaOH electrolyte within the voltage range from 0 to 0.7 V *vs.* Ag/AgCl at a scan rate of 10 mV/s. The anodic scan shows the evolution of oxidation and reduction peaks at c.a. 0.45V and 0.35V vs. Ag/AgCl respectively, which correspond to the Ni^{2+}/Ni^{3+} transition in the $Ni(OH)_2$ catalyst.[14] A TiO_2-Ni electrode was then subjected to CV scan in 1 M NaOH/0.33 M urea electrolyte solution, and the results presented in Figure 2-2B indicate oxidation of urea occurs at the onset potential for the Ni^{2+} catalyst oxidation of 0.45V as observed in the significant increase in current in presence of urea. The observed increase in current density upon introduction of the urea to the electrolyte corresponds to the electrocatalytic activation of Ni^{2+} to Ni^{3+}, which leads to NiOOH formation in presence of OH^-. This finding supports past studies

that have identified NiOOH as the catalytic intermediate driving urea oxidation according to the reaction scheme below.

Anode

$$Ni(OH)_2 + OH^- \rightarrow NiOOH + H_2O + e^-$$

$$6NiOOH + CO(NH_2)_2 \rightarrow 6NiOOH + N_2 + CO_2 + 5H_2O + 6e^-$$

$$NiOOH + H_2O + e^- \rightarrow Ni(OH)_2$$

Cathode

$$6H_2O + 6e^- \rightarrow 3H_2 + 6OH^-$$

Overall

$$CO(NH_2)_2 + H_2O \rightarrow 3H_2 + N_2 + CO_2$$

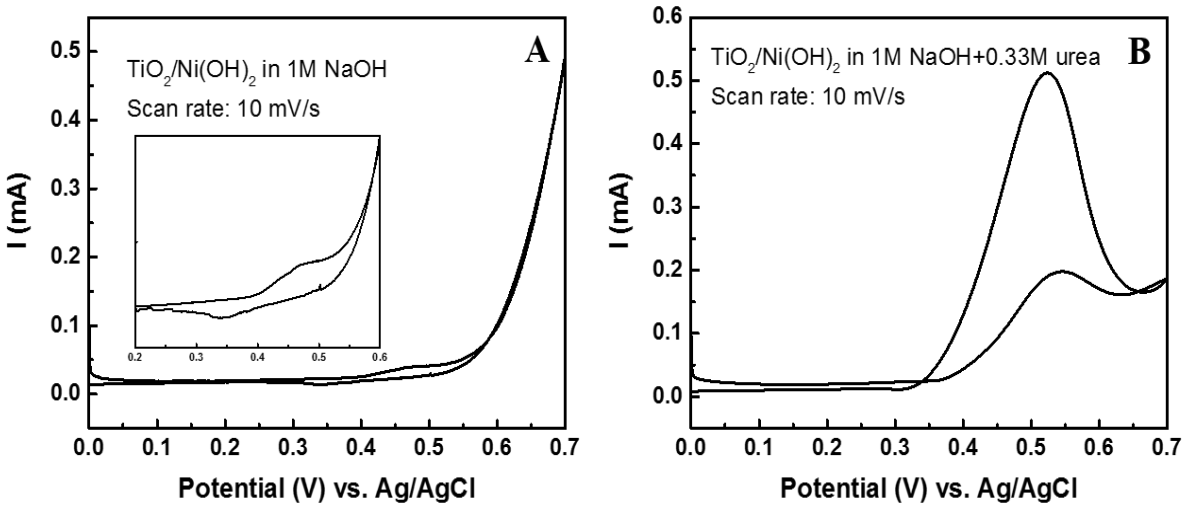

Figure 2-2. Evaluation of $Ni(OH)_2$ electrocatalytic response in 3-electrode cell (A) without urea and (B) in presence of urea. Urea oxidation is catalyzed by the redox activity of $Ni(OH)_2$ in OH^- solution as evident by the strong oxidation peaks at the Ni^{2+}/Ni^{3+} redox potential. Inset of (A) shows the muted redox activity at the Ni^{2+}/Ni^{3+} redox potential when urea is not present.

One interesting observation in the electrochemical testing was the higher current response in the return cathodic scan at the Ni^{2+} oxidation potential. This phenomenon suggests weakly bound adsorbed intermediate species undergo oxidation with faster kinetics at these potentials than the initial urea oxidation step. In fact $Ni(OH)_2$ has been shown to strongly adsorb many intermediate species arising from the complex 6-electron urea oxidation reaction that involves multiple proton transfer steps.[6]

Next, we fabricated CdS-Ni photoanodes and employed them in a 3-electrode photoelectrochemical cell to evaluate the steady state photoresponse of the semiconductor-catalyst architecture in 1M NaOH/0.33 M urea electrolyte under simulated sunlight at 100 mW/cm^2 using AM 1.5 filter. I-V characteristics of the electrode were measured using Pt wire as counter electrode and Ag/AgCl as reference electrode. A linear scan (i.e. LSV) beginning at open circuit voltage and *vs.* Ag/AgCl was carried out to gauge the photoelectrochemical response at various potentials, including the Ni^{2+}/Ni^{3+} activation potential of ~0.45 V. The results of the LSV scans are presented in Figure 2-3A and show several interesting features. First, CdS-Ni electrodes exhibited anodic photocurrent onset just beyond V_{oc} at c.a. -1.0 V with anodic activation of $Ni(OH)_2$ evident around 0.45 V *vs.* Ag/AgCl. As the number of SILAR deposition cycles increases, the photocurrent density increases with a slight lowering of the $Ni(OH)_2$ activation potential. We attribute this finding to improved grain structure and lower electron-hole recombination as the CdS layer is increased. This result suggests the CdS photoanode is capable of hole transfer to $Ni(OH)_2$ and subsequently to urea within the electrolyte solution. We also prepared fresh electrodes to evaluate the stability of the electrodes under constant illumination with on-off cycling. CdS-Ni electrodes were found to be unstable during chronoamperometric testing under continuous illumination as depicted in Figure 2-3B.

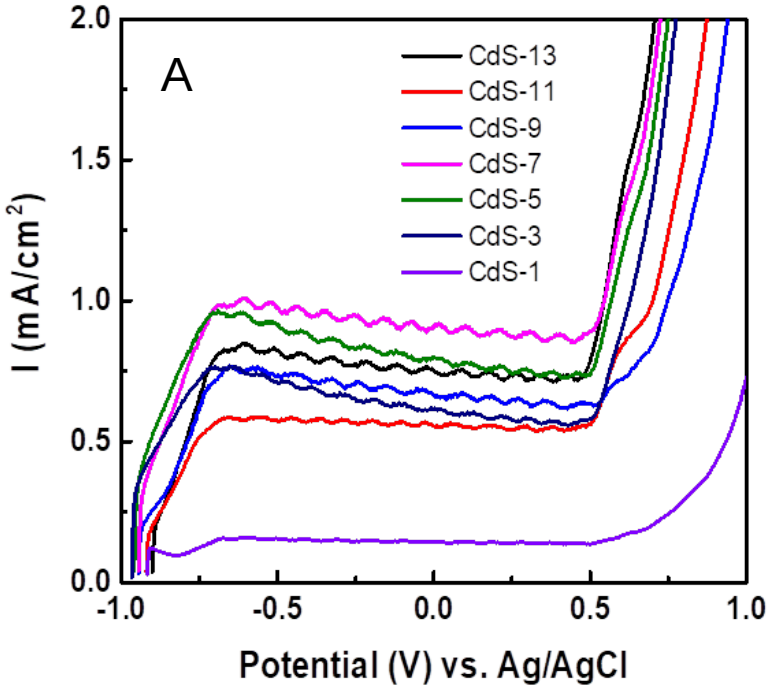
A
CdS-13
CdS-11
CdS-9
CdS-7
CdS-5
CdS-3
CdS-1
I (mA/cm^2)
Potential (V) vs. Ag/AgCl
2.0
1.5
1.0
0.5
0.0
-1.0
-0.5
0.0
0.5
1.0

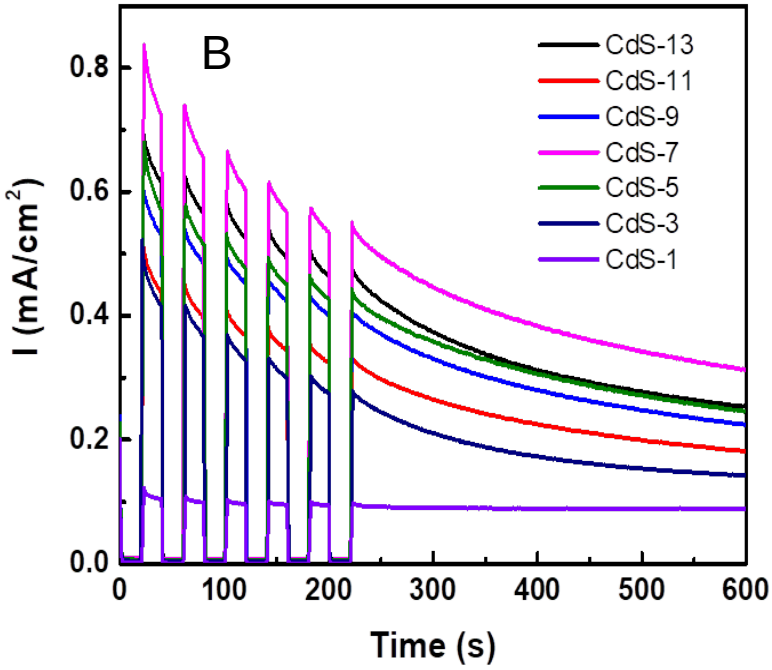
B
CdS-13
CdS-11
CdS-9
CdS-7
CdS-5
CdS-3
CdS-1
I (mA/cm^2)
Time (s)
0.8
0.6
0.4
0.2
0.0
0
100
200
300
400
500
600

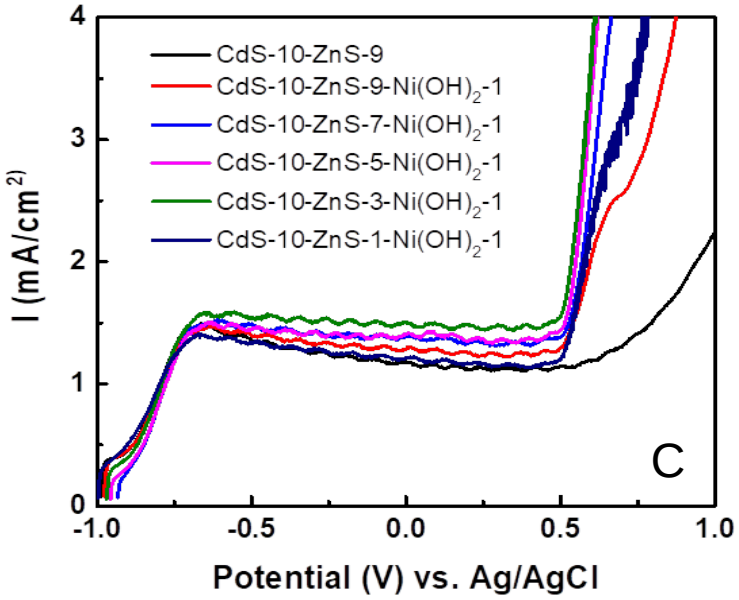

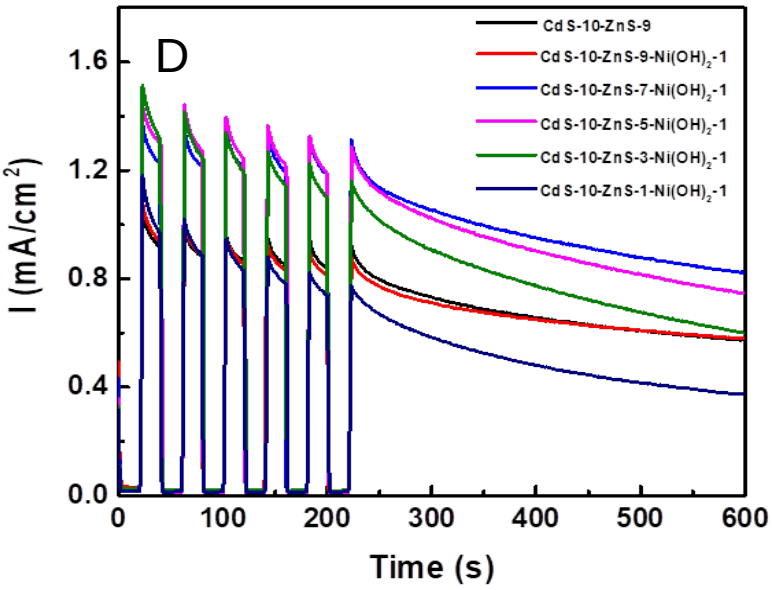

Figure 2-3. LSV and I-t curves of CdS-Ni (A, B) and CdS-ZnS-Ni (C, D) photoanodes in 3-electrode tests using 1 M NaOH + 0.33 M urea electrolyte solutions under illumination using AM 1.5 simulated sunlight. ZnS-coated CdS electrodes demonstrate significant improvement in photostability.

In an attempt to improve the photostability, CdS-Ni electrodes were coated with ZnS passivation layer to minimize electron-hole recombination at surface trap sites while also providing additional protection to the CdS layer from water-mediated photocorrosion reactions. ZnS was deposited onto the photoanode *via* SILAR between the CdS and $Ni(OH)_2$ since its effects are well established on the passivation of chalcogenide surfaces.[24, 60-62] Figure 2-3C shows the beneficial effect of the ZnS passivation by increasing the photocurrent in the LSV scans relative to Figure 2-3A. The photocurrent density slightly decreased with increasing cycles of ZnS (Figure 2-3C), which is expected considering the higher series resistance imparted to the photoanode. Importantly, the photostability depicted in Figure 2-3D shows a drastic improvement relative to the stability of the unpassivated CdS-Ni electrodes shown in Figure 2-3B. Improved coating techniques for conformal ZnS layers coupled with rapid hole transfer kinetics may lead to stable photoanodes in the urea system without any further treatments.

The present challenge in extracting electrons from urea for water reduction is to activate the $Ni(OH)_2$ electrocatalyst *via* interfacial hole transfer from the semiconductor and have the Ni-catalyst serve as a steady-state hole sink for CdS. This eliminates the oxidizing potential from the CdS surface where photocorrosion reactions dominate the fate of the hole. Since the CdS valence band energy lies below the Ni^{2+} oxidation potential on the electrochemical energy scale, the photogenerated hole is thermodynamically favored for transfer across the CdS-$Ni(OH)_2$ interface. Activation of $Ni(OH)_2$ *via* photoinduced hole transfer across the CdS-$Ni(OH)_2$ interface can drive the urea oxidation directly *via* visible light activation of the semiconductor-catalyst assembly. More importantly, during ideal steady-state operation, kinetics of the hole transfer must be of sufficient magnitude relative to parasitic recombination reactions to maintain the CdS-Ni interfacial potential at or beyond the activation potential for the $Ni(OH)_2$. In this case

the Ni-based catalyst will perform similarly as when the potential is driven beyond 0.45 V *vs.* Ag/AgCl by the external bias.

2.3.3 Hole Transfer Kinetics

We employed ultrafast transient absorption spectroscopy (TAS) to probe the evolution and decay of the excited state of the CdS and CdS-Ni photoanodes. TAS is a pump-probe technique whereby the semiconductor is excited by a short pulse (~130 fs) of 387 nm photons, after which a broadband probe is directed at the sample to measure its visible absorption. A second pulse is then directed at the sample without pumping to measure the visible absorption in the ground state. The difference in absorption between the excited and ground states of the semiconductor arises as a result of the difference in the probability of the electronic transitions and/or from the creation of a new light-absorbing species in the excited state. Several pathways exist for electrons and holes to transfer and recombine in the CdS-Ni photoanode when immersed in urea-based electrolytes. Scheme 2-1 depicts a simplified reaction schematic for electrons and holes following photoexcitation with photons equal to or greater than the CdS band gap. Green arrows denote the desirable charge transfer reactions, whereas red arrows indicate parasitic recombination reactions. The current experimental setup employed in this work to measure the charge transfer and recombination rates does not effectively permit evaluation of rate constants for processes 2, 5, and 7. We focused our efforts primarily on those processes that are expected to contribute significantly to the steady state photoconversion efficiency.

In the present work we employed CdS and CdS-Ni photoelectrodes in various experimental regimes to deconvolve the relevant kinetic parameters within the system. Band edge bleaching resulting from population of the conduction band with photoexcited electrons provides a transient signal used to ascertain the rate of depopulation of electrons from the

conduction band. We also observe transient absorption signal in several of the experiments as a result of the formation of a new light absorbing species, which will be discussed in detail in later sections. The decay kinetics of the transient bleach and/or absorption can be fit using linear combination of multiexponential components according to equation 2-1:

$$y = \sum_i A_i e^{-t/\tau_i} \qquad (2\text{-}1)$$

where A_i and τ_i are the relative amplitude and time constant for the ith component, respectively. The average time constant and corresponding rate constant for the excited state decay process can then be calculated using equations (2-2) and (2-3).

$$\tau_{ave} = \frac{\sum A_i \tau_i^2}{\sum A_i \tau_i} \qquad (2\text{-}2)$$

$$k = \frac{1}{\tau_{ave}} \qquad (2\text{-}3)$$

It is instructive to first note the key spectral features corresponding to the ultrafast timescale for the CdS and CdS-Ni photoanodes after undergoing photoexcitation. Spectra corresponding to CdS and CdS-Ni are presented in Figure 2-4 with time delay from 0 – 1 ns. CdS electrode under vacuum exhibits both transient bleaching at 465 nm and transient absorption from 500-700 nm as seen in Figure 2-4A. The transient bleach corresponds to the state filling by excited electrons in the CdS conduction band after excitation by the pump, while the transient absorption is characteristic of the photoinduced formation of $S^{-\bullet}$ resulting from surface-trapped holes at terminal anion sites.[32–36] When the CdS electrode is immersed in the (O_2-free) urea

solution, the transient absorption is shifted and much narrower from 650-750 nm with peak centered around 730 nm as observed in Figure 2-4B. A delay in the rise of the transient absorption was observed relative to the transient bleach in the CdS-vacuum and CdS-urea electrodes, which is indicative of the hole trapping process.[33,37,38] Hole transfer to an adsorbed urea molecule would be expected to initiate the oxidation reaction, which could lead to a radical transition state. We suspect this new peak at 730 nm is associated with a charge transfer or radical cation state arising *via* hole transfer to adsorbed urea. No evidence of this peak was observed in the control experiments with NaOH electrolyte. If we assume the rise of the peak at 730 nm is indicative of the hole transfer reaction to adsorbed urea molecules, the rate constant can be calculated from the rise time of the peak and is reported to be 2.4×10^{12} s^{-1}. Radical transition states of various functionalized urea molecules have been studied in the past using ionizing radiation, and their visible transient absorption spectra are related to the identity of the functional groups and the nature of the radical species.[39] Furthermore, we suspect elimination of $S^{-\bullet}$ transient absorption when CdS is immersed in urea solution arises from surface passivation of unoccupied sulfide bonds by the urea amine group, similar to other amines.[40–43]

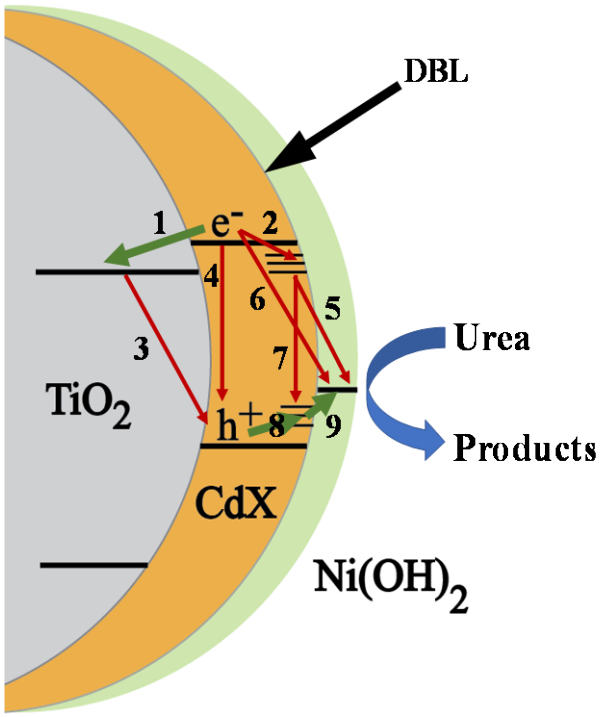

	Physical Process	Rate Constant
1	Electron transfer	k_{et}
2	Electron trapping	$k_{e\text{-}trap}$
3	Back electron transfer	$k_{bt\text{-}1}$
4	Non-radiative recombination	k_{nr}
5	Trap-induced recombination	$k_{t\text{-}rec}$
6	Back electron transfer	$k_{bt\text{-}2}$
7	Trap-induced recombination	$k_{t\text{-}nr}$
8	Surface hole trapping	$k_{h\text{-}trap}$
9	Trap-mediated hole transfer	k_{ht}
10	Urea oxidation	k_{ox}

Scheme 2-1. Schematic representation of the dynamical processes initiated upon photon absorption in a chalcogenide-sensitized electrode architecture with $Ni(OH)_2$ catalyst. The table outlines the photophysical or photochemical process associated with each reaction.

Transient spectra for CdS-Ni electrodes in vacuum and urea electrolyte solution are depicted in Figures 2-4C and 2-4D. CdS-Ni electrode under vacuum shows similar elimination of the $S^{-\bullet}$ transient absorption in favor of a new peak centered at 750 nm. We attribute this peak to Ni^{3+} transient absorption,[44,45] which confirms the photoinduced hole transfer from CdS to Ni-centers within $Ni(OH)_2$ on essentially an identical timescale as hole trapping under vacuum in CdS. Elimination of the hole trapping signal at sulfur terminal sites implies the Ni^{2+} strongly associates with terminal sulfur atoms during SILAR deposition sequence. In the presence of urea, evolution of a broad transient absorption is observed with the CdS-Ni electrode, and we used spectroelectrochemistry to confirm its identity as NiOOH. The broad absorption in Figure 4E with increasing electrolysis time of a FTO-$Ni(OH)_2$ electrode immersed in 1 M NaOH while

applying bias of 0.8 V *vs.* Ag/AgCl matches the transient absorption profile in Figure 2-4D. The electrochemical oxidation of $Ni(OH)_2$ in the presence of OH^- generates NiOOH, which is thought to be the catalytic species in the urea oxidation reaction.[6,46,47] The rise of the broad absorption feature was used to evaluate the hole transfer rate from CdS to $Ni(OH)_2$ as shown in Figure 4F and is calculated to be 7.3×10^{11} s^{-1}, which is slower than the hole transfer rate to urea in the CdS photoanode.

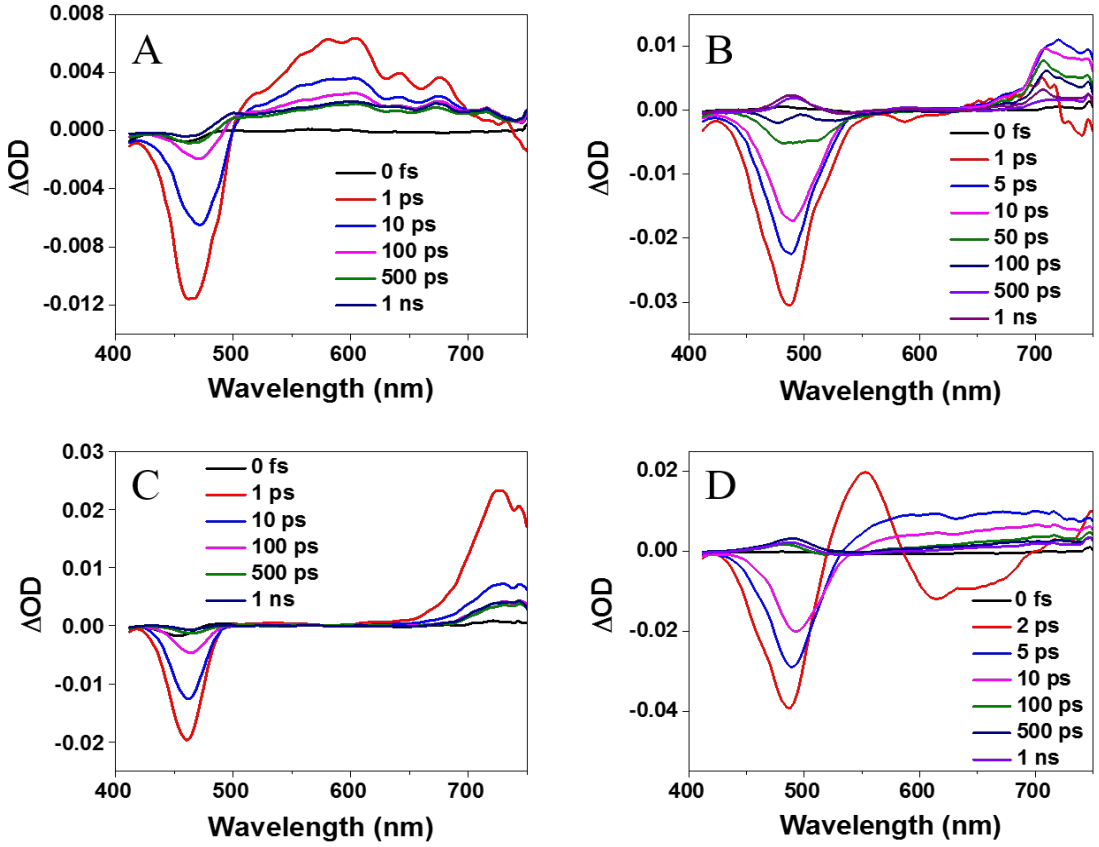

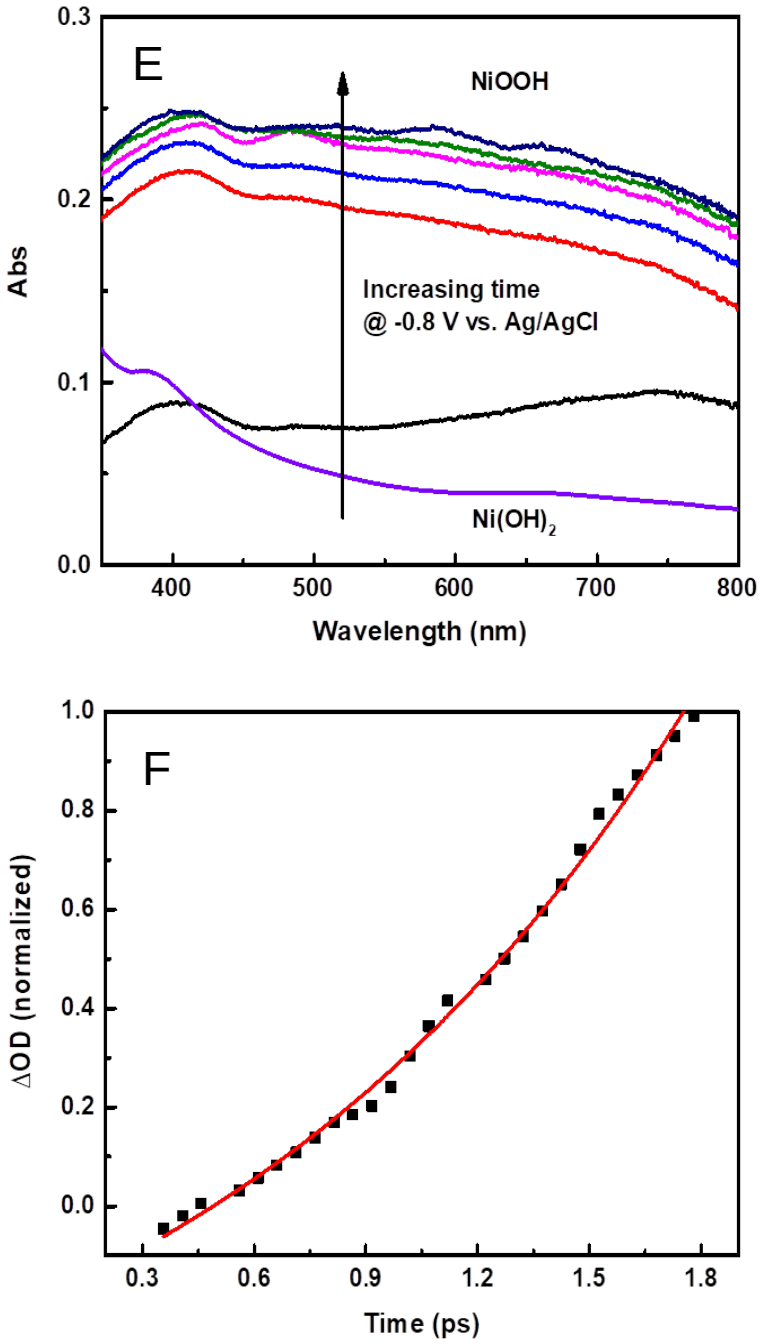

Figure 2-4. Transient absorption spectra for (A) CdS in vacuum, (B) CdS in 1 M NaOH+0.33 M urea, (C) CdS-Ni in vacuum, and (D) CdS-Ni in 1 M NaOH+0.33 M urea. Spectroelectrochemistry was employed to identify the broad transient absorption in (D) from 550 nm – 750 nm as NiOOH as observed in (E), the electrochemical reaction product of $Ni(OH)_2$ oxidation in basic pH electrolytes. Hole transfer rates are extracted by fitting signal rise time to exponential rise in (F).

2.3.4 Hole Transfer Rate from NiOOH to Urea

To study the hole transfer from NiOOH to urea, we monitored the decay rates of the transient absorption related to NiOOH by immersion of CdS-Ni in NaOH and NaOH/urea. When CdS-Ni is immersed only in NaOH, the transient absorption decay is related to the recombination of CdS conduction band electrons with NiOOH, and the decay rate constant is given as $k_{NaOH} = k_{bt-2}$. When CdS-Ni is immersed in NaOH/urea, the hole transfer from NiOOH to urea, represented as k_{ht-2} in Scheme 1, also contributes to the transient absorption decay. The decay rate can be represented as $k_{NaOH-urea} = k_{bt-2} + k_{ht-2}$. The transient absorption decay for each of the experimental conditions was fit to the minimum number of components using equation 2-1 (Figure 2-5), and the average decay times are 162.73 ps and 97.09 ps for CdS-Ni in NaOH and in NaOH/urea, respectively. The hole transfer rate from NiOOH to urea can be obtained by calculating the difference in absorption decay rate between CdS-Ni electrode immersed in NaOH and in NaOH/urea, $k_{ht-2} = k_{NaOH-urea} - k_{NaOH}$, which is calculated to be $4.2\times10^{9}\ s^{-1}$.

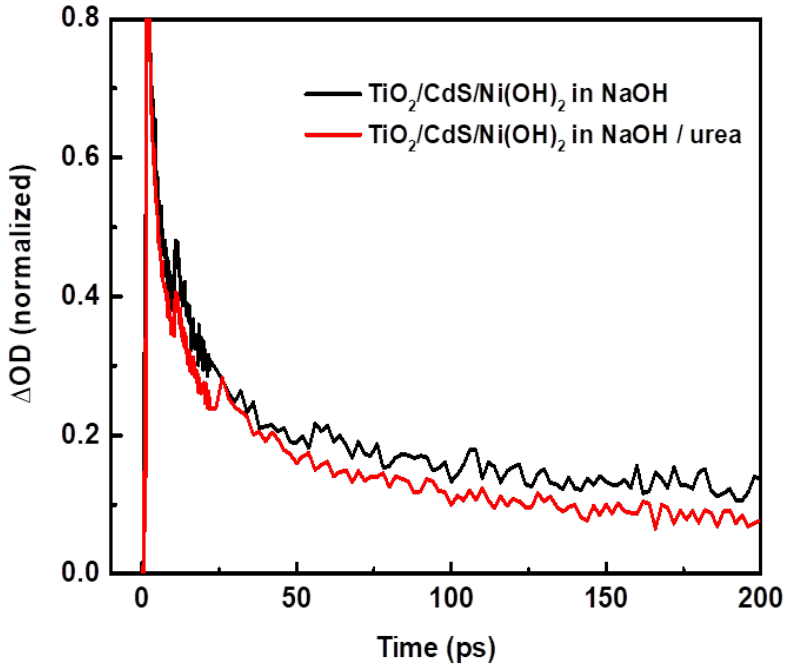

Figure 2-5. Transient absorption decay of TiO_2-CdS-$Ni(OH)_2$ in 1M NaOH and 1M NaOH + 0.33 M urea.

2.3.5 Recombination in CdS-Ni Photoanodes

The CdS-Ni electrode introduces an additional interface (CdS-$Ni(OH)_2$) that can serve as a charge carrier recombination center. Electrons residing in the CdS conduction band are favored thermodynamically to recombine with holes transferred to $Ni(OH)_2$ and reduce the oxidized Ni^{3+} state. This pathway competes directly with the hole transfer reaction to urea at the $Ni(OH)_2$-electrolyte interface, which we suspect reduces the yield of photooxidized urea through competition kinetics. In order to measure the back electron transfer rate from the CdS conduction band to NiOOH, we monitored the CdS transient bleach decay on insulating SiO_2 support with and without $Ni(OH)_2$ catalyst layer. Since the bleach recovery is related to the depopulation of the conduction band in CdS, we compared the relative rates for the SiO_2-CdS and SiO_2-CdS-Ni photoanodes to estimate the back electron transfer rate, k_{bt-2}, represented as reaction 6 in Scheme

2-1. The bleach recovery rate in the SiO_2-CdS electrode is related to the non-radiative recombination rate and is calculated as $k_{nr} = 1/\tau_{CdS}$. For the SiO_2-CdS-Ni electrode the bleach recovery is related to the linear combination of non-radiative recombination and back electron transfer from CdS to $Ni(OH)_2$ and can be expressed as $1/\tau_{CdS-Ni(OH)2} = k_{nr} + k_{bt-2}$. The difference in the rate of bleaching recovery in these electrodes can be used to estimate the back electron transfer rate accordingly $k_{bt-2} = 1/\tau_{CdS-Ni(OH)2} - 1/\tau_{CdS}$. Figure 2-6 shows the exponential bleaching recovery for each of the electrodes, which was fit to the minimum number of components using equation 2-1. The obtained average bleach recovery times for SiO_2-CdS in vacuum and SiO_2-CdS-Ni in NaOH/urea are 214.42 ps and 160.66 ps, respectively. The back electron transfer rate from CdS to $Ni(OH)_2$ is then calculated to be 1.56×10^9 s^{-1}. This rate is comparable to the hole transfer rate from NiOOH to urea, which facilitates recombination and lower efficiency. We note here the necessity of the difference in experimental conditions (vacuum *vs.* electrolyte) since carrying out photoexcitation of CdS in electrolyte leads to photocorrosion reactions. Further, to gauge the back electron transfer from CdS to NiOOH, stable electrolyte solution with NaOH and urea must be provided for conversion of $Ni(OH)_2$ to NiOOH.

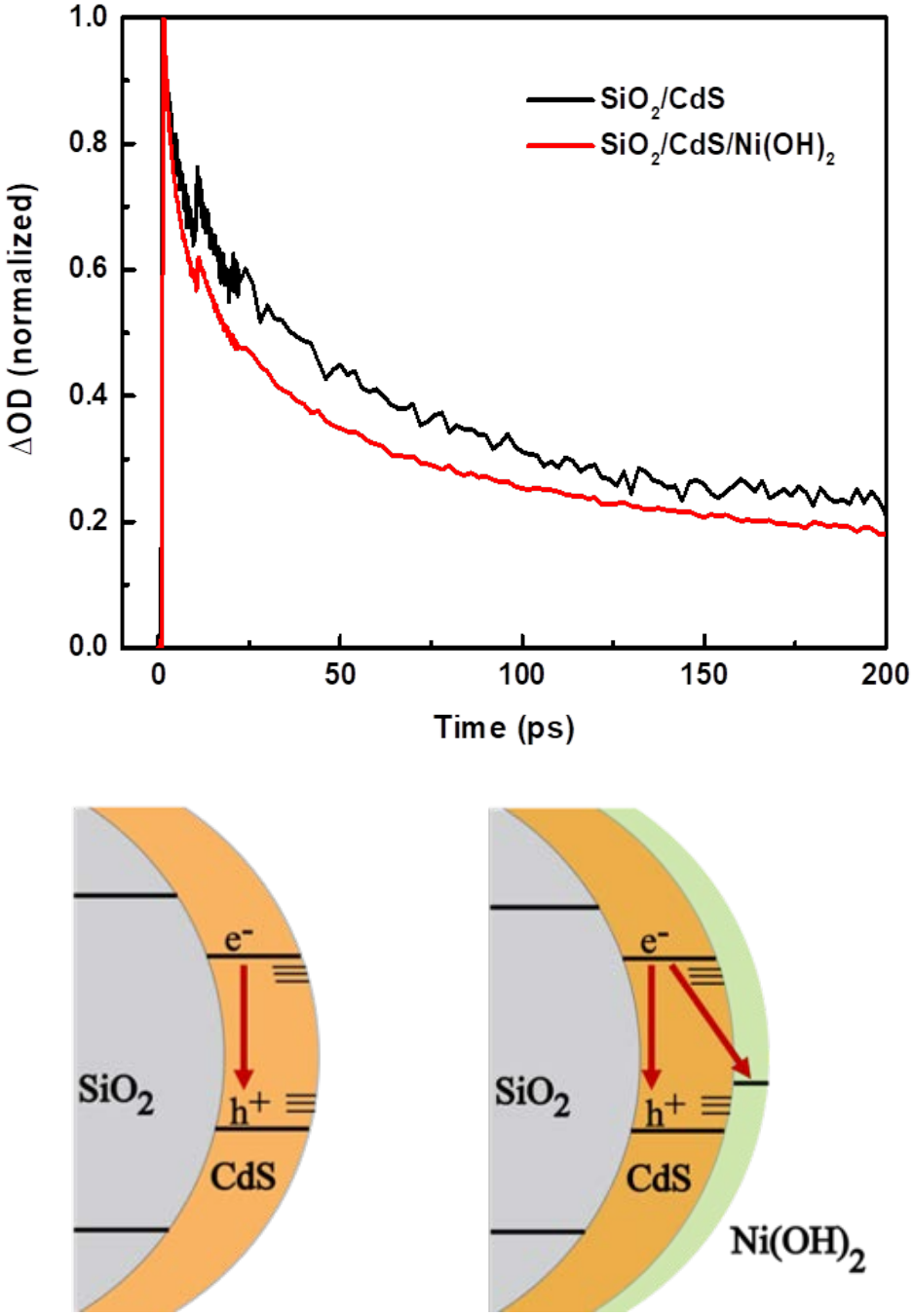

Figure 2-6. Transient bleaching recovery at band edge for (a) CdS in vacuum and (b) CdS-Ni in 1 M NaOH+0.33 M urea solution. The schematic below shows the recombination pathways that are involved in the processes, which allows us to deconvolve the back electron transfer rate from CdS conduction band to NiOOH (oxidized form of $Ni(OH)_2$, which implies hole transfer from CdS to $Ni(OH)_2$ must occur before k_{bt-2}).

2.3.6 Electron Transfer from CdS and Back Transfer

In order to provide a clear and complete picture for the charge carrier transfer and recombination rates, we investigated the electron transfer rate from CdS to TiO_2 (pathway 1 in Scheme 1) and the back electron transfer rate from CdS valence band holes (pathway 3 in Scheme 2-1). Transient absorption spectroscopy was carried out for SiO_2-CdS-Ni and TiO_2-CdS-Ni in 1M NaOH/0.33M urea solution. Photoexcited electrons from CdS will transfer to TiO_2 due to the offset in CdS and TiO_2 conduction bands. When CdS is deposited on an insulator support such as SiO_2, pathway 1 corresponding to electron transfer from CdS to SiO_2 is blocked. The bleach recovery rate in SiO_2-CdS-Ni is attributed to non-radiative recombination of electrons and holes in addition to back electron transfer from CdS to NiOOH. For TiO_2-CdS-Ni, the bleach recovery rate is further influenced by deactivation pathway 1, electron transfer from TiO_2 to CdS. We observe a faster bleach recovery rate in TiO_2-CdS-Ni compared to that in SiO_2-CdS-Ni (Figure 2-7). The bleach recovery rates in TiO_2-CdS-Ni and SiO_2-CdS-Ni can be expressed as $k_{CdS-TiO2} = k_{nr} + k_{bt-2} + k_{et}$ and $k_{CdS-SiO2} = k_{nr} + k_{bt-2}$, respectively. The electron transfer rate, k_{et}, can be obtained from the difference in the rates for each of the electrodes, given as $k_{et} = k_{CdS-TiO2} - k_{CdS-SiO2}$. The average time constants for bleach recovery in TiO_2-CdS-Ni and SiO_2-CdS-Ni electrode are 126.6 ps and 160.7 ps, respectively. Then according to equation (3), the electron transfer rate from CdS to TiO_2 is calculated as $1.68\times10^{9}\ s^{-1}$, which is comparable with previously reported rates for electron transfer at the TiO_2-CdS interface.[48]

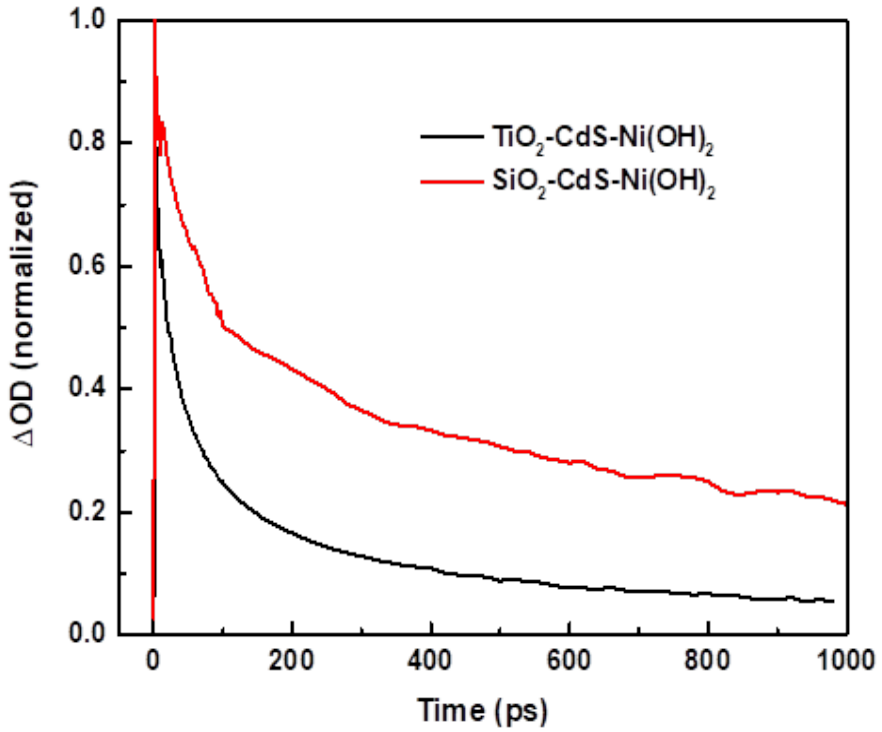

Figure 2-7. Electron decay kinetics of TiO_2-CdS-$Ni(OH)_2$ and SiO_2-CdS-$Ni(OH)_2$ in 1M NaOH+0.33 M urea.

The back electron transfer from CdS also contributes to the decay of the NiOOH transient absorption. We confirmed the back electron transfer rate in similar fashion by calculating the difference in the transient absorption decay rate (corresponding to NiOOH) in the two electrodes. The absorption decay was fit with the minimum number of components using equation 2-1, and the average decay times for TiO_2-CdS-Ni and SiO_2-CdS-Ni in NaOH/urea are 97 ps and 113 ps, respectively. The back electron transfer rate, k_{bt-1}, from is calculated at 1.47×10^9 s^{-1}, which essentially the same rate obtained in the prior experiments using SiO_2-CdS in vacuum and SiO_2-CdS-Ni in urea electrolyte.

Moreover, the introduction of ZnS passivation layer decreases the bleach recovery rate by ~43% ($<\tau_{ZnS}>$ = 222.9 ps; $<\tau_{no\text{-}ZnS}>$ = 126.6 ps) (Figure 2-8). These findings highlight the

passivating effect of ZnS between the CdS and $Ni(OH)_2$ interface as well as the overall challenge in mitigating the photoanode recombination reactions in the cascade electrode assemblies.

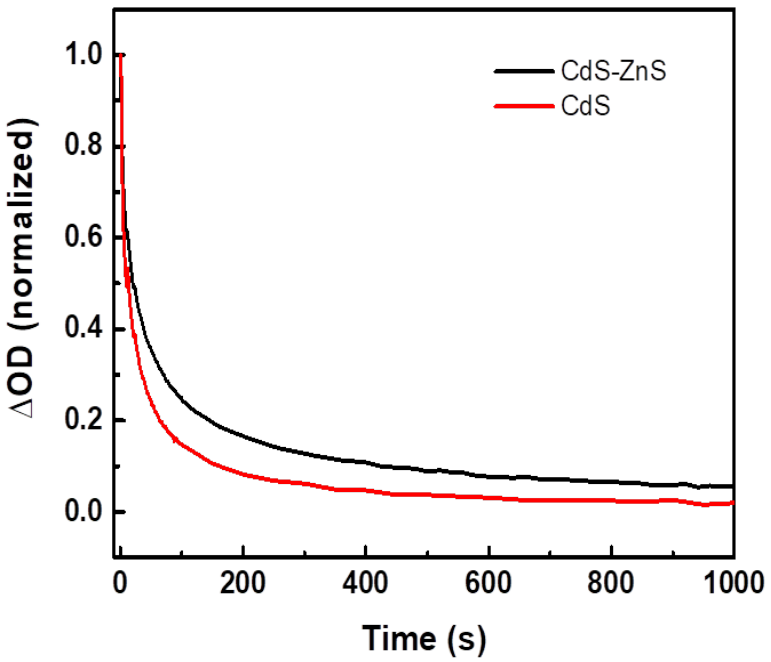

Figure 2-8. Bleach decay of TiO_2-CdS- $Ni(OH)_2$ and TiO_2-CdS-ZnS-$Ni(OH)_2$ in 1M NaOH +0.33 M urea.

A summary of the charge transfer and recombination rates corresponding to the most relevant and accessible pathways in Scheme 1 and 95% confidence interval are summarized below in table 2-2.

Table 2-2. Charge transfer and recombination rates associated with each reaction

Rate	Physical process	Rate constant (s^{-1}) 95% confidence interval
k_{et}	Electron transfer from CdS to TiO_2	$(1.7 \pm 0.25) \times 10^9$
k_{bt-1}	Back electron transfer from TiO_2	$(1.5 \pm 0.089) \times 10^9$
k_{nr}	Non-radiative recombination	$(4.7 \pm 0.17) \times 10^9$
k_{bt-2}	Back electron transfer from CdS	$(1.6 \pm 0.067) \times 10^9$
k_{ht-1}	Hole transfer from CdS to $Ni(OH)_2$	$(7.3 \pm 0.28) \times 10^{11}$
k_{ht-2}	Hole transfer from $Ni(OH)_2$ to urea	$(4.2 \pm 0.11) \times 10^9$
k_{ht-3}	Hole transfer from CdS to urea	$(2.4 \pm 0.55) \times 10^{12}$

2.4 Summary

CdS/$Ni(OH)_2$ architecture demonstrates proper energy alignment and rapid hole transfer from CdS to $Ni(OH)_2$ for catalyst activation ($k_{ht} \sim 10^{11}$ s^{-1}). NiOOH mediates urea oxidation through redox-facilitated charge transfer reaction, and back electron transfer from CdS to NiOOH is highly competitive ($k_{ht-2} \sim k_{bt-2} \sim 10^9$ s^{-1}). This back electron transfer leads to lower photocurrent when $Ni(OH)_2$ is deposited directly onto CdS. Introduction of ZnS reduces the interfacial recombination rate and improves the photocurrent density and photostability. Back electron transfer from CdS to NiOOH was found to be highly competitive with the hole transfer from NiOOH to urea, which is expected to result in lower steady state photocurrent. The reported results demonstrate for the first time a mid-gap semiconductor-catalyst architecture with proper band alignment for hole transfer that can be used to produce hydrogen gas from urine waste in a

photoelectrochemical reactor. Further work must be carried out to understand how to better insulate the photoanodes against photocorrosion reactions and minimize parasitic back electron transfer reactions in CdS-Ni photoanodes.

References

(1) Walter, M. G.; Warren, E. L.; McKone, J. R.; Boettcher, S. W.; Mi, Q.; Santori, E. A.; Lewis, N. S. Solar Water Splitting Cells. *Chem. Rev.* **2010,** *110* (11), 6446-6473.

(2) Satyapal, S.; Petrovic, J.; Read, C.; Thomas, G.; Ordaz, G. The U.S. Department of Energy's National Hydrogen Storage Project: Progress Towards Meeting Hydrogen-Powered Vehicle Requirements. *Catal. Today* **2007,** *120* (3), 246-256.

(3) Graetzel, M. The Artificial Leaf, Molecular Photovoltaics Achieve Efficient Generation of Electricity from Sunlight. *Coord. Chem. Rev.* **1991,** *111* (167), 167-174.

(4) Lewis, N. S.; Nocera, D. G. Powering the Planet: Chemical Challenges in Solar Energy Utilization. *Proceedings of the National Academy of Sciences of the United States of America* **2006,** *103* (43), 15729-15735.

(5) Rollinson, A. N.; Jones, J.; Dupont, V.; Twigg, M. V. Urea as a Hydrogen Carrier: A Perspective on Its Potential for Safe, Sustainable and Long-Term Energy Supply. *Energ. Environ. Sci.* **2011,** *4* (4), 1216-1224.

(6) Daramola, D. A.; Singh, D.; Botte, G. G. Dissociation Rates of Urea in the Presence of NiOOH Catalyst: A DFT Analysis. *J. Phys. Chem. A* **2010,** *114* (43), 11513-11521.

(7) Boggs, B. K.; King, R. L.; Botte, G. G. Urea Electrolysis: Direct Hydrogen Production from Urine. *Chem. Comm.* **2009,** *32*, 4859-4861.

(8) Shigeyoshi, M.; Koichi, K.; Nobuyoshi, B. Formation of Nickel Oxyhydroxide Thin Films by Electrodepositon and Their Electrochromic Characteristics. *Jpn. J. Appl. Phys.* **1988,** *27* (2R), 314.

(9) Wang, D.; Botte, G. G. In Situ X-Ray Diffraction Study of Urea Electrolysis on Nickel Catalysts. *ECS Electrochem. Lett.* **2014,** *3* (9), H29-H32.

(10) Benini, S.; Rypniewski, W. R.; Wilson, K. S.; Miletti, S.; Ciurli, S.; Mangani, S. A New Proposal for Urease Mechanism Based on the Crystal Structures of the Native and Inhibited Enzyme from Bacillus Pasteurii: Why Urea Hydrolysis Costs Two Nickels. *Struct.* **1999,** *7* (2), 205-216.

(11) Zambelli, B.; Musiani, F.; Benini, S.; Ciurli, S. Chemistry of Ni^{2+} in Urease: Sensing, Trafficking, and Catalysis. *Acc. Chem. Res.* **2011,** *44* (7), 520-530.

(12) Barrios, A. M.; Lippard, S. J. Interaction of Urea with a Hydroxide-Bridged Dinuclear Nickel Center: An Alternative Model for the Mechanism of Urease. *J. Am. Chem. Soc.* **2000,** *122* (38), 9172-9177.

(13) Suárez, D.; Díaz, N.; Merz, K. M. Ureases: Quantum Chemical Calculations on Cluster Models. *J. Am. Chem. Soc.* **2003,** *125* (50), 15324-15337.

(14) Wang, G.; Ling, Y.; Lu, X.; Wang, H.; Qian, F.; Tong, Y.; Li, Y. Solar Driven Hydrogen Releasing from Urea and Human Urine. *Energ.Environ. Sci.* **2012,** *5* (8), 8215-8219.

(15) Nirmal, M.; Brus, L. Luminescence Photophysics in Semiconductor Nanocrystals. *Acc. Chem. Res.* **1999,** *32* (5), 407-414.

(16) Morgan, N. Y.; Leatherdale, C. A.; Drndic, M.; Jarosz, M. V.; Kastner, M. A.; Bawendi, M. Electronic Transport in Films of Colloidal CdSe Nanocrystals. *Phys. Rev. B* **2002,** *66* (7), art. no.-075339.

(17) Rabani, E.; Hetenyi, B.; Berne, B. J.; Brus, L. E. Electronic Properties of CdSe Nanocrystals in the Absence and Presence of a Dielectric Medium. *J. Chem. Phys.* **1999,** *110* (11), 5355-5369.

(18) Reiss, P.; Bleuse, J.; Pron, A. Highly Luminescent CdSe/ZnSe Core/Shell Nanocrystals of Low Size Dispersion. *Nano Lett.* **2002,** *2* (7), 781-784.

(19) Dantas, N. O.; Qu, F.; Silva, R. S.; Morais, P. C. Anti-Stokes Photoluminescence in Nanocrystal Quantum Dots. *J. Phys. Chem. B* **2002,** *106*, 7453-7457.

(20) Kamat, P. V. Quantum Dot Solar Cells. The Next Big Thing in Photovoltaics. *J. Phys. Chem. Lett.* **2013,** *4* (6), 908-918.

(21) Baker, D. R.; Kamat, P. V. Tuning the Emission of CdSe Quantum Dots by Controlled Trap Enhancement. *Langmuir* **2010,** *26* (13), 11272-11276.

(22) Hines, D. A.; Kamat, P. V. Quantum Dot Surface Chemistry: Ligand Effects and Electron Transfer Reactions. *J. Phys. Chem. C* **2013,** *117* (27), 14418-14426.

(23) Harris, C.; Kamat, P. V. Photocatalytic Events of CdSe Quantum Dots in Confined Media. Electrodic Behavior of Coupled Platinum Nanoparticles. *ACS Nano* **2010,** *4* (12), 7321-7330.

(24) Abazovic, N. D.; Kuljanin-Jakovljevic, J. Z.; Comor, M. I. Optical Properties of CdSe and CdSe/ZnS Quantum Dots Dispersed in Solvents of Different Polarity. *Russ. J. Phys. Chem. A* **2009,** *83* (9), 1511-1514.

(25) Monte, A. F. G.; Rabelo, D.; Morais, P. C. Optical Properties of CdS Nanoparticles Embedded in Polymeric Microspheres. *J. Alloys Compd.* **2010,** *495* (2), 436-438.

(26) Leatherdale, C. A.; Woo, W.-K.; Mikulec, F. V.; Bawendi, M. G. On the Absorption Cross Section of CdSe Nanocrystal Quantum Dots. *J. Phys. Chem. B* **2002,** *106*, 7619-7622.

(27) Murray, C.; Norris, D.; Bawendi, M. Synthesis and Characterization of Nearly Monodisperse CdE (E=S, Se, Te) Semiconductor. *J. Am. Chem. Soc.* **1993,** *115*, 8706-8715.

(28) Jiang, H. X.; Baum, D.; Honig, A. Dynamics and Spatial Distribution of Edge Luminescence Generators in CdS from Time-Resolved Excitation Spectroscopy. *J. Lumin.* **1988,** *41* (557), 557-558.

(29) Egorov, V. D.; Floegel, P.; Nguyen, H. X.; Kaschke, M. Picosecond Transient Optical Nonlinearities in CdS and CdSe. *Phys. Status Solidi B* **1988,** *146* (1), 351-356.

(30) Stramel, R. D.; Nakamura, T.; Thomas, J. K. Photophysical and Photochemical Properties of CdS with Limited Dimensions. *J. Chem. Soc., Faraday Trans* **1988,** *84* (5), 1287-1300.

(31) Wang, Y.; Herron, N. Photoluminescence and Relaxation Dynamics of CdS Superclusters in Zeolites. *J. Phys. Chem.* **1988,** *92* (17), 4988-4994.

(32) Kakuta, N.; Park, K. H.; Finlayson, M. F.; Ueno, A.; Bard, A. J.; Campion, A.; Fox, M. A.; Webber, S. E.; White, J. M. Photoassisted Hydrogen Production Using Visible Light and Coprecipitated ZnS·CdS without a Noble Metal. *J. Phys. Chem.* **1985,** *89* (5), 732-734.

(33) Taqui Khan, M. M.; Bhardwaj, R. C.; Jadhav, C. M. Photocatalytic H_2 and O_2 Generation from Water Using a CdS Dispersion Loaded with Pt, Ir, or Rh and RuO_2. Use of $[\{Ru(OH)(EDTA)\}_2(O_2)]$ as an Electron Relay (H_4EDTA = Ethylenediaminetetra-Acetic Acid). *J. Chem. Soc., Chem. Commun* **1985,** *2*, 1690-1692.

(34) Thewissen, D. H. M. W.; Timmer, K.; van, d. Z. A. E. A.; Tinnemans, A. H. A.; Mackor, A. Preparation of Active CdS/RuO_x Particles for the Photogeneration of H_2. *J. Chem. Soc., Chem. Commun* **1985,** January.

(35) Kaneko, M.; Okada, T.; Teratani, S.; Taya, K. Visible Light Cleavage of Water by CdS Photoanode Coated with Polymer-Pendant $Ru(Bpy)^{32+}$ Film Containing RuO_2 Dispersions. *Electrochim. Acta* **1987,** *32* (9), 1405-1407.

(36) Kobayashi, J.; Kitaguchi, K.; Tanaka, H.; Tsuiki, H.; Ueno, A. Photogeneration of Hydrogen from Water over an Alumina- Supported ZnS-CdS Catalyst. *J. Chem. Soc., Faraday Trans* **1987,** *83* (5), 1395-1404.

(37) Graetzel, M. Recent Advances in Sensitized Mesoscopic Solar Cells. *Acc. Chem. Res.* **2009,** *42* (11), 1788-1798.

(38) Harris, C. T.; Kamat, P. V. Photocatalysis with CdSe Nanoparticles in Confined Media: Mapping Charge Transfer Events in the Subpicosecond to Second Timescales. *ACS Nano* **2009,** *3* (3), 682-690.

(39) Hensel, J.; Wang, G. M.; Li, Y.; Zhang, J. Z. Synergistic Effect of Cdse Quantum Dot Sensitization and Nitrogen Doping of TiO_2 Nanostructures for Photoelectrochemical Solar Hydrogen Generation. *Nano Lett.* **2010,** *10* (2), 478-483.

(40) Wang, G. M.; Yang, X. Y.; Qian, F.; Zhang, J. Z.; Li, Y. Double-Sided CdS and CdSe Quantum Dot Co-Sensitized ZnO Nanowire Arrays for Photoelectrochemical Hydrogen Generation. *Nano Lett.* **2010,** *10* (3), 1088-1092.

(41) Jia, L.; Wang, D. H.; Huang, Y. X.; Xu, A. W.; Yu, H. Q. Highly Durable N-Doped Graphene/CdS Nanocomposites with Enhanced Photocatalytic Hydrogen Evolution from Water under Visible Light Irradiation. *J. Phys. Chem. C* **2011,** *115* (23), 11466-11473.

(42) Li, Q.; Guo, B. D.; Yu, J. G.; Ran, J. R.; Zhang, B. H.; Yan, H. J.; Gong, J. R. Highly Efficient Visible-Light-Driven Photocatalytic Hydrogen Production of CdS-Cluster-Decorated Graphene Nanosheets. *J. Am. Chem. Soc.* **2011,** *133* (28), 10878-10884.

(43) Tongying, P.; Vietmeyer, F.; Aleksiuk, D.; Ferraudi, G. J.; Krylova, G.; Kuno, M. Double Heterojunction Nanowire Photocatalysts for Hydrogen Generation. *Nanoscale* **2014,** *6* (8), 4117-4124.

(44) Zhukovskyi, M.; Tongying, P.; Yashan, H.; Wang, Y.; Kuno, M. Efficient Photocatalytic Hydrogen Generation from Ni Nanoparticle Decorated CdS Nanosheets. *ACS Catal.* **2015**, *5*, 6615-6623.

(45) Bolts, J. M.; Bocarsly, A. B.; Palazzotto, M. C.; Walton, E. G.; Lewis, N. S.; Wrighton, M. S. Chemically Derivatized N-Type Silicon Photoelectrodes. Stabilization to Surface Corrosion in Aqueous Electrolyte Solutions and Mediation of Oxidation Reactions by Surface-Attached Electroactive Ferrocene Reagents. *J. Am. Chem. Soc.* **1979,** *101* (6), 1378-1385.

(46) Frese, K. Electrochemical Studies of Photocorrosion of N-CdSe. *J. Electrochem. Soc.* **1983,** *130* (1), 28-33.

(47) Dewitt, R.; Kirsch, D. M. A. Polycrystalline CdS Photocorrosion Studied by Capacitance and Action Spectra Measurements. *Appl. Phys. Lett.* **1984,** *45* (2), 146-147.

(48) Frese, K. W. J.; Canfield, D. Photocorrosion of N-CdSe in Sulfide Electrolytes. *J. Electrochem. Soc.* **1985,** *132* (7), 1649-1655.

(49) Graetzel, M.; Kiwi, J.; Morrison, C. L.; Davidson, R. S.; Tseung, A. C. C. Visible-Light-Induced Photodissolution of a-Fe_2O_3 Powder in the Presence of Chloride Anions. *J. Chem. Soc., Faraday Trans* **1985,** *81* (8), 1883-1890.

(50) Meissner, D.; Memming, R.; Li, S.; Yesodharan, S.; Graetzel, M. Photocorrosion by Oxygen Uptake in Aqueous Cadmium Sulphide Suspensions. *Ber. Bunsenges. Phys. Chem.* **1985,** *89* (2), 121-124.

(51) Arce, E.; Ibanez, J.; Meas, Y. A Kinetic Selection Criterion for Redox Couples Used to Decrease N-Type Semiconductor Photocorrosion. *C.r. Seances Acad. Sci., Ser. Ii* **1986,** *302* (10), 703-706.

(52) Meissner, D.; Memming, R.; Kastening, B.; Bahnemann, D. Fundamental Problems of Water Splitting at Cadmium Sulfide. *Chem. Phys. Lett.* **1986,** *127* (5), 419-423.

(53) Rajh, T.; Micic, O. I.; Nozik, A. J. Formation and Properties of Cu_2O Semiconductor Colloids. *Langmuir* **1986,** *2* (4), 477-480.

(54) Meissner, D.; Benndorf, C.; Memming, R. Photocorrosion of Cadmium Sulfide: Analysis by Photoelectron Spectroscopy. *Appl. Surf. Sci.* **1987,** *27* (4), 423-436.

(55) Vucemilovic, M. I.; Vukelic, N.; Rajh, T. Solubility and Photocorrosion of Small CdS Particles. *J. Photochem. Photobiol., A* **1988,** *42* (1), 157-167.

(56) Aruchamy, A.; Fujishima, A. Photoanodic Behaviour of Cu_2O Corrosion Layers on Copper Electrodes. *J. Electroanal. Chem. Interfacial Electrochem* **1989,** *272* (1-2), 125-136.

(57) Levy-Clement, C.; Tenne, R. *Photoelectrochemistry and Photovoltaics of Layered Semiconductors*. Kluwer Academic Publishers, 1992.

(58) Alexander, B. D.; Kulesza, P. J.; Rutkowska, L.; Solarska, R.; Augustynski, J. Metal Oxide Photoanodes for Solar Hydrogen Production. *J. Mater. Chem.* **2008,** *18* (20), 2298-2303.

(59) Bang, J. H.; Kamat, P. V. Quantum Dot Sensitized Solar Cells. A Tale of Two Semiconductor Nanocrystals: CdSe and CdTe. *ACS Nano* **2009,** *3* (6), 1467-1476.

(60) Jin, S. Y.; Lian, T. Q. Electron Transfer Dynamics from Single CdSe/ZnS Quantum Dots to TiO_2 Nanoparticles. *Nano Lett.* **2009,** *9* (6), 2448-2454.

(61) Mora-Sero, I.; Gimenez, S.; Fabregat-Santiago, F.; Gomez, R.; Shen, Q.; Toyoda, T.; Bisquert, J. Recombination in Quantum Dot Sensitized Solar Cells. *Acc. Chem. Res.* **2009,** *42* (11), 1848-1857.

(62) Shen, Q.; Kobayashi, J.; Diguna, L. J.; Toyoda, T. Effect of ZnS Coating on the Photovoltaic Properties of CdSe Quantum Dot-Sensitized Solar Cells. *J. Appl. Phys.* **2008,** *103* (8), Art. No. 084304.

Chapter 3 Effect of ZnS and SiO_2 Thin Layer on Stability of CdS and Charge Kinetics

3.1 Introduction

Due to relatively narrow band gap (~ 2.4 eV) and straddled conduction and valence band positions relative to water reduction and oxidation potentials, CdS has been used for solar water splitting extensively in past decades.[1–9] However, CdS will be oxidized by its photogenerated holes under illumination, and this H_2O-mediated photocorrosion will significantly deteriorate the photocatalytic performance of CdS.[10–22] One approach to improve anti-photocorrosion performance is to deposit thin layers over CdS to reduce the physical contact of CdS and electrolyte. Thin layers with thickness of few nanometers such as ZnS,[23–30] SiO_2,[31–34] Al_2O_3,[35] and graphene[36,37] etc. have been successfully applied on CdS surface, and these layers have been proved to be effective in enhancing stability as well as charge separation in CdS. However, most of the endeavors are focused on CdS quantum dots or nanoparticles, studies of impact of thin layers on CdS photoelectrodes are relatively few and systematical research on correlation of steady-state photoresponse and transient charge kinetics of CdS photoelectrode has not been published yet.

In this chapter, we report a facile strategy to improve stability and performance of CdS photocatalyst in urea-based solution by depositing a thin layer of ZnS or SiO_2 over CdS. ZnS will be prepared by successive ionic layer adsorption and reaction (SILAR) method. Sol-gel

method will be employed to prepare SiO_2 film on CdS. SiO_2 has been researched as the protective layer for Si-based photoelectrodes for water splitting reactions.[38] However, these electrodes have Si dense substrate so the conformal SiO_2 layer can easily be fabricated by atomic layer deposition (ALD) or thermal oxidation method on Si. The major challenge presented in this research lies in the deposition of non-porous and uniform SiO_2 thin layer with precise thickness control on the porous mesoscopic electrode. ALD and hydrolysis of tetraethyl orthosilicate (TEOS) (sol-gel method) are two common methods to deposit SiO_2 thin film. ALD can produce SiO_2 with precise thickness, and it has been used to fabricate mesoscopic photoelectrodes with DBL to stabilize metal oxides and produce photonic crystals. This method is based on sequential and self-limiting gas-solid reactions of precursors on the surface. Films with desired thickness can be obtained by repeating ALD reaction cycles. Compared to ALD, hydrolysis of TEOS is more cost-effective to perform. It is generally accepted that silica particles form from 3 reactions expressed as follows:[39]

$$\mathrm{Si(OC_2H_5)_4 + H_2O \xrightarrow{hydrolysis} Si(OC_2H_5)_3)OH + C_2H_5OH} \qquad \text{(Reaction 3-1)}$$

$$\mathrm{\equiv Si - OC_2H_5 + \equiv Si - OH \xrightarrow{alcohol\ condensation} \equiv Si - O - Si \equiv + C_2H_5OH} \qquad \text{(Reaction 3-2)}$$

$$\mathrm{\equiv Si - OH + \equiv Si - OH \xrightarrow{water\ condensation} \equiv Si - O - Si \equiv + H_2O} \qquad \text{(Reaction 3-3)}$$

The hydrolysis process occurs in three stages: first, hydrolysis of TEOS after mixing with water causes the formation of silanols (Reaction 3-1); second, condensation between two silanols or a silanol and an ethoxy group to from a siloxane (Si-O-Si) network (Reaction 3-2); third, formation of gel through cross-linking (Reaction 3-3). The thickness and particle size of SiO_2 can be changed by adjusting the reaction parameters such as deposition time, concentration

of precursors and reaction temperature. The sol-gel method is the preferred method to prepare the SiO_2 thin layer in this research.

CdS has been reported as a photocatalyst in urea oxidation.[40] However, the photocorrosion of the CdS photoelectrode is an issue limiting the application of CdS. In this chapter, steady-state photoresponse of CdS-ZnS and CdS-SiO_2 photoelectrode are compared with the as-prepared CdS photoelectrode, and transient charge kinetics are also studied to correlate and explain the steady-state photoresponse results. Electrochemical impedance spectroscopy and photocorrosion Tafel measurement are employed to measure the charge transfer resistance and corrosion current, respectively. All results mutually prove to unravel the impact of ZnS and SiO_2 thin layer on CdS photoelectrode steady-state photoresponse and transient charge kinetics.

3.2 Experimental

3.2.1 Materials

Titanium tetrachloride (99.9%, ACROS), titanium oxide paste (Solaronix), cadmium sulfate (≥ 99.0%, Alfa Aesar), sodium sulfide (≥ 98.0%, Avantor), zinc acetate (USP grade, Amresco), tetraethyl orthosilicate (TEOS, ≥ 99.0%, EMD Millipore Corporation), ethanol (100%, Pharmco-AAPER), urea (99.0%, Avantor), sodium sulfate (ACS grade, Ameresco). All chemicals were used as purchased.

3.2.2 Preparation of Photoelectrodes

The method to prepare TiO_2-CdS is same as the one descried in the reference[40]. Briefly, fluorine-doped tin oxide (FTO) was cut into pieces with dimension of 6 cm × 0.8 cm (length × width) and subjected to ultrasonication in detergent solution, deionized water (DI) and ethanol for 30mins, respectively. Cleaned FTO pieces were immersed in 40 mM $TiCl_4$ solution, heated to

70 °C for 30 min and followed by annealing at 500 °C for 30 min to deposit a blocking layer. DSL 18NR-T TiO_2 paste was bladed onto a 0.8 cm^2 active area, dried at 80 °C for 1 h and then annealed at 500 °C for 1 h. A post-$TiCl_4$ solution treatment (same as to deposit blocking layer) was introduced to increase the roughness of surface. CdS deposition on TiO_2 were realized via SILAR by dipping TiO_2 electrodes alternatively in $CdSO_4$ (0.1 M) and Na_2S (0.1 M) aqueous solution for ten cycles (1 min dipping and 30 s rinsing with DI water). ZnS film was prepared via SILAR by dipping TiO_2-CdS alternatively in $Zn(Ac)_2$ (0.1 M) and Na_2S (0.1 M) aqueous solution for 6 and 12 cycles (1 min dipping and 30 s rinsing with DI water), respectively. CdS-SiO_2 was prepared by dipping TiO_2-CdS electrode in 10 mM tetraethyl orthosilicate (TEOS) ethanol solution containing 100 mM NH_4OH for 24h, then the electrode was rinsed with water and dried at 70 °C in air. The second layer of SiO_2 was deposited by drop-casting at 70 °C on hotplate.

3.2.3 Materials Characterization

Morphology and composition analysis were carried out by employing a JEOS JSM-7000F scanning electron microscope (SEM) equipped with energy dispersive X-ray spectroscopy (EDS).

3.2.4 Electrochemical and PEC Measurements

Electrochemical and photoelectrochemical measurements were carried out using a Gamry Interface 1000 potentiostat in a three-electrode configuration. The active area of the photoanode for electrochemical and photoelectrochemical measurement is 0.8 cm^2 and 0.2 cm^2, respectively. A 150 W Xe lamp with an AM 1.5G filter was used to irradiate cells at 100 mW/cm^2. Linear sweep voltammetry measurements were recorded by sweeping potential at 50 mV/s. Electrochemical impedance spectroscopy was conducted in frequency range of 0.1Hz to 100 kHz

at bias of 2 V vs. Ag/AgCl under illumination. Tafel scan was carried out from – 0.25 V vs. EOC to 0.25 V vs. EOC under illumination. All electrochemical and photoelectrochemical measurements were conducted in de-aired electrolyte.

3.2.5 Optical Measurements

UV - visible absorption spectra of photoelectrodes were recorded by an Agilent Cary 60 spectrophotometer. Transient absorption (TA) measurements were recorded using a Clark MXR CPA-2010 (fundamental wavelength 775 nm, pulse duration 150 fs, pulse energy 1 mJ, repetition rate 1 kHz) incorporating Helios software provided by Ultrafast Systems. The fundamental laser output was split into a pump light and a probe light, which account for 95% and 5%, respectively. The probe light beam passed through an optical delay stage and then was focused on a Ti: sapphire crystal to provide a white light continuum. The pump light beam was directed through a second harmonic frequency doubler to produce the 387 nm pump light beam. All samples investigated were placed in a quartz cell. Based on the designed experiment, the quartz cell was pumped vacuum or filled with degassed solution.

3.3 Results and Discussions

3.3.1 EDS results

Energy dispersive spectroscopy (EDS) analysis confirms the presence of ZnS and SiO_2 on CdS photoelectrode (Figure 3-1A and Figure 3-1B). The content of elements is listed in table 3-1 and table 3-2.

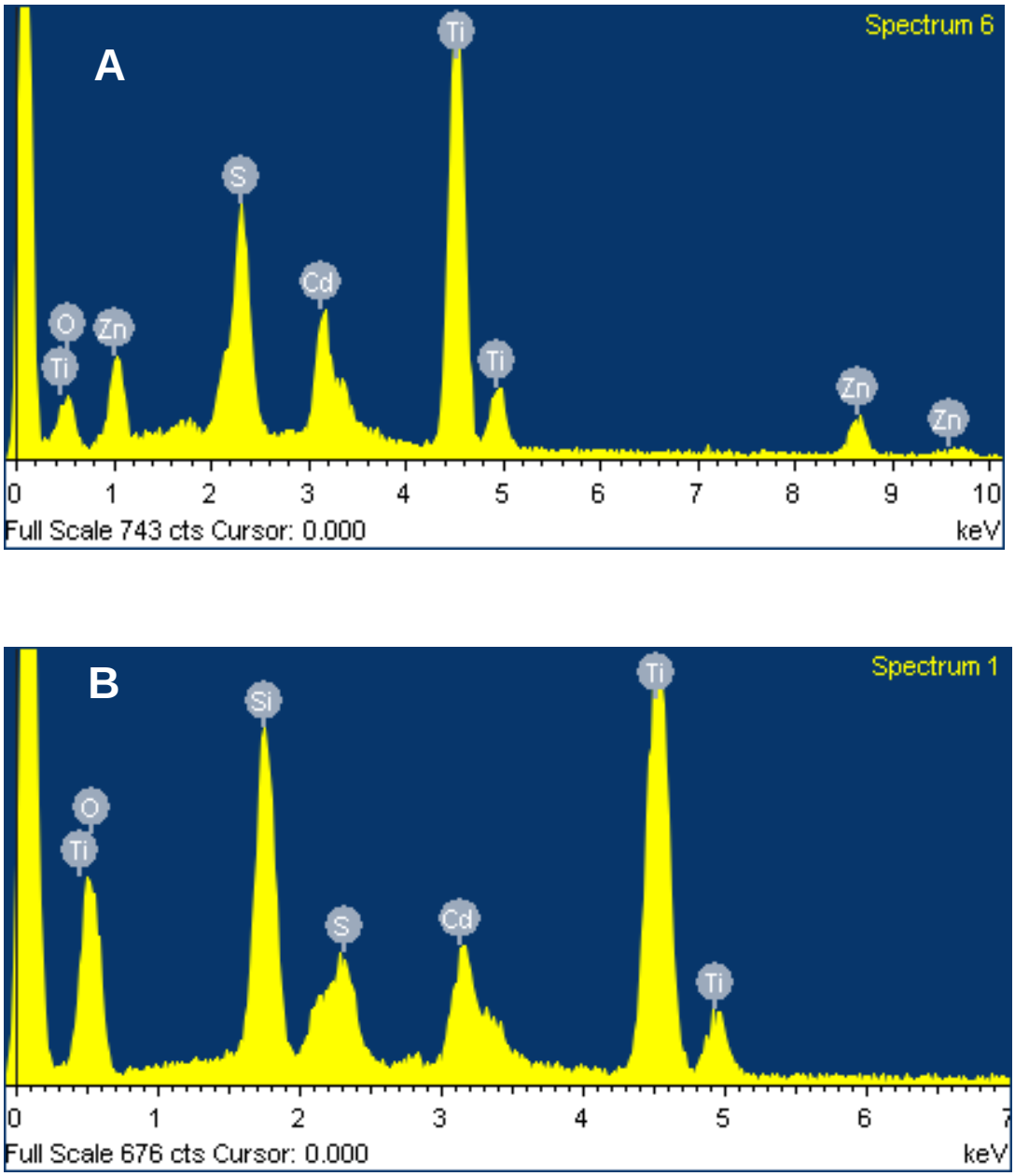

Figure 3-1. EDS results of (A) CdS-ZnS-12 and (B) CdS-SiO_2-2.

Table 3-1 Content of elements in CdS-SiO_2-2

Element	Weight%	Atomic%
O K	51.89	75.67
Si K	10.11	8.40
S K	1.98	1.44
Ti K	25.08	12.22
Cd L	10.93	2.27
Totals	100.00	

Table 3-2 Content of elements in CdS-ZnS-12

Element	Weight%	Atomic%
O K	27.30	56.15
S K	7.59	7.79
Ti K	37.17	25.54
Zn K	11.12	5.60
Cd L	16.82	4.93
Totals	100.00	

3.3.2 ZnS and SiO_2 Mapping

Element mapping images show that CdS films are not completely covered by ZnS (Figure 3-2A and 3-2B) and SiO_2 (Figure 3-2C and Figure 3-2D) due to porous structure of substrate, which means that ZnS and SiO_2 can't completely prevent physical contact of CdS and electrolyte and hence they can only partially reduce the photocorrosion of CdS.

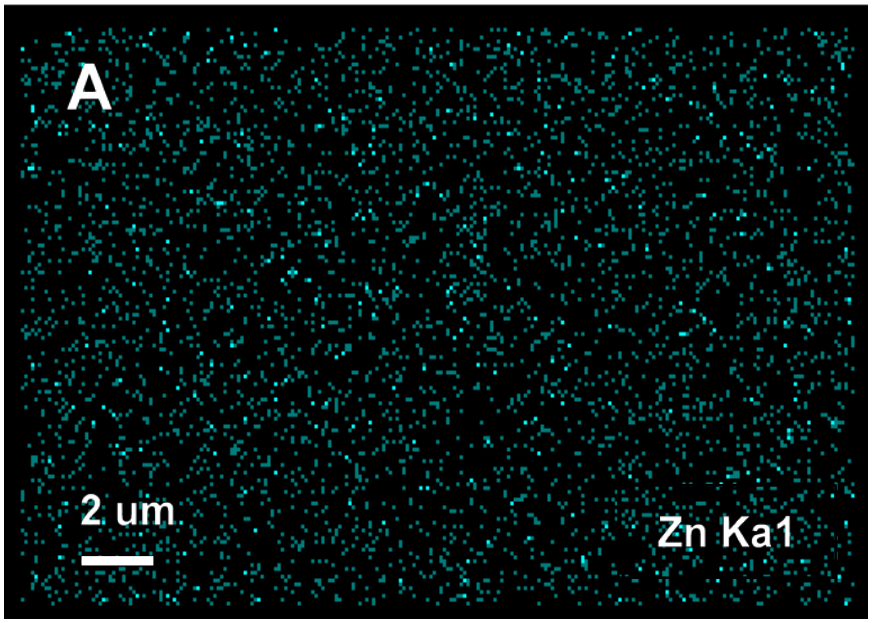

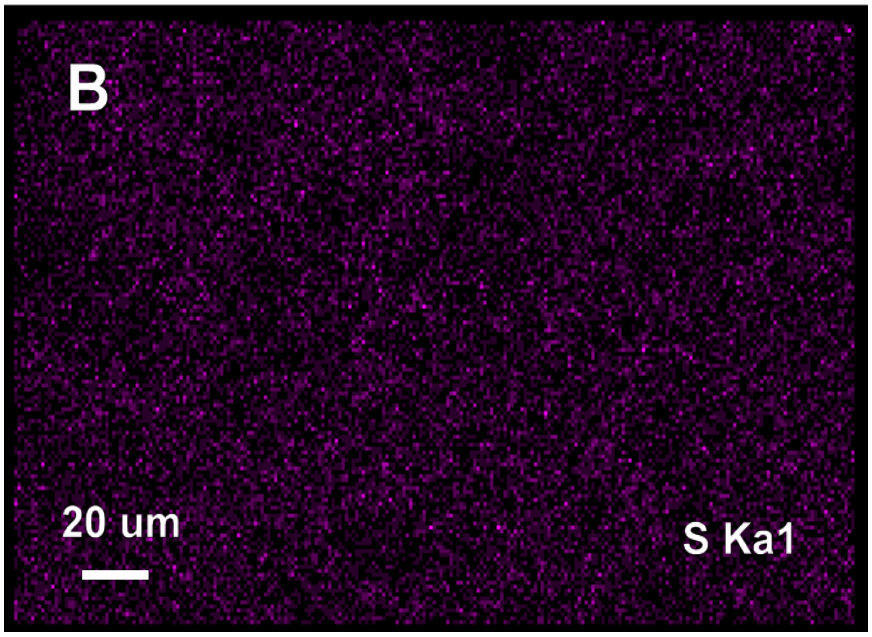
B
20 um
S Ka1

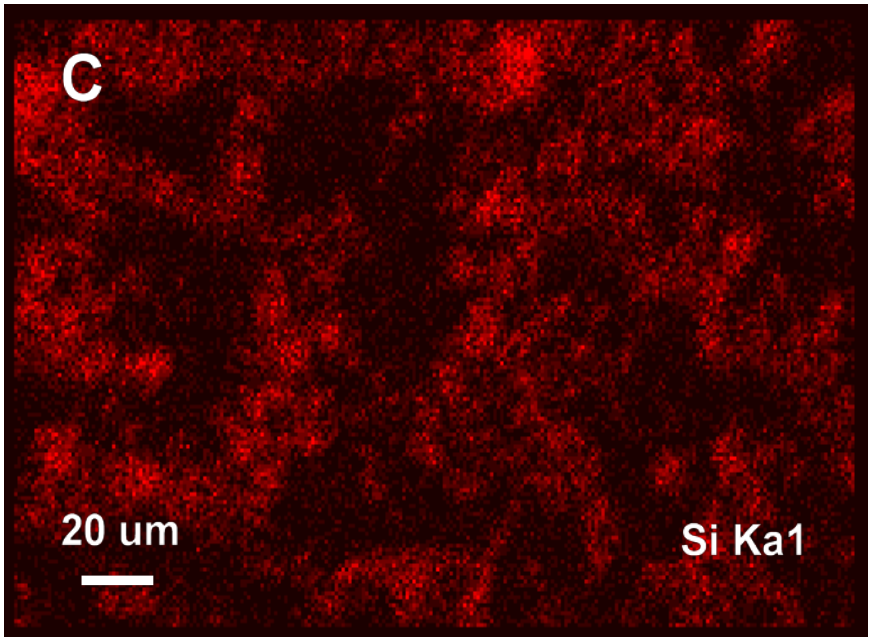
C
20 um
Si Ka1

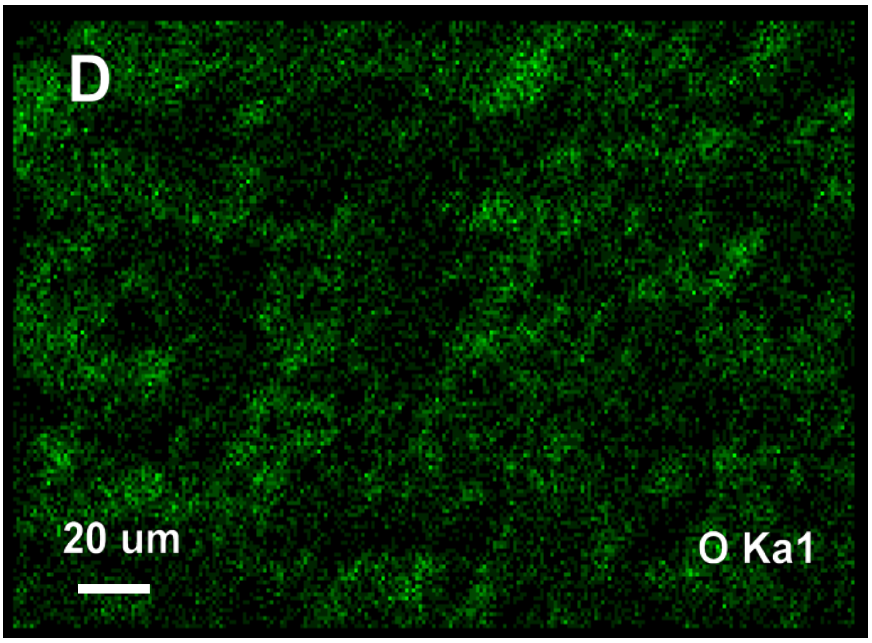

Figure 3-2. Element mapping images of (A) Zn, (B) S, (C) Si and (D) O on electrodes.

3.3.3 Optical Properties

A comparison of the UV-vis spectra of CdS, CdS-ZnS and CdS-SiO_2 electrodes are shown in Figure 3-3A and Figure 3-3B, respectively. The Figures show that ZnS or SiO_2 layer doesn't change the CdS absorption onset, which is at about 525 nm, indicating that ZnS and SiO_2 are non-photoactive in experiment. For CdS-ZnS, absorbance changes slightly with increased thickness of ZnS, and electrodes with 6 and 12 cycles of ZnS almost have the same absorbance. For CdS-SiO_2, absorbance changes slightly when wavelength is shorter than 525 nm, and the relatively larger difference in absorbance in range of 525 nm - 800 nm can be attributed to light scattering of SiO_2.

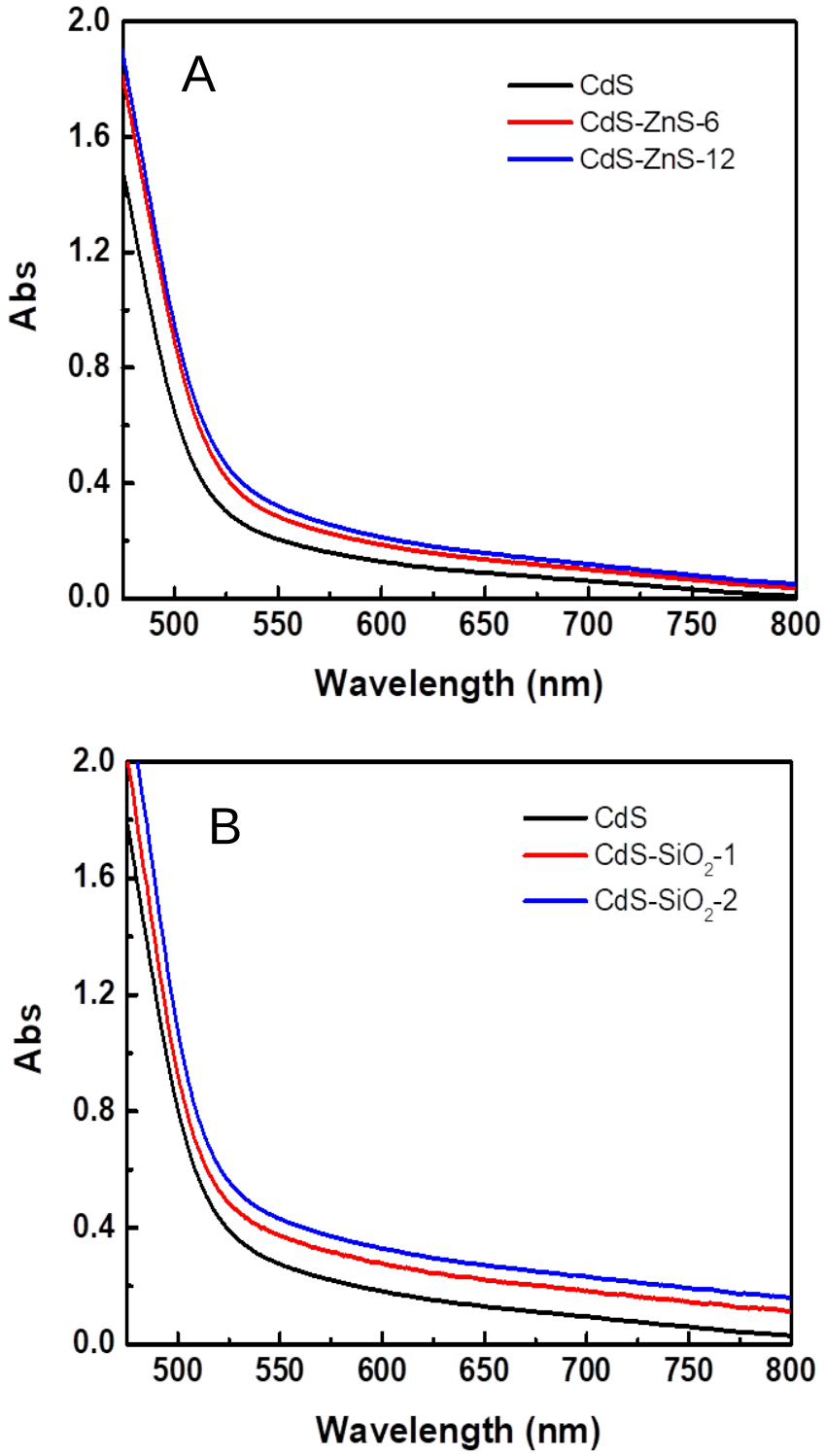

Figure 3-3. UV-Vis spectra of (A) CdS-ZnS and (B) CdS-SiO_2 electrode in vacuum.

3.3.4 Steady-state Photoresponse

I-V characteristics of the electrodes were measured using Pt wire as the counter electrode and Ag/AgCl as the reference electrode. Linear sweep voltammetry scans were conducted to reveal the state-state photoelectrochemical response at various potentials. As is shown, the open circuit potential moves negatively compared with the as-prepared CdS when ZnS is deposited on CdS (Figure 3-4A), indicating reduced recombination of photogenerated electrons and holes. As the open circuit potential is the potential difference between quasi-fermi level of electrode and redox potential of electrolyte, when the recombination of electrons and holes are reduced, more electrons will elevate to conduction band, moving quasi-fermi level toward direction of higher electron energy and hence increase the open circuit potential. The suppressed trap state-mediated non-radiative recombination is due to reduced trap states on CdS surface by surface passivation of ZnS to CdS.[23] As is shown in Figure 3-3A, more ZnS (12 cycles) yields more negative open circuit potential as more surface stated are passivated, and open circuit potential moves 300 mV negatively compared with bare CdS. I-t curves show consistent results with I-V characteristics. Enhancement of photocurrent with ZnS is due to surface passivation (Figure 3-4B). The stability of photoelectrodes also is enhanced with increased amount of ZnS deposited on CdS. As 12 cycles of ZnS cover more surface area of CdS and reduce the physical contact of CdS and electrolyte, the photocurrent is more stable due to reduced photocorrosion. Figure 3-4C shows the photocurrent stability of photoelectrodes, the photocurrent stability index Φ of CdS is 0.3 and 0.2 after illumination for 500 s and 600 s, respectively, while the numbers of CdS-ZnS-12 are 0.84 and 0.8. With a slower decay rate, photocurrent stability of ZnS-12 also decreases with time due to incomplete surface coverage of CdS by ZnS. SiO_2 can also passivate CdS surface as is shown in Figure 3-4D, the open circuit potential moves 80 mV negatively when

passivated by 2 layers of SiO_2. The stability of electrodes is enhanced with the increased amount of SiO_2 (Figure 3-4E), and the photocurrent stability index Φ for CdS is 0.24 and 0.19 after illumination for 500 s and 600 s, respectively, while the numbers for CdS-SiO_2-2 are 0.87 and 0.62 (Figure 3-4F). The decreased photocurrent stability with illumination time for CdS-SiO_2 is due to partially coverage of SiO_2 on CdS and departure of SiO_2, exposing CdS to electrolyte gradually.

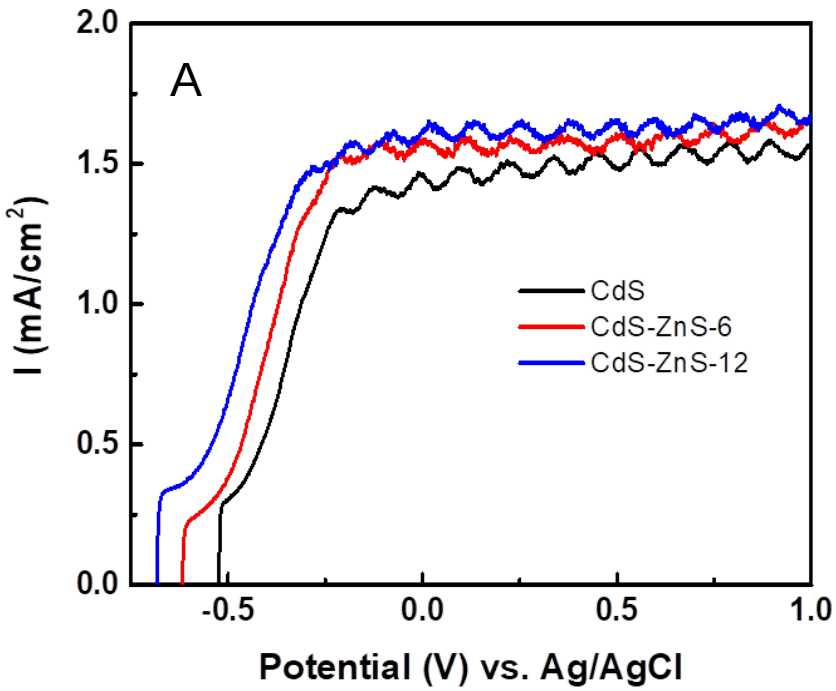

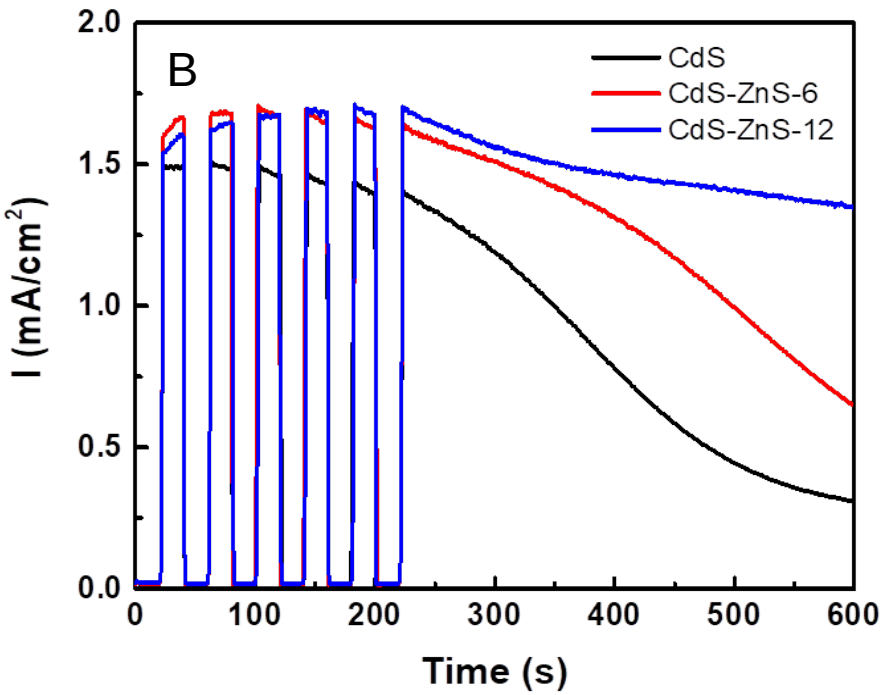
B
CdS
CdS-ZnS-6
CdS-ZnS-12
I (mA/cm^2)
Time (s)
0.0
0.5
1.0
1.5
2.0
0
100
200
300
400
500
600

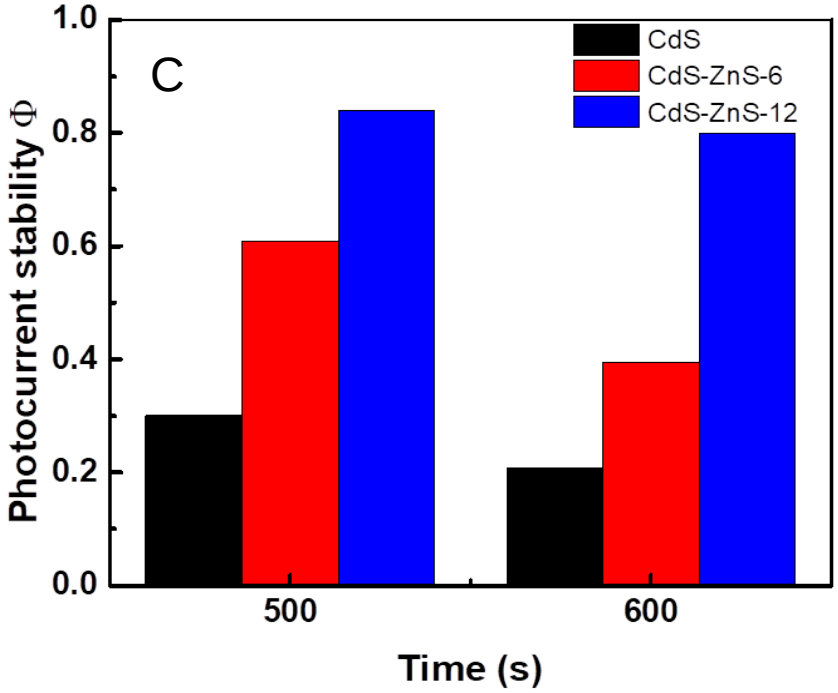
C
CdS
CdS-ZnS-6
CdS-ZnS-12
Photocurrent stability Φ
Time (s)
0.0
0.2
0.4
0.6
0.8
1.0
500
600

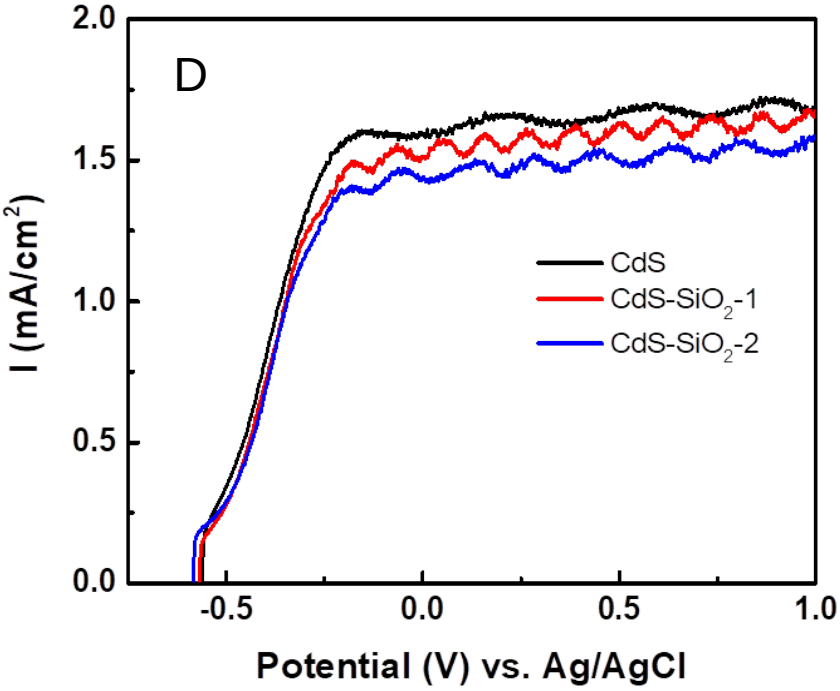
D
CdS
CdS-SiO2-1
CdS-SiO2-2
I (mA/cm2)
Potential (V) vs. Ag/AgCl
2.0
1.5
1.0
0.5
0.0
-0.5
0.0
0.5
1.0

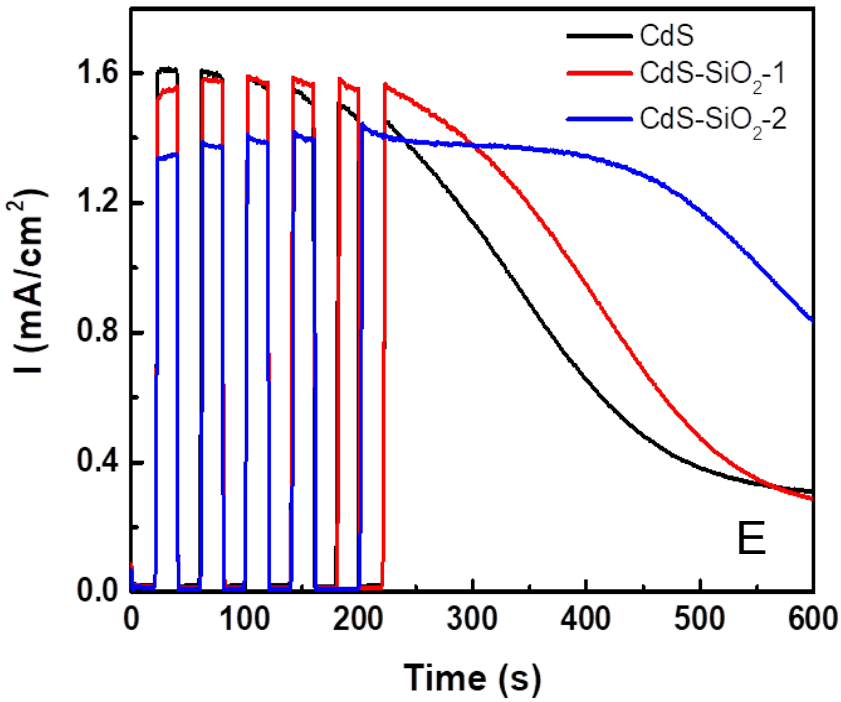
CdS
CdS-SiO2-1
CdS-SiO2-2
E
I (mA/cm2)
Time (s)
1.6
1.2
0.8
0.4
0.0
0
100
200
300
400
500
600

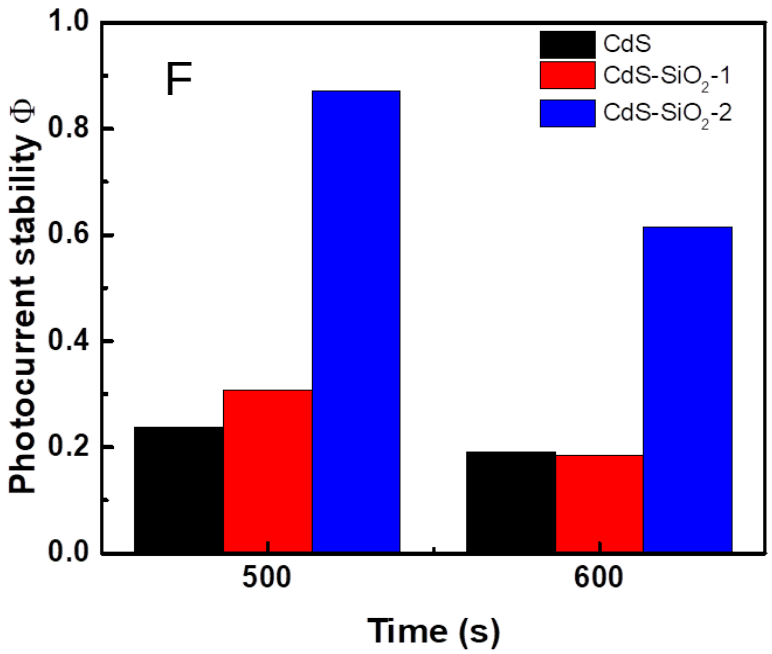

Figure 3-4. Linear sweep voltammetry, chronoamperometry and photocurrent decay of CdS-ZnS (A, B, C) and CdS-SiO_2 (D, E, F) photoanodes. In Figure C and F, Φ is obtained by dividing photocurrent by the highest photocurrent of each electrode. Φ =1 implies completely stable electrode, that is, the higher value the Φ, the better the stability of electrode. Experiments are conducted in a 3-electrode configuration with 1 M Na_2SO_4 + 0.33 M urea as electrolyte solutions under illumination using AM 1.5 simulated sunlight at 100 mW/cm^2.

3.3.5 Transient Charge Kinetics

Ultrafast transient absorption spectroscopy (TAS) was employed to probe the evolution and decay of the excited state of the CdS, CdS-ZnS and CdS-SiO_2 photoanodes. Several pathways exist for electrons and holes to transfer and recombine in the CdS-ZnS and CdS-SiO_2 photoelectrodes when immersed in urea-based electrolytes. Scheme 3-1 depicts physical processes of electrons and holes after photoexcitation of CdS upon illumination. Green arrows denote the desirable charge transfer processes, whereas red arrows indicate undesired processes. Efforts are focused on pathways 3 and 4, which reveal the impact of ZnS or SiO_2 thin layer on passivation of surface states. The decay kinetics of the transient bleach and/or absorption can be fitted using linear combination of multiexponential components according to equation 3-1:

$$y = \sum_i A_i e^{-t/\tau_i} \qquad (3\text{-}1)$$

where A_i and τ_i are amplitude and time constant of the ith component, respectively. The average time constant and corresponding rate constant for bleach and absorption decay related to electron and hole transfer and recombination can then be obtained using equations (3-2) and (3-3).

$$\tau_{ave} = \frac{\sum A_i \tau_i^2}{\sum A_i \tau_i} \qquad (3\text{-}2)$$

$$k = \frac{1}{\tau_{ave}} \qquad (3\text{-}3)$$

Path number	Rate constant	Physical process
1	k_{et}	Electron transfer from CdS to TiO_2
2	$k_{bt\text{-}1}$	Back electron transfer from TiO_2 to CdS
3	$k_{trap\text{-}h}$	Hole trapped by surface states
4	$k_{trap\text{-}e}$	Electron trapped by surface states
5	k_{ht}	Hole transfer from CdS to electrolyte

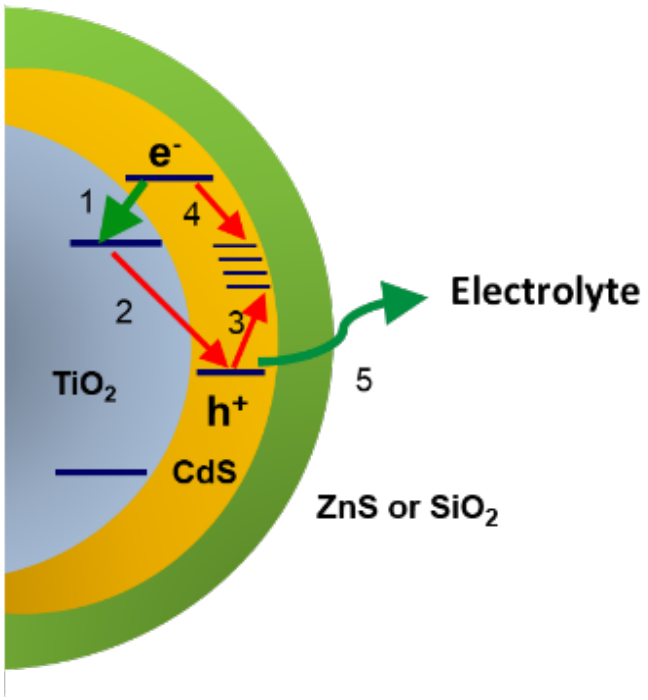

Scheme 3-1. Schematic representation of the dynamical processes upon photon absorption of CdS electrode architecture with ZnS or SiO_2. The table outlines the physical processes after photoexcitation upon illumination.

3.3.6 Surface Passivation

To study the impact of ZnS and SiO_2 on passivation of surface states of CdS, the decay rates of the transient bleach of CdS, CdS-ZnS and CdS-SiO_2 are probed in vacuum. As the bleach decay relates to depopulation of electrons from the conduction band of CdS, which in vacuum is due to the electron transfer from CdS to TiO_2 (pathway 1 in scheme 3-1) and electron trapping by surface trap states of CdS (pathway 4 in scheme 3-1), comparison of beach decay kinetics of CdS, CdS-ZnS and CdS-SiO_2 can obtain the electron trapping information and hence the surface passivation effect of ZnS and SiO_2 on CdS since electron transfer from CdS to TiO_2 is supposed to be the same for all electrodes. As is shown in Figure 3-5, the bleaches decay (tri-

exponentially fitted by using equation 3-1) slower when there exists ZnS or SiO_2 thin layer on CdS compared to bare CdS, indicating less electron trapping due to reduced surface trap states by passivation of ZnS or SiO_2, which is consistent with the results obtained in linear sweep voltammetry. Table 3-3 gives beach decay time and rate constant for different electrodes calculated by using equations (3-2) and (3-3). Compared to 6 cycles of ZnS, the bleach decays slower for 12 cycles of ZnS due to less surface trap states, which decreases the trap-mediated recombination. However, the difference in decay time is not significant, revealing that 6 cycles of ZnS passivate most surface trap states on CdS. SiO_2-passivated CdS also shows that there is almost no difference in decay time for electrodes with 1 layer and 2 layers of SiO_2, and the abnormal shorter decay time of electrode with 2 layers SiO_2 compared to 1 layer SiO_2 could be attributed to the unavoidable experiment error, considering the time difference is only around 13 s.

Table 3-3. Bleach decay time and rate constant related electron trapping in surface trap states

Bleach decay time (ps)	**Bleach decay rate constant (s^{-1})**	**System**
417.5	2.40×10^9	CdS
491.8	2.03×10^9	CdS-ZnS-6
519.9	1.92×10^9	CdS-ZnS-12
561.4	1.78×10^9	CdS-SiO_2-1
548.2	1.82×10^9	CdS-SiO_2-2

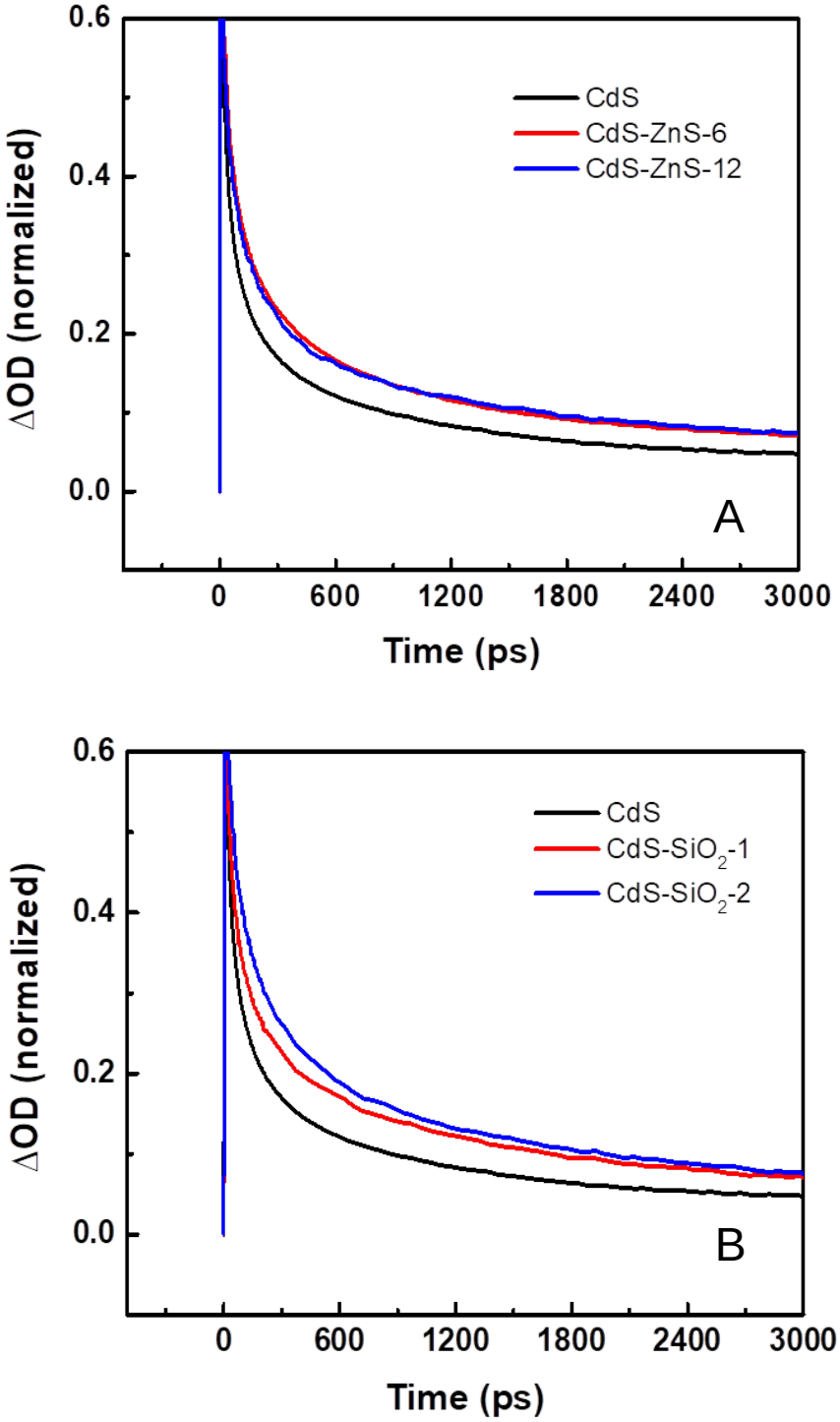

Figure 3-5. Transient bleach decay kinetics of (A) CdS and CdS-ZnS with different cycles of CdS and (B) CdS and CdS-SiO_2 with different cycles of SiO_2 in vacuum.

3.3.7 Hole Kinetics

To measure the effect of thin film ZnS or SiO_2 on hole kinetics, 6 layers of ZnS or 1 layer of SiO_2 are deposited on CdS. The transient absorption decay of CdS, CdS-ZnS and CdS-SiO_2 is shown in Figure 3-6. As is shown, the absorption decay related to holes shows the same decay tendency as transient bleach decay, that is, the absorption decays slower when there is ZnS or SiO_2 on CdS. The decay of transient absorption is due to the recombination of holes and electrons, and as less holes are trapped in surface trap states when ZnS or SiO_2 present on CdS, the trap-mediated recombination is reduced, showing the slower transient absorption decay.

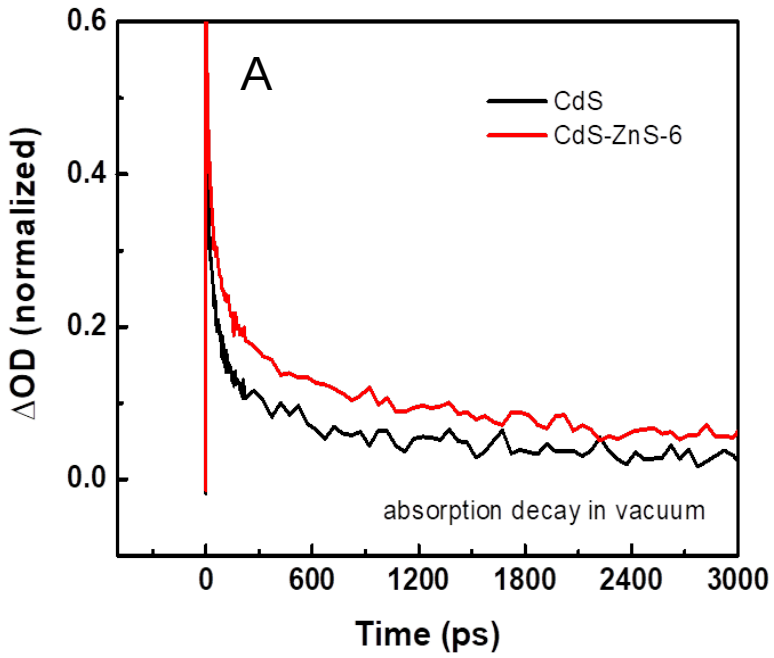

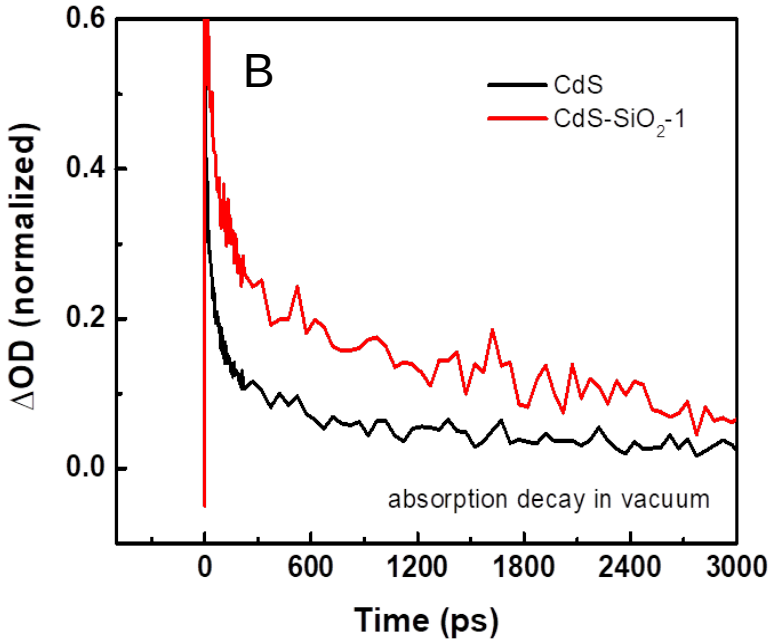

Figure 3-6. Absorption decay kinetics of CdS, CdS-ZnS-6 and CdS-SiO_2-1 in vacuum.

3.3.8 Charge Transfer Resistance

Electrochemical impedance spectroscopy (EIS) was employed to study the interfacial charge transfer impedance in CdS, CdS-ZnS and CdS-SiO_2 in electrolyte under illumination. As the diameter of semicircle represents the charge transfer impedance,[41–43] the impedance for CdS, CdS-ZnS with 12 cycles of ZnS and CdS-SiO_2 with 2 cycles of SiO_2 is 200 Ω, 250 Ω and 275 Ω, respectively (Figure 3-7). The results show that ZnS or SiO_2 exists as potential barrier to suppress charge transfer, which is consistent with the result obtained in transient absorption spectroscopy.

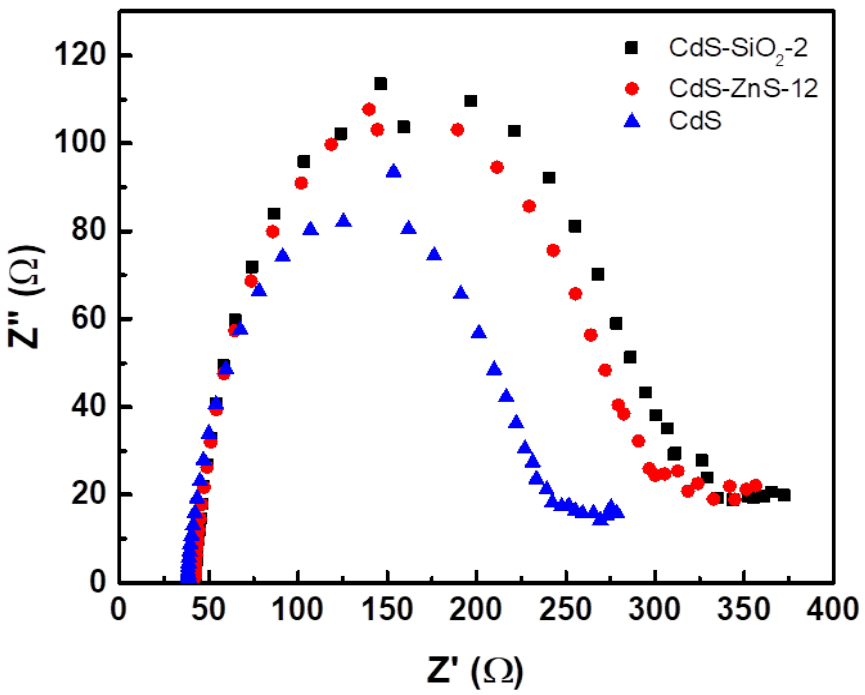

Figure 3-7. Electrochemical impedance spectra of CdS, CdS-ZnS-12 and CdS-SiO_2-2 in 1M Na_2SO_4 + 0.33 M urea. Scans were conducted in range from 0.1Hz to 100 kHz under external potential of 2V vs. Ag/AgCl at potentiostatic mode under illumination.

3.3.9 Tafel Measurement

Tafel scan is used to study the corrosion of electrodes.[44] It is performed by extrapolating the linear portions of a logarithmic current versus potential plot back to their intersection. The value of either the anodic or the cathodic current at the intersection is corrosion current. The plots of E vs. log I of different electrodes in Na_2SO_4 and Na_2SO_4-urea solution are shown in Figure 3-8. Photocorrosion current is listed in table 3-4, as is shown, the photocorrosion current density for CdS, CdS-ZnS and CdS-SiO_2 in Na_2SO_4 is 204 μA/cm^2, 92 μA/cm^2 and 76 μA/cm^2, respectively. The photocorrosion current decreased 55% for ZnS-coated CdS and 63% for SiO_2-coated CdS, indicating that the ZnS or SiO_2 reduced the physical contact of CdS and electrolyte, decreased H_2O-mediated photocorrosion and increased stability of photoelectrodes, which is consistent with the results obtained in Figure 3-3. The photocorrosion was also measured in

Na_2SO_4-urea solution. As is shown in table 3-4, the photocorrosion current is lower than those in Na_2SO_4. The photocorrosion current decreased 25%, 28% and 33% for CdS, CdS-ZnS and CdS-SiO_2 in urea-containing electrolyte, respectively, showing that urea can accept holes and passivate the surface dangling bands, reduce the holes trapped by S^{2-} and decrease the photocorrosion.

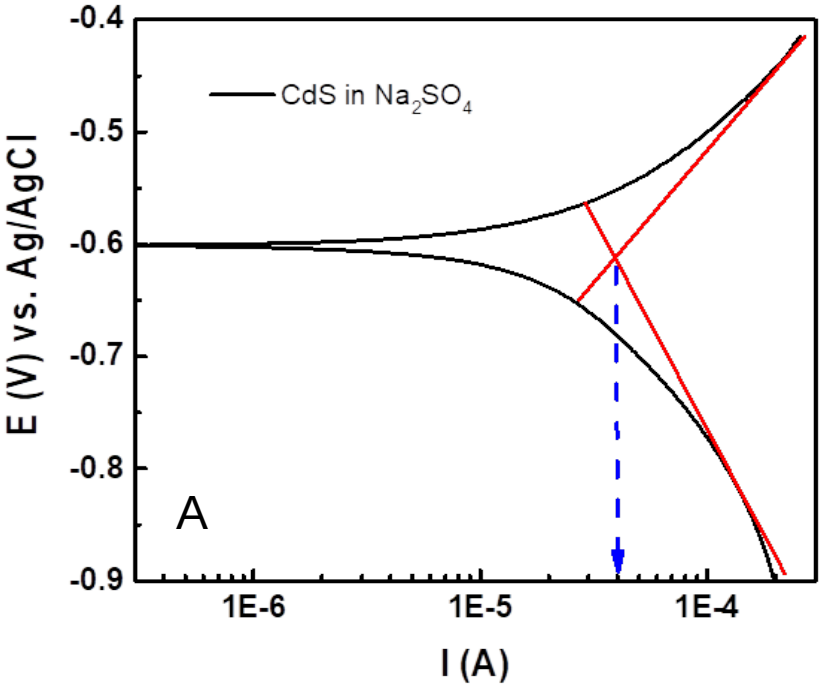

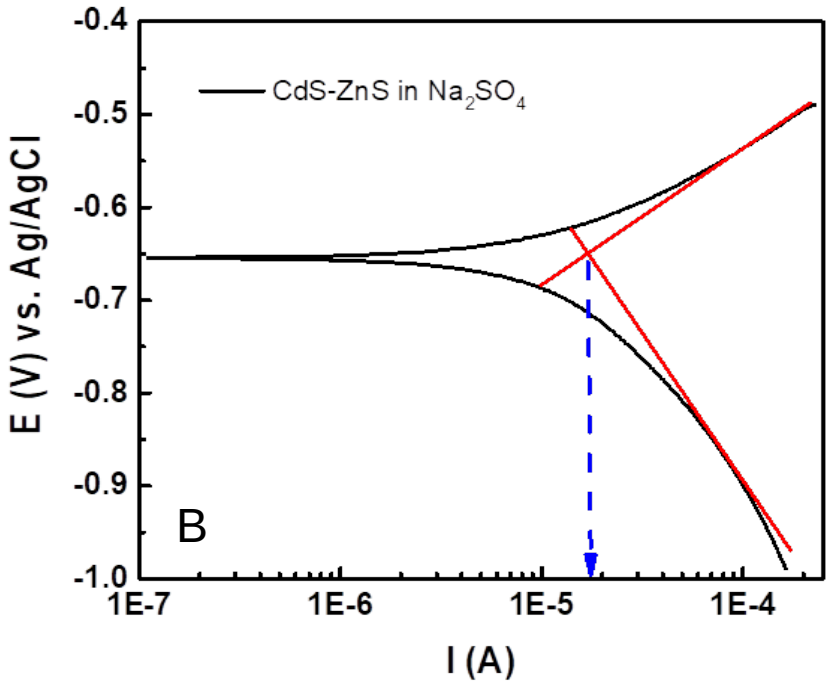
CdS-ZnS in Na_2SO_4
E (V) vs. Ag/AgCl
I (A)
B
-0.4
-0.5
-0.6
-0.7
-0.8
-0.9
-1.0
1E-7
1E-6
1E-5
1E-4

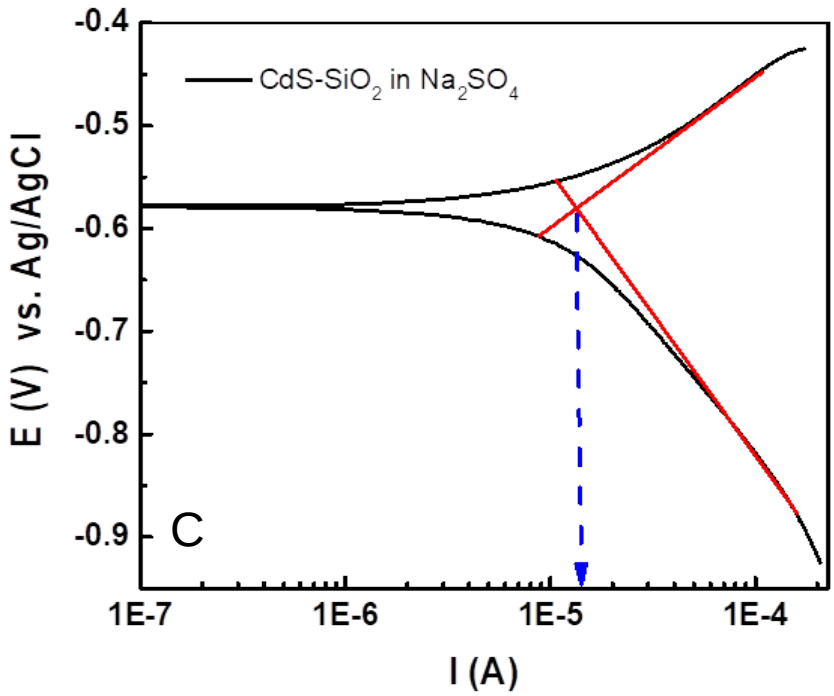
CdS-SiO_2 in Na_2SO_4
E (V) vs. Ag/AgCl
I (A)
C
-0.4
-0.5
-0.6
-0.7
-0.8
-0.9
1E-7
1E-6
1E-5
1E-4

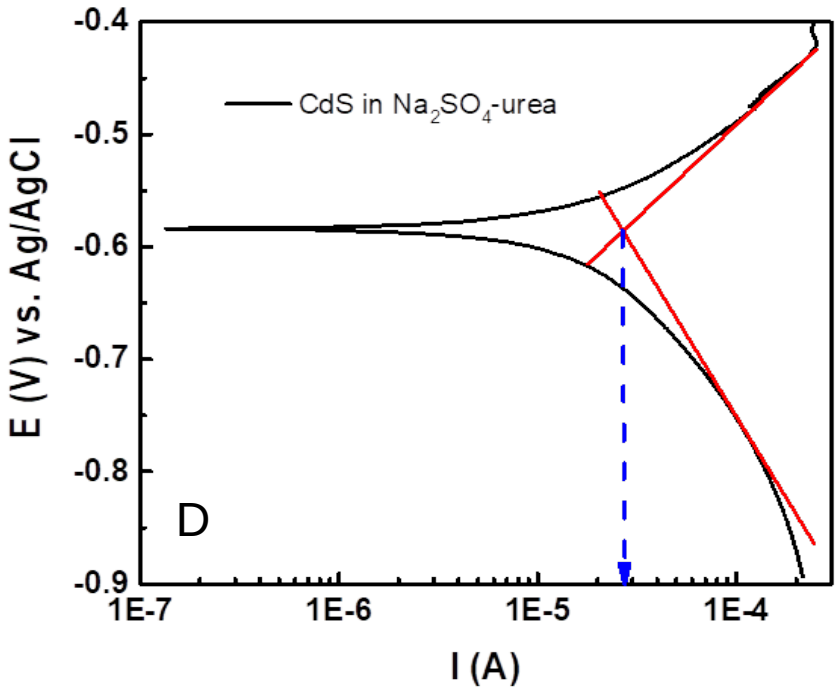
CdS in Na_2SO_4-urea
D
E (V) vs. Ag/AgCl
I (A)
-0.4
-0.5
-0.6
-0.7
-0.8
-0.9
1E-7
1E-6
1E-5
1E-4

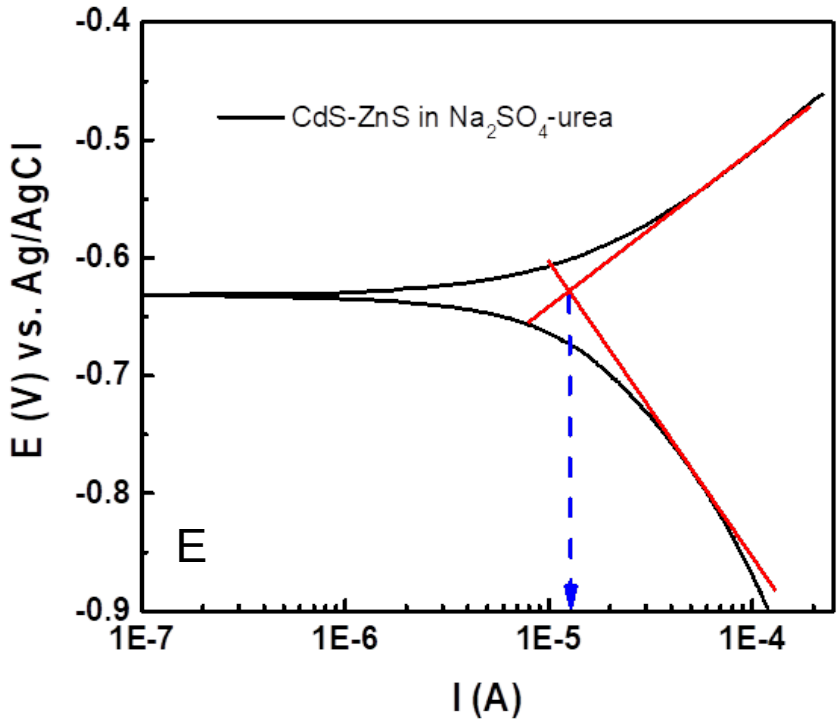
CdS-ZnS in Na_2SO_4-urea
E
E (V) vs. Ag/AgCl
I (A)
-0.4
-0.5
-0.6
-0.7
-0.8
-0.9
1E-7
1E-6
1E-5
1E-4

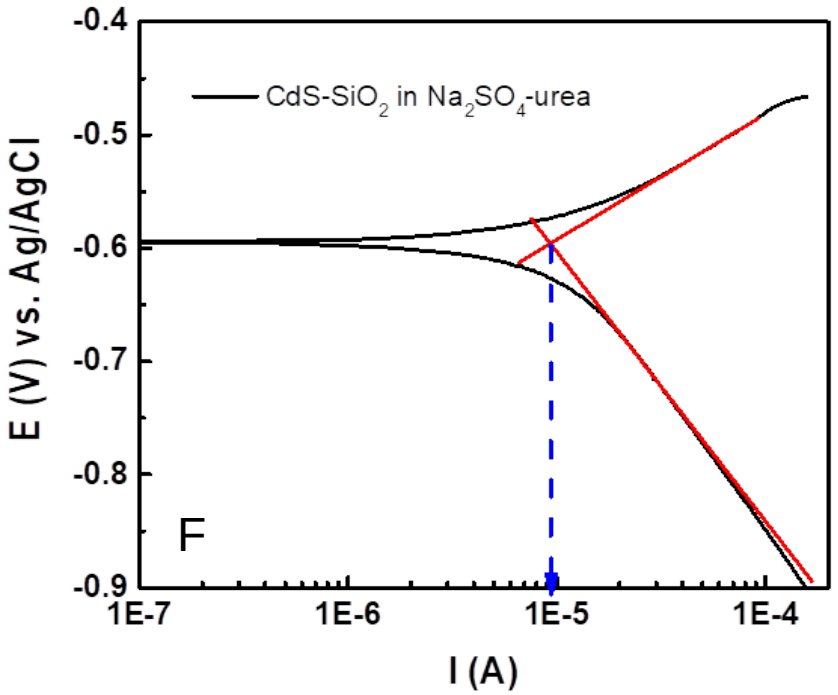

Figure 3-8. Photocorrosion current of (A) CdS (B) CdS-ZnS-12 (C) CdS-SiO_2-2 in 1 M Na_2SO_4 and (D) CdS (E) CdS-ZnS-12 (F) CdS-SiO_2-2 in 1 M Na_2SO_4 + 0.33 M urea.

Table 3-4. Photocorrosion current of electrodes in Na_2SO_4 and Na_2SO_4-urea

Na_2SO_4 ($\mu A/cm^2$)	Na_2SO_4-urea ($\mu A/cm^2$)	System
204	153	CdS
92	66	CdS-ZnS
76	51	CdS-SiO_2

3.4 Summary

Photocorrsion of semiconductor-based photoelectrodes is an issue limiting the application of some semiconductors, while important, studies on enhancement of stability of semiconductor photoelectrodes are relatively few. Thin dielectric layers have been proposed to reduce photocorrosion and improve performance of photoelectrodes, yet systematical research on

correlation of steady-state photoresponse and transient charge kinetics of photoelectrodes has not been published. This chapter took CdS as an example semiconductor to study the impact of thin dielectric layer ZnS and SiO_2 on its photostability and performance. Transient absorption technique was also employed to exposit the mechanism behind steady-state photoresponse. ZnS and SiO_2 were deposited on TiO_2-CdS photoelectrode by successive ionic layer absorption and reaction (SILAR) and sol-gel method, respectively. Stead-state photoresponse results showed that the open circuit potential moved 300 mV and 80 mV negatively when electrodes were passivated by 12 cycles of ZnS and 2 layers of SiO_2, respectively, illustrating both ZnS and SiO_2 passivated CdS surface states. Stability test results revealled that after illumination for 10 min, photocurrent stability improved 4 and 3 times compared to bare CdS for 12 cycles of ZnS and 2 layers of SiO_2, respectively. Transient absorption results showed slower bleach and absorption decay due to reduced trap-mediated recombination when ZnS or SiO_2 presents on CdS photoelectrode. Electrochemical impedance results showed a higher charge transfer resistance when there existed ZnS or SiO_2, which is consistent with the transient absorption results. Tafel plots showed that the photocorrosion current decreased 55% for ZnS-coated CdS and 63% for SiO_2-coated CdS compared to bare CdS, revealing the reduction of photocorrosion when ZnS or SiO_2 was present as the blocking layer.

References

(1) Tongying, P.; Vietmeyer, F.; Aleksiuk, D.; Ferraudi, G. J.; Krylova, G.; Kuno, M. Double Heterojunction Nanowire Photocatalysts for Hydrogen Generation. *Nanoscale* **2014**, *6* (8), 4117–4124.

(2) Wang, G.; Yang, X.; Qian, F.; Zhang, J. Z.; Li, Y. Double-Sided CdS and CdSe Quantum Dot Co-Sensitized ZnO Nanowire Arrays for Photoelectrochemical Hydrogen Generation. *Nano Lett.* **2010**, *10* (3), 1088–1092.

(3) Zhukovskyi, M.; Tongying, P.; Yashan, H.; Wang, Y.; Kuno, M. Efficient Photocatalytic Hydrogen Generation from Ni Nanoparticle Decorated CdS Nanosheets. *ACS Catal.* **2015**, *5* (11), 6615–6623.

(4) Jia, L.; Wang, D. H.; Huang, Y. X.; Xu, A. W.; Yu, H. Q. Highly Durable N-Doped Graphene/CdS Nanocomposites with Enhanced Photocatalytic Hydrogen Evolution from Water under Visible Light Irradiation. *J. Phys. Chem. C* **2011**, *115* (23), 11466–11473.

(5) Li, Q.; Guo, B.; Yu, J.; Ran, J.; Zhang, B.; Yan, H.; Gong, J. R. Highly Efficient Visible-Light-Driven Photocatalytic Hydrogen Production of CdS-Cluster-Decorated Graphene Nanosheets. *J. Am. Chem. Soc.* **2011**, *133* (28), 10878–10884.

(6) Kakuta, N.; Park, K. H.; Finlayson, M. F.; Ueno, A.; Bard, A. J.; Campion, A.; Fox, M. A.; Webber, S. E.; White, J. M. Photoassisted Hydrogen Production Using Visible Light and Coprecipitated ZnS-CdS without a Noble Metal. *J. Phys. Chem.* **1985**, *89* (5), 732–734.

(7) Qiu, F.; Han, Z.; Peterson, J. J.; Odoi, M. Y.; Sowers, K. L.; Krauss, T. D. Photocatalytic Hydrogen Generation by CdSe/CdS Nanoparticles. *Nano Lett.* **2016**, *16* (9), 5347–5352.

(8) Thewissen, H.; Timmer, K.; A. van der Zouwen-Assink, E.; H. A. Tinnemans, A.; Mackor, A. Preparation of Active CdS/RuO X Particles for the Photogeneration of H_2. *J. Chem. Soc. Chem. Commun.* **1985**.

(9) Kamat, P. V. Quantum Dot Solar Cells. The Next Big Thing in Photovoltaics. *J. Phys. Chem. Lett.* **2013**, *4* (6), 908–918.

(10) Awatani, T.; McQuillan, A. J. Adsorbed Thiosulfate Intermediate of Cadmium Sulfide Aqueous Photocorrosion Detected and Characterized by in Situ Infrared Spectroscopy. *J. Phys. Chem. B* **1998**, *102* (21), 4110–4113.

(11) Manassen, J.; Cahen, D.; Hodes, G.; Sofer, A. Electrochemical, Solid State, Photochemical and Technological Aspects of Photoelectrochemical Energy Converters. *Nature* **1976**, *263* (5573), 97–100.

(12) Ferrer, I. J.; Salvador, P.; Velasco, J. G. On the Photoelectrochemical Etching of Polycrystalline CdS Thin Film Electrodes in SO_3^{2-} Electrolytes. *J. Electroanal. Chem. Interfacial Electrochem.* **1985**, *189* (2), 363–369.

(13) Gerischer, H. On the Stability of Semiconductor Electrodes against Photodecomposition. *J. Electroanal. Chem. Interfacial Electrochem.* **1977**, *82* (1), 133–143.

(14) Ellis, A. B.; Kaiser, S. W.; Wrighton, M. S. Optical to Electrical Energy Conversion. Characterization of Cadmium Sulfide and Cadmium Selenide Based Photoelectrochemical Cells. *J. Am. Chem. Soc.* **1976**, *98* (22), 6855–6866.

(15) Meissner, D.; Memming, R.; Kastening, B. Photoelectrochemistry of Cadmium Sulfide. 1. Reanalysis of Photocorrosion and Flat-Band Potential. *J. Phys. Chem.* **1988**, *92* (12), 3476–3483.

(16) Meissner, D.; Lauermann, I.; Memming, R.; Kastening, B. Photoelectrochemistry of Cadmium Sulfide. 2. Influence of Surface-State Charging. *J. Phys. Chem.* **1988**, *92* (12), 3484–3488.

(17) Dewitt, R.; Kirsch-De Mesmaeker, A. Polycrystalline CdS Photocorrosion Studied by Capacitance and Action Spectra Measurements. *Appl. Phys. Lett.* **1984**, *45* (2), 146–147.

(18) Matsumoto, H.; Sakata, T.; Mori, H.; Yoneyama, H. Preparation of Monodisperse CdS Nanocrystals by Size Selective Photocorrosion. *J. Phys. Chem.* **1996**, *100* (32), 13781–13785.

(19) Rubin, H. D.; Humphrey, B. D.; Bocarsly, A. B. Role of Surface Reactions in the Stabilization of N-CdS-Based Photoelectrochemical Cells. *Nature* **1984**, *308* (5957), 339–341.

(20) Bard, A. J.; Wrighton, M. S. Thermodynamic Potential for the Anodic Dissolution of n-Type Semiconductors A Crucial Factor Controlling Durability and Efficiency in Photoelectrochemical Cells and an Important Criterion in the Selection of New Electrode/Electrolyte Systems. *J. Electrochem. Soc.* **1977**, *124* (11), 1706–1710.

(21) Park, S. M.; Barber, M. E. Thermodynamic Stabilities of Semiconductor Electrodes. *J. Electroanal. Chem. Interfacial Electrochem.* **1979**, *99* (1), 67–75.

(22) Ellis, A. B.; Kaiser, S. W.; Wrighton, M. S. Visible Light to Electrical Energy Conversion. Stable Cadmium Sulfide and Cadmium Selenide Photoelectrodes in Aqueous Electrolytes. *J. Am. Chem. Soc.* **1976**, *98* (6), 1635–1637.

(23) Zhao, K.; Pan, Z.; Mora-Seró, I.; Cánovas, E.; Wang, H.; Song, Y.; Gong, X.; Wang, J.; Bonn, M.; Bisquert, J.; et al. Boosting Power Conversion Efficiencies of Quantum-Dot-

Sensitized Solar Cells Beyond 8% by Recombination Control. *J. Am. Chem. Soc.* **2015**, *137* (16), 5602–5609.

(24) Boldt, K.; Ramanan, C.; Chanaewa, A.; Werheid, M.; Eychmüller, A. Controlling Charge Carrier Overlap in Type-II ZnSe/ZnS/CdS Core–Barrier–Shell Quantum Dots. *J. Phys. Chem. Lett.* **2015**, *6* (13), 2590–2597.

(25) Chen, H. Y.; Maiti, S.; Son, D. H. Doping Location-Dependent Energy Transfer Dynamics in Mn-Doped CdS/ZnS Nanocrystals. *ACS Nano* **2012**, *6* (1), 583–591.

(26) Mollavali, M.; Falamaki, C.; Rohani, S. Efficient Light Harvesting by NiS/CdS/ZnS NPs Incorporated in C, N-Co-Doped-TiO_2 Nanotube Arrays as Visible-Light Sensitive Multilayer Photoanode for Solar Applications. *Int. J. Hydrog. Energy* **2018**, *43*.

(27) Wang, Y. F.; Wang, H. Y.; Li, Z. S.; Zhao, J.; Wang, L.; Chen, Q. D.; Wang, W. Q.; Sun, H. B. Electron Extraction Dynamics in CdSe and CdSe/CdS/ZnS Quantum Dots Adsorbed with Methyl Viologen. *J. Phys. Chem. C* **2014**, *118* (31), 17240–17246.

(28) Takayama, K.; Fujiwara, K.; Kume, T.; Naya, S.; Tada, H. Electron Filtering by an Intervening ZnS Thin Film in the Gold Nanoparticle-Loaded CdS Plasmonic Photocatalyst. *J. Phys. Chem. Lett.* **2017**, *8* (1), 86–90.

(29) Chen, H. Y.; Chen, T. Y.; Son, D. H. Measurement of Energy Transfer Time in Colloidal Mn-Doped Semiconductor Nanocrystals. *J. Phys. Chem. C* **2010**, *114* (10), 4418–4423.

(30) Kumar, P.; Ray, R.; Adel, P.; Luebkemann, F.; Dorfs, D.; Pal, S. K. Role of ZnS Segment on Charge Carrier Dynamics and Photoluminescence Property of CdSe@CdS/ZnS Quantum Rods. *J. Phys. Chem. C* **2018**, *122* (11), 6379–6387.

(31) Mao, L. H.; Zhang, Q. H.; Zhang, Y.; Wang, C. F.; Chen, S. Construction of Highly Luminescent CdTe/CdS@ZnS–SiO_2 Quantum Dots as Conversion Materials toward

Excellent Color-Rendering White-Light-Emitting Diodes. *Ind. Eng. Chem. Res.* **2014**, *53* (43), 16763–16770.

(32) Gupta, N.; Pal, B. Core–shell Structure of Metal Loaded CdS–SiO_2 Hybrid Nanocomposites for Complete Photomineralization of Methyl Orange by Visible Light. *J. Mol. Catal. Chem.* **2014**, *391*, 158–167.

(33) Liu, Z.; Miyauchi, M.; Uemura, Y.; Cui, Y.; Hara, K.; Zhao, Z.; Sunahara, K.; Furube, A. Enhancing the Performance of Quantum Dots Sensitized Solar Cell by SiO_2 Surface Coating. *Appl. Phys. Lett.* **2010**, *96* (23), 233107.

(34) Anderson, B. D.; Wu, W.-C.; Tracy, J. B. Silica Overcoating of CdSe/CdS Core/Shell Quantum Dot Nanorods with Controlled Morphologies. *Chem. Mater.* **2016**, *28* (14), 4945–4952.

(35) Roelofs, K. E.; Brennan, T. P.; Dominguez, J. C.; Bailie, C. D.; Margulis, G. Y.; Hoke, E. T.; McGehee, M. D.; Bent, S. F. Effect of Al_2O_3 Recombination Barrier Layers Deposited by Atomic Layer Deposition in Solid-State CdS Quantum Dot-Sensitized Solar Cells. *J. Phys. Chem. C* **2013**, *117* (11), 5584–5592.

(36) Cho, K. M.; Kim, K. H.; Park, K.; Kim, C.; Kim, S.; Al-Saggaf, A.; Gereige, I.; Jung, H.-T. Amine-Functionalized Graphene/CdS Composite for Photocatalytic Reduction of CO_2. *ACS Catal.* **2017**, *7* (10), 7064–7069.

(37) Wang, M.; Cai, L.; Wang, Y.; Zhou, F.; Xu, K.; Tao, X.; Chai, Y. Graphene-Draped Semiconductors for Enhanced Photocorrosion Resistance and Photocatalytic Properties. *J. Am. Chem. Soc.* **2017**, *139* (11), 4144–4151.

(38) Esposito, D. V.; Levin, I.; Moffat, T. P.; Talin, A. A. H_2 Evolution at Si-Based Metal–insulator–semiconductor Photoelectrodes Enhanced by Inversion Channel Charge Collection and H Spillover. *Nat. Mater.* **2013**, *12*, 562.

(39) Buckley, A. M.; Greenblatt, M. The Sol-Gel Preparation of Silica Gels. *J. Chem. Educ.* **1994**, *71* (7), 599.

(40) Zhao, R.; Schumacher, G.; Leahy, S.; Radich, J. G. $Ni(OH)_2$ as Hole Mediator for Visible Light-Induced Urea Splitting. *J. Phys. Chem. C* **2018**, *122* (25), 13995−14003.

(41) Hu, W.; Liu, T.; Guo, Y.; Luo, S.; Shen, H.; He, H.; Wang, N.; Lin, H. Highly Efficient Solid-State Solar Cells Based on Composite CdS-ZnS Quantum Dots. *J. Electrochem. Soc.* **2015**, *162* (10), H747–H752.

(42) Leng, W. H.; Zhang, Z.; Zhang, J. Q.; Cao, C. N. Investigation of the Kinetics of a TiO_2 Photoelectrocatalytic Reaction Involving Charge Transfer and Recombination through Surface States by Electrochemical Impedance Spectroscopy. *J. Phys. Chem. B* **2005**, *109* (31), 15008–15023.

(43) Jun, H. K.; Careem, M. A.; Arof, A. K. Performances of Some Low-Cost Counter Electrode Materials in CdS and CdSe Quantum Dot-Sensitized Solar Cells. *Nanoscale Res. Lett.* **2014**, *9* (1), 69.

(44) Allongue, P.; Blonkowski, S. Corrosion of III-V Compounds; a Comparative Study of GaAs and InP: Part I. Electrochemical Characterization Based on Tafel Plot Measurements. *J. Electroanal. Chem. Interfacial Electrochem.* **1991**, *316* (1), 57–77.

Chapter 4 Size-Dependent Carrier Kinetics and Photoelectrochemical Studies in CdS

4.1 Introduction

CdS quantum dots-sensitized TiO_2 has been studied for decades for photovoltaic applications.[1] As a semiconductor, one advantage of CdS is the tuning of the potential energy levels of conduction and valence bands by changing the quantum dots (QD) size, the so-called quantum size effect.[2] The most probable distance between the electron and hole in an exciton is called the exciton Bohr radius a_0. The exciton Bohr radius gives a length scale to describe the spatial extension of excitons in semiconductors, and ranges from about 2-50 nm depending on the semiconductor. As the semiconductor nanocrystal size approaches a_0, confinement starts to influence the exciton wave function, inducing changes in the density of electronic states and in the energy level separation, which leads to an increase of the bandgap E_g with decreasing size (E_g is proportional to $1/r^2$, r is the radius of the nanocrystals) and the appearance of discrete energy levels near the band edges.[3] This spatial confinement of excitons in semiconductor nanostructures is known as quantum confinement. Influence of quantum confinement is usually not observed for sizes larger than 2-3 times the exciton Bohr radius. It is worth noting that a_0 and E_g are correlated, the narrower the E_g, the larger the a_0. For example, the exciton Bohr radius for CdS (E_g ~ 2.4 eV) and CdSe (E_g ~ 1.8 eV) is 3.1 nm and 6.1 nm, respectively.[4] As a result, the optoelectronic properties of semiconductor nanocrystals are strongly size-dependent, making it

possible to tune the bandgap energy of semiconductor nanocrystals by changing the size of the nanocrystals. Accordingly, carrier kinetics such as electron transfer rate from CdS to TiO_2 will change as the varied conduction band position difference between CdS and TiO_2 when TiO_2 is sensitized with difference size of CdS QDs. Also, the electron-hole recombination rate changes due to altered band gap energy and surface states with different QDs size.[5] As band gap affects light absorption wavelength range and photoresponse corresponding to light absorption, the steady-state photoresponse of electrode can also be tuned by size quantization effects, that is, appropriate size can be tuned to optimize steady-state photoperformance. Successive ionic layer absorption and reaction (SILAR) method has been used to deposit CdS QDs onto mesoporous TiO_2 due to facile synthesis, controllable size and high photovoltaic performance.[5–9] Carrier kinetics such as interfacial electron transfer processes[10–13] and charge recombination[7,14] between CdS QDs and TiO_2, and steady-state photoresponses[15–17] have been investigated. While important, the research on the size-dependent charge transfer kinetics and steady-state photoresponse of CdS prepared by SILAR on TiO_2 is few. To our knowledge, the correlation of size-dependent carrier kinetics and photoresponse, containing photocurrent, photovoltage and photostability of CdS-TiO_2 photoelectrodes has not been published yet.

This chapter aims to study the effect of CdS QDs size on carrier kinetics and steady-state photoresponse and their intrinsic correlation in the CdS-sensitized TiO_2 photoelectrode. Femtosecond transient absorption spectroscopy (TAS) are employed to elucidate size-dependent carrier kinetics such as charge transfer kinetics and non-radiative recombination rate. Traditional photoelectrochemical (PEC) test methods are used to study PEC properties such as open circuit potential (EOC), photocurrent intensity and stability. Employing time-resolved technique as well as PEC measurements, a correlation between size-dependent carrier kinetics and photoelectrode

performance is demonstrated. In a more general perspective, this paper can contribute to the relevance of fundamental studies in rational development of PEC electrodes.

4.2 Experimental

4.2.1 Materials

Titanium tetrachloride (99.9%, ACROS), titanium oxide paste (Solaronix), zirconium dioxide paste (Solaronix), cadmium sulfate (≥ 99.0%, Alfa Aesar), sodium sulfide (≥ 98.0%, Avantor), urea (99.0%, Avantor), sodium sulfate (ACS grade, Ameresco). All chemicals were used as purchased.

4.2.2 Preparation of Photoelectrodes

The method to prepare TiO_2-CdS is same as descried in reference.[18] Briefly, fluorine-doped tin oxide (FTO) was cut into pieces with dimension of 6 cm × 0.8 cm (length × width) and subjected to ultrasonication in detergent solution, deionized water (DI) and ethanol for 30mins, respectively. Cleaned FTO pieces were immersed in 40 mM $TiCl_4$ solution, heated to 70 °C for 30 min and followed by annealing at 500 °C for 30 min to deposit a blocking layer. DSL 18NR-T TiO_2 paste was bladed onto a 0.8 cm^2 active area, dried at 80 °C for 1 h and then annealed at 500 °C for 1 h. A post-$TiCl_4$ solution treatment (same as to deposit blocking layer) was introduced to increase the roughness of surface. CdS was deposited on TiO_2 via SILAR by dipping TiO_2 electrodes alternatively in $CdSO_4$ (0.1 M) and Na_2S (0.1 M) aqueous solution for different cycles (1 min dipping and 30 s rinsing with DI water). TiO_2-CdS and ZrO_2-CdS used for transient absorption measurements are prepared on microslides.

4.2.3 Electrochemical and PEC Measurements

Photoelectrochemical measurements were carried out using a Gamry Interface 1000 potentiostat in a three-electrode configuration. The active area of the photoanode is 0.2 cm^2. A

150 W Xe lamp with an AM 1.5G filter was used to irradiate cells at 100 mW/cm^2. Linear sweep voltammetry measurements were recorded by sweeping potential at 50 mV/s. All photoelectrochemical measurements were conducted in de-aired electrolyte.

4.2.4 Optical Measurements

UV - visible absorption spectra of photoelectrodes were recorded by an Agilent Cary 60 spectrophotometer. Transient absorption measurements were recorded using a Clark MXR CPA-2010 (fundamental wavelength 775 nm, pulse duration 150 fs, pulse energy 1 mJ, repetition rate 1 kHz) incorporating Helios software provided by Ultrafast Systems. All samples investigated were placed in a quartz cell. Based on the designed experiment, the quartz cell was pumped vacuum or filled with degassed solution.

4.3 Results and Discussions

4.3.1 Optical Properties

Figure 4-1A shows the pictures of CdS-sensitized TiO_2 electrodes with different SILAR cycles of CdS. The color changes from light yellow to orange with increasing amount of CdS deposited on TiO_2. This color change is due to the quantum confinement effect. As the radius of a CdS nanoparticle changes, the photon energy of the first absorbance peak changes accordingly. Quantum effect is seen when CdS particle radius is lower than its Bohr radius (~ 3 nm).[19] Uv-vis spectra (Figure 4-1B) show a peak near the onset of absorption, which is ascribed to the first excitonic transition (1s to 1s). The onset of absorption is red-shifted with increasing radius as a consequence of size quantization effect. Figure 4-1C shows the normalized transient absorption spectra of TiO_2-CdS sensitized by different SILAR cycles of CdS quantum dots recorded 1 ps following 387 nm pulse excitation in vacuum. The bleach maximum of electrodes (Figure 4-1D) with different cycles of CdS coincides with the first exciton transition shown in uv-vis spectra

(Figure 4-1B). As is shown in Figure 4-1D, the maxium wavelength is red-shifted with increased cycles of CdS, which is in agreement of the onset of absorption in uv-vis spectra. The band gap is estimated by the first exciton peak maximum wavelength, which is shown in Figure 4-1E. As is shown, the band gap decreases with the inreased numbers of SILAR cycles of CdS. Based on the band gap, the particle size reaches about 5.1 nm at 15 SILAR cycles calculated from Brus equation.[20–23]

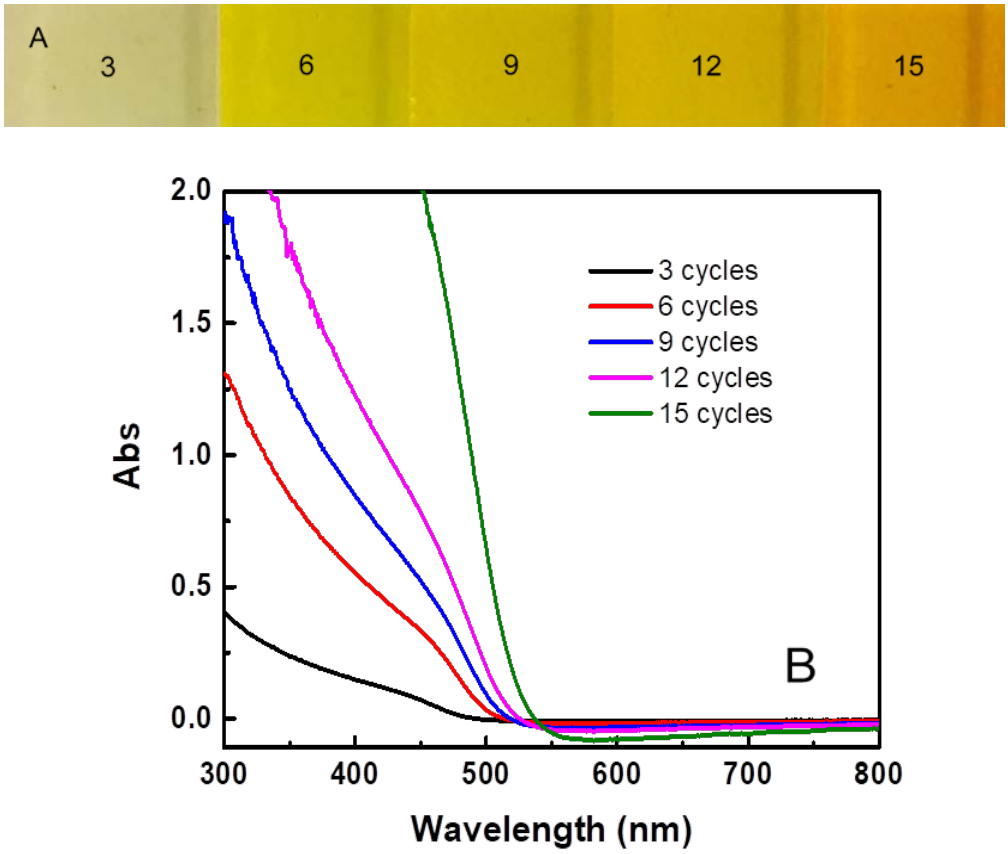

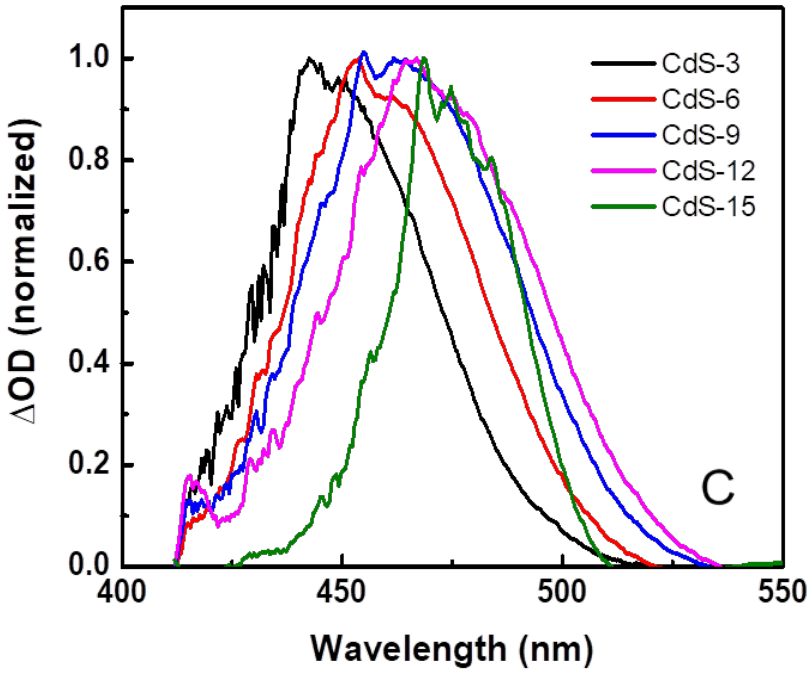
CdS-3
CdS-6
CdS-9
CdS-12
CdS-15
C
ΔOD (normalized)
Wavelength (nm)
0.0
0.2
0.4
0.6
0.8
1.0
400
450
500
550

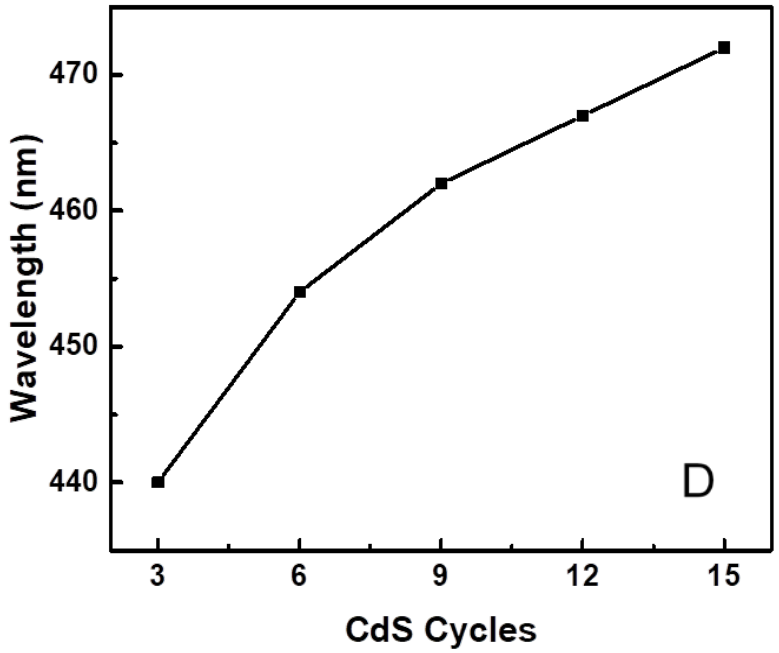
D
Wavelength (nm)
CdS Cycles
440
450
460
470
3
6
9
12
15

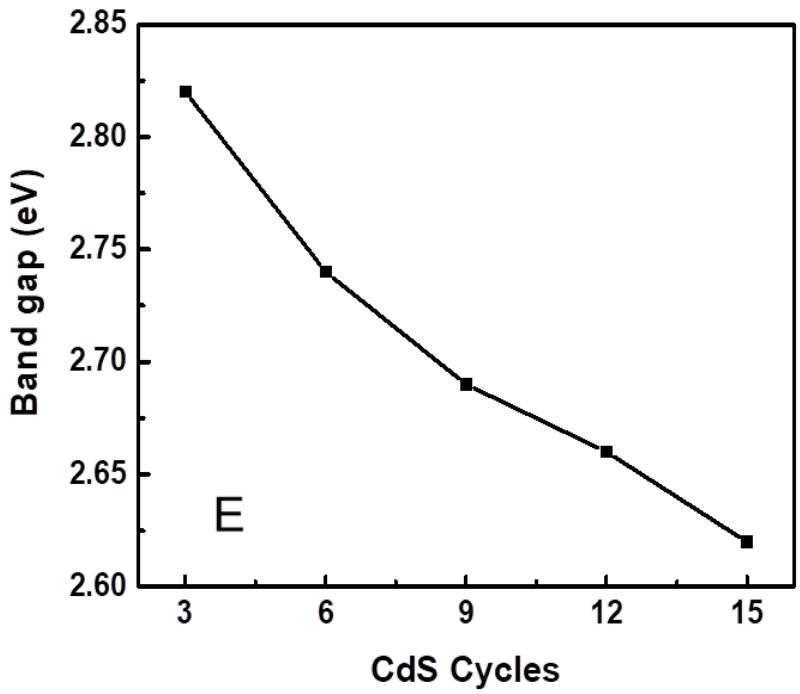

Figure 4-1. (A) Pictures show the color change of electrodes with different cycles of CdS. Numbers on pictures denote the SILAR cycles, (B) Uv-vis spectra, (C) normalized transient absorption spectra recorded 1 ps following 387 nm pulse excitation in vacuum, (D) first excitonic peak maximum wavelength, (E) band gap calculated based on first exciton peak maximum of TiO_2-CdS with different cycles of CdS prepared by SILAR.

4.3.2 Trap-mediated Non-radiative Recombination

Femtosecond transient absorption spectroscopy is employed to study the transient charge kinetics. To study the change of non-radiative recombination rate with different cycles of CdS, we deposited CdS by SILAR on mesoporous ZrO_2 on microslides. As bleach recovery is due to electron depopulation in conduction band of CdS. As ZrO_2 will not accept electrons transfer from CdS, the bleach recovers via charge recombination and trapping processes in CdS quantum dots. The decay kinetics of the transient bleach can be fitted using linear combination of multiexponential components according to equation 4-1:

$$y = \sum_i A_i e^{-t/\tau_i} \qquad (4\text{-}1)$$

where A_i and τ_i is the relative amplitude and time constant for the ith component, respectively. The bleach decay of ZrO_2-CdS with different cycles of CdS is tri-exponentially fitted and is shown in Figure 4-2A. As is shown, the bleach decay rate is decreasing with the increased SILAR cycles of CdS, and since the bleach decay is due to trap-mediated non-radiative recombination of electrons and holes in this scenario, the non-radiative recombination rate is reduced with increased cycles of CdS. The average time constant and corresponding rate constant for the excited state decay process can then be calculated using equations (4-2) and (4-3).

$$\tau_{ave} = \frac{\sum A_i \tau_i^2}{\sum A_i \tau_i} \qquad (4\text{-}2)$$

$$k = \frac{1}{\tau_{ave}} \qquad (4\text{-}3)$$

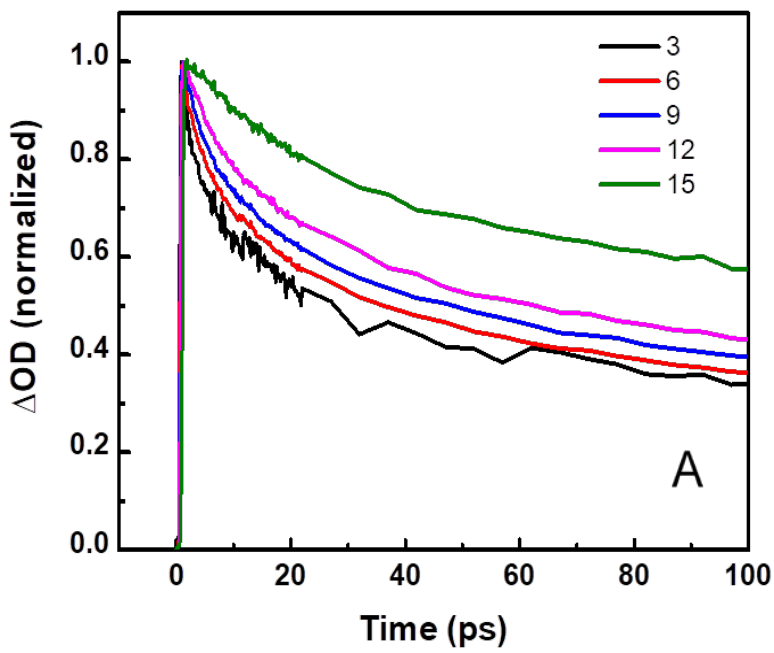

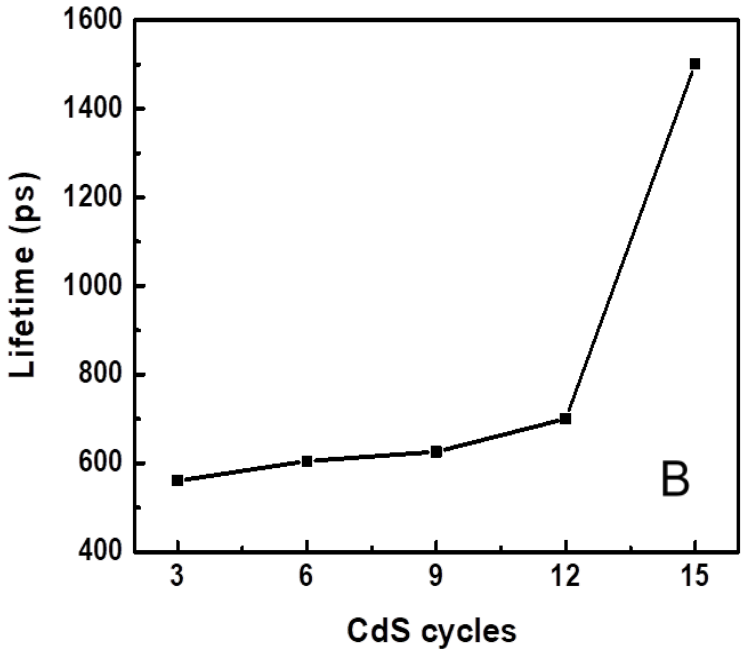

Figure 4-2. (A) Transient bleach decay and (B) lifetime in vacuum of ZrO_2-CdS with different SILAR cycles of CdS.

The calculated average time constant at different CdS cycles is shown in Figure 2B and corresponding rate constant is shown in table 4-1. The lifetime increases and accordingly bleach decay rate constant decreases with the increased cycles of CdS. This can be attributed to the reduced grain boundaries and interfaces as well as surface states in larger size particles, which suppress charge trapping and hence reduce the trap-mediated recombination rate at the particle interfaces.[24]

Table 4-1. Bleach decay rate constant in vacuum of ZrO_2-CdS

Cycles	**3**	**6**	**9**	**12**	**15**
Rate constant (s^{-1})	1.8×10^9	1.7×10^9	1.6×10^9	1.4×10^9	6.7×10^8

4.3.3 Electron Transfer from CdS to TiO_2

As the potential energy level of conduction band edge of CdS is more negative than that of TiO_2, photoexcited electrons will transfer from CdS to TiO_2 following CdS excitation. Figure 4-3A to E show the bleach decay rate of TiO_2-CdS and ZrO_2-CdS with different SILAR cycles of CdS. The bleach decay rate of TiO_2-CdS is faster than that of ZrO_2- CdS, this is because in addition to non-radiative recombination in TiO_2-CdS, the electrons can also transfer from CdS to TiO_2 as mentioned above, which also contributes to the bleach decay. As in ZrO_2, the bleach decay is attributed to the non-radiative recombination, the difference in bleach decay rate between TiO_2-CdS and ZrO_2-CdS is the electron transfer rate from CdS to TiO_2, that is,

$$k_{et} = k_{TiO2-CdS} - k_{ZrO2-CdS} \quad (4\text{-}4)$$

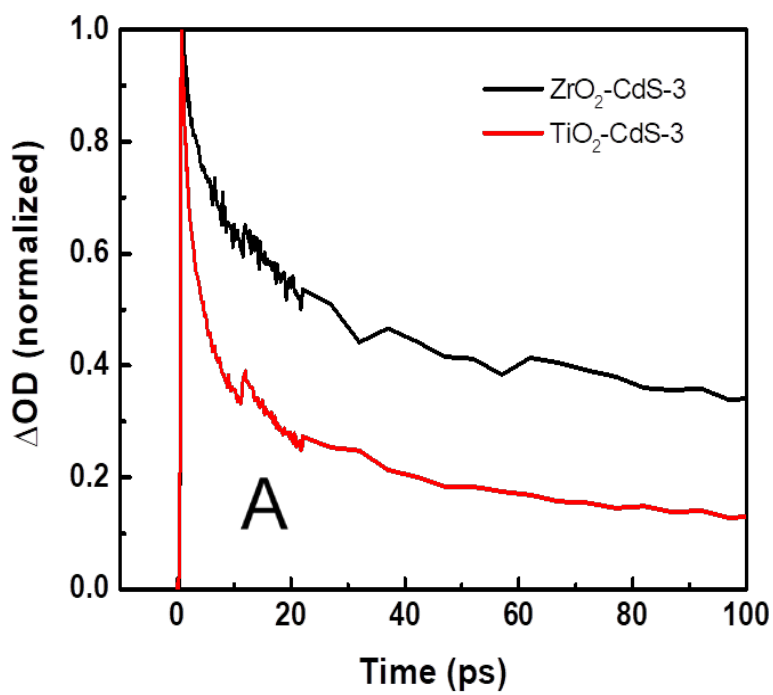

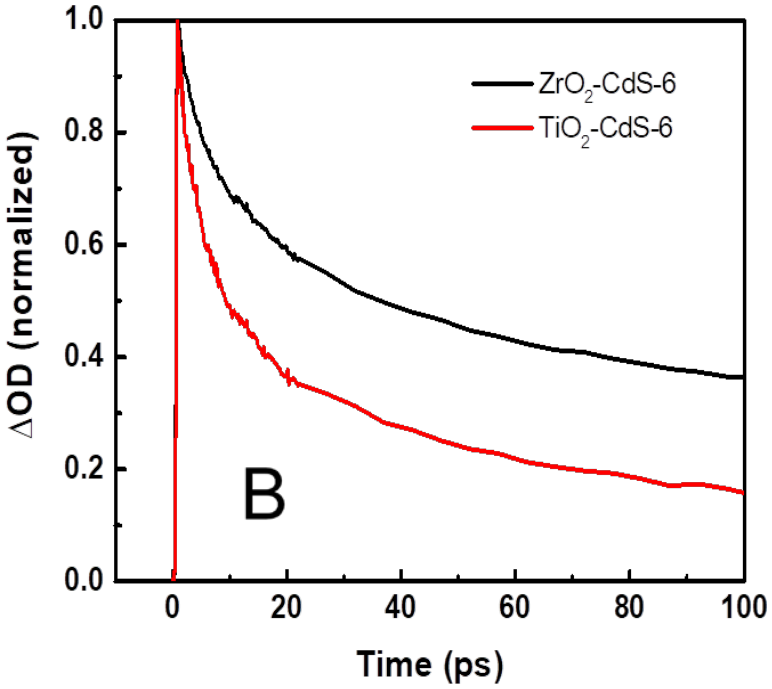
1.0
0.8
0.6
0.4
0.2
0.0
ΔOD (normalized)
0
20
40
60
80
100
Time (ps)
ZrO2-CdS-6
TiO2-CdS-6
B

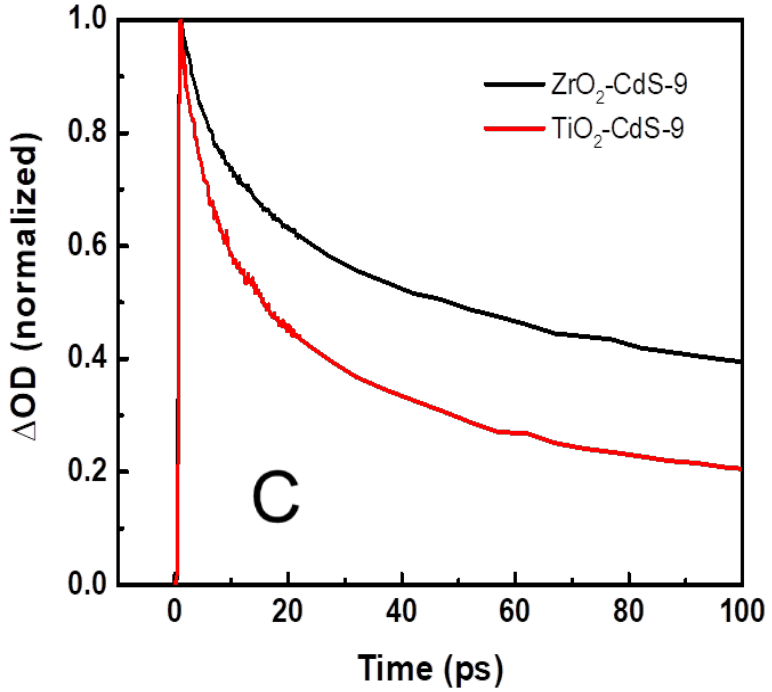
1.0
0.8
0.6
0.4
0.2
0.0
ΔOD (normalized)
0
20
40
60
80
100
Time (ps)
ZrO2-CdS-9
TiO2-CdS-9
C

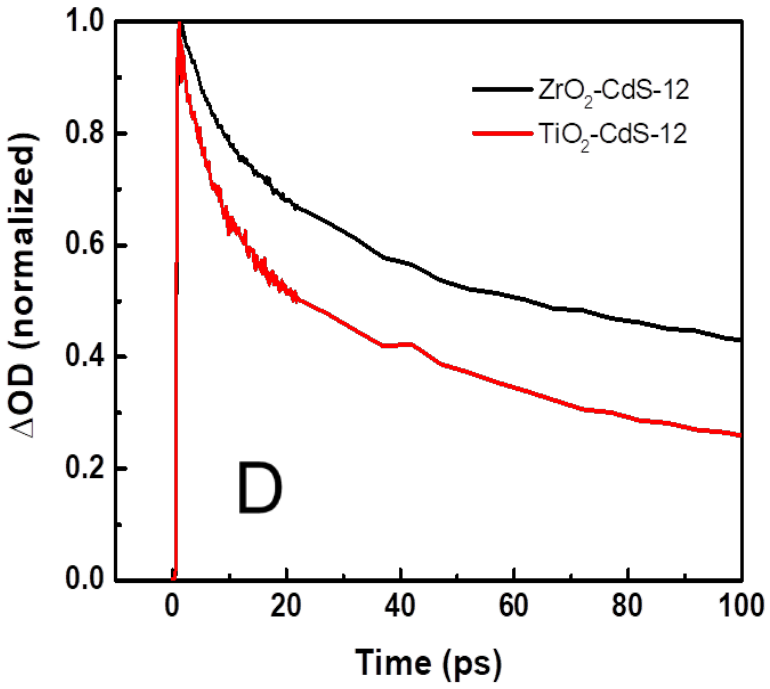
1.0
0.8
0.6
0.4
0.2
0.0
ΔOD (normalized)
0
20
40
60
80
100
Time (ps)
ZrO2-CdS-12
TiO2-CdS-12
D

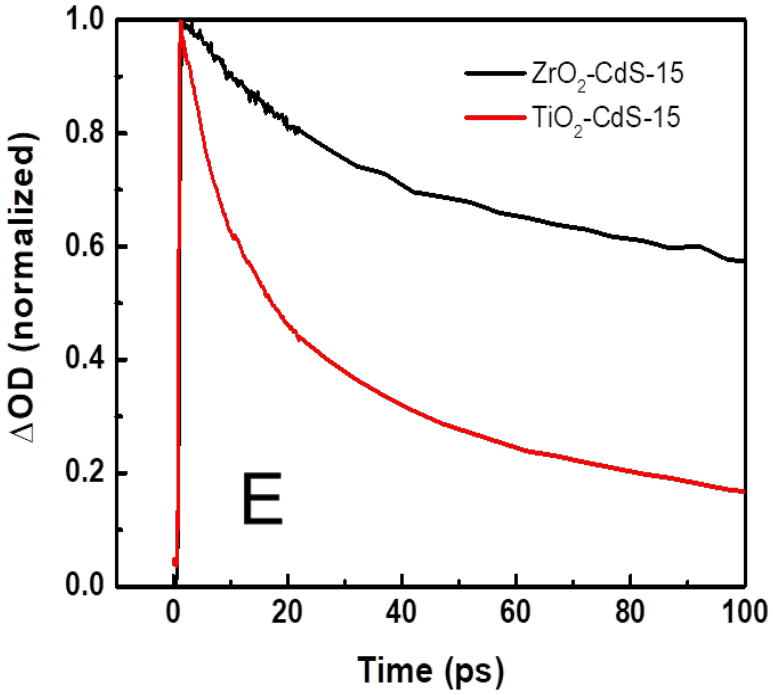
1.0
0.8
0.6
0.4
0.2
0.0
ΔOD (normalized)
0
20
40
60
80
100
Time (ps)
ZrO2-CdS-15
TiO2-CdS-15
E

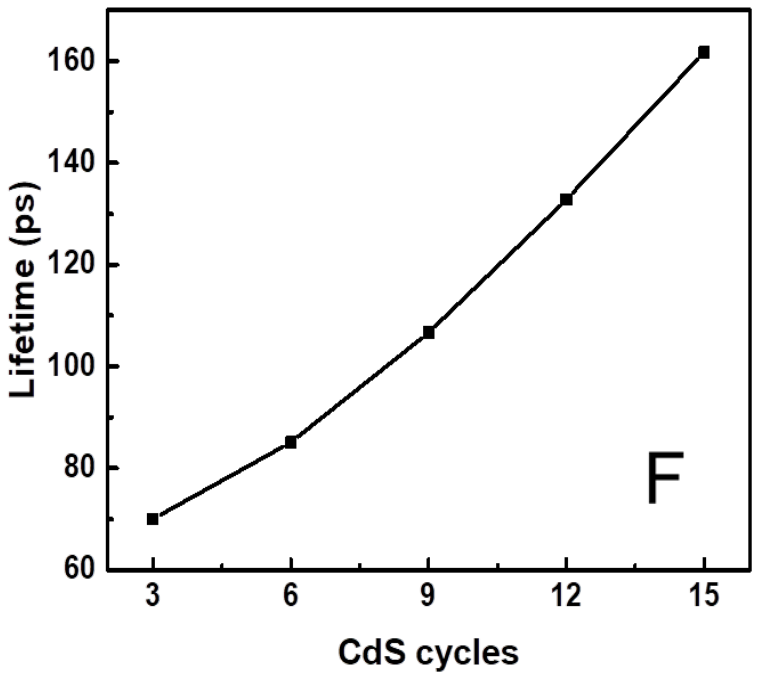
Lifetime (ps)
160
140
120
100
80
60
3
6
9
12
15
CdS cycles
F

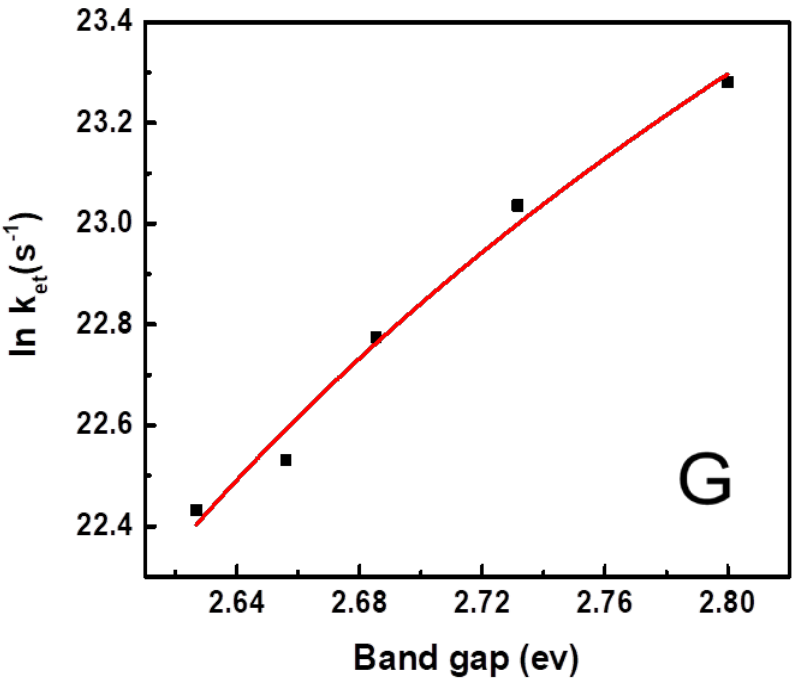
ln $k_{et}(s^{-1})$
23.4
23.2
23.0
22.8
22.6
22.4
2.64
2.68
2.72
2.76
2.80
Band gap (ev)
G

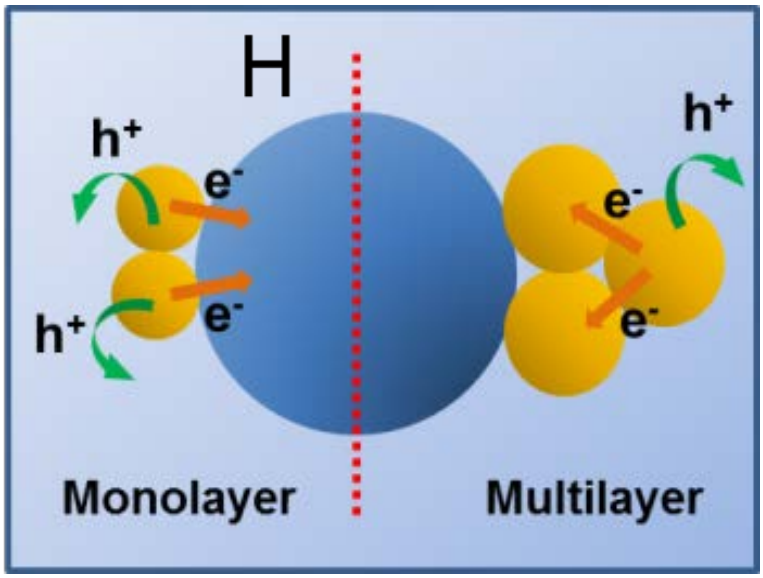

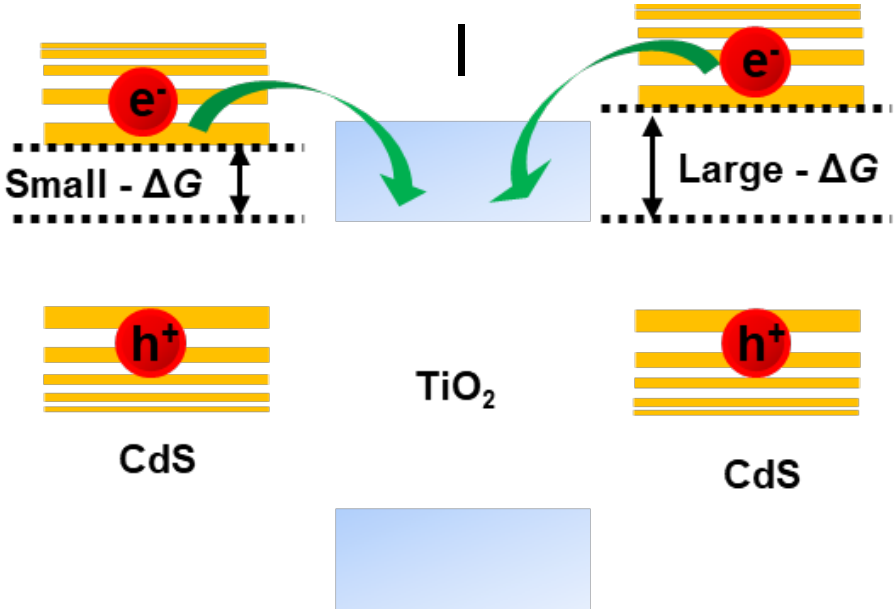

Figure 4-3. (A) (B) (C) (D) (E) Comparison of transient absorption bleach decay of TiO_2-CdS and ZrO_2-CdS with different cycles of CdS in vacuum, (F) bleach decay lifetime of TiO_2-CdS with difference cycles of CdS in vacuum, (G) dependence of electron transfer rate constant on band gap, solid line is quadratically fitted. Schematic representation of electron transfer (H) pathways and (I) driving force in TiO_2-CdS with different particle size of CdS.

As is shown in Figure 4-3F, the lifetime of electrons increases with increased SILAR cycles of CdS on TiO_2-CdS, which is attributed to firstly, the suppressed charge trapping and trap-mediated recombination rate at particle interfaces due to reduced surface area and interfaces as well as surface states in larger size particles, which is the same reason as that in ZrO_2-CdS. Secondly, CdS loading amount increases with increasing SILAR cycles. Therefore, for a low number of cycles, all the CdS QDs contact directly with the TiO_2 porous substrate, favoring electron transfer from CdS to TiO_2. However, for a large number of cycles, a fraction of QDs are not in direct contact with TiO_2, hence electrons can only transfer through another CdS QDs before reaching TiO_2, which retards electrons transfer (Figure 4-3H). Thirdly, the average CdS QDs size increases with an increase in the number of CdS cycles, which means, an increase in the average distance of the CdS QDs to TiO_2 substrate. This would lead to an increase in the average time needed to transfer electrons from CdS QDs to TiO_2[6,23] (Figure 4-3H). Last but not least, the potential difference between conduction band edge of CdS and TiO_2 becomes smaller with increasing CdS cycles due to quantum confinement effect. That means, electron transfer from CdS to TiO_2 becomes slower as the size of the CdS QDs gets larger, due to a decreased driving force $-\Delta G$ for electron transfer as the CdS conduction band edge shifts toward higher energies (less negative), as is shown in Figure 4-3I. The electron transfer rate for TiO_2-CdS with different SILAR cycles of CdS is calculated by using equations (4-1) - (4-4), and the results are listed in table 4-2. The logarithm of electron transfer rate is quadratically increasing with respect to the band gap (Figure 4-1G). As the effective mass of holes is about 4 times that of electrons in CdS, the band gap change is mainly the position change of conduction band edge, leading to the variation of driving force.[25] That means, the logarithm of electron transfer rate is quadratically

changing with driving force -Δ*G*, the higher the driving force, the faster the electron transfer rate, which is in agreement with Marcus theory.[26]

Table 4-2. Electron transfer rate constant from CdS to TiO_2 in vacuum

Cycles	3	6	9	12	15
Rate constant (s^{-1})	1.3×10^{10}	1.0×10^{10}	7.8×10^{9}	6.1×10^{9}	5.5×10^{9}

4.3.4 Steady-state Photoresponse

Figure 4-4A shows the photocurrent density change with SILAR cycles of CdS and illumination time. The photocurrent comes from the photooxidation of CdS and oxidation of urea by photogenerated holes in CdS photoanode in three-electrode system,[18] hence the photocurrent variation reveals the utilization of changed available holes. Figure 4-4B shows the dependence of the photocurrent density on the SILAR cycles. The photocurrent density first increases and reaches its maximum at 9 cycles. This is because with the increase of CdS cycles, the band gap energy decreases and the amount of CdS increases. The reduced band gap and increment of QDs loading amount ensure enhanced absorption of light (Figure 4-1A) and hence more photoexcited carriers as expected, which contribute to photocurrent density. For further increase in CdS cycles to 12 and 15, the photocurrent density decreases. This behavior can be attributed to four reasons. First, with the increase in loading amount of CdS QDs, the possibility of blocking of the TiO_2 mesopores increases, which leads to reduced contact area of electrolyte and CdS QDs and hence unfavorable hole transport at QDs /electrolyte interface (Figure 4-4F). Second, as mentioned in section *electron transfer from CdS to TiO_2*, multilayer of CdS QDs induces increased diffusion distance and transfer time of electrons, which lead to increased chance of recombination of holes

and electrons. The recombination could occur in the same QDs or in nearby ones or in electrolyte through electron back transfer and recombine with holes captured by electrolyte. Third, the surface trap states decrease with increased QDs size (as shown in section *trap-mediated non-radiative recombination*), which means less holes are trapped by surface states or sulfur dangling bonds on QDs surface. As sulfur dangling bonds S^{2-} capture holes and are oxidized at photoelectrode / aqueous electrolyte interface, the so-called photocorrosion,[18] which also contributes to photocurrent density. In addition, the valence band edge of CdS moves towards lower energy potentials (more negative) with decreased band gap when QDs size is increasing. The driving force for hole transfer, potential difference between valence band edge of CdS and S^{2-} oxidation becomes smaller, leading to reduced photocorrosion and photocurrent density. This can be proved by Figure 4C, photocurrent stability improves with increased cycles of CdS. After 200 s illumination, photocurrent obtained by electrode with 3 cycles of CdS is about 47% of its initial value, while the number for 15 cycles is 99%. After 600 s illumination, there is no CdS on TiO_2 surface as is shown in Figure 4-4A for electrode with 3 cycles of CdS, the stable photocurrent comes from light absorption of TiO_2 but not CdS. While for electrode with 15 cycles of CdS, the photocurrent density is 80% of its initial value. Figure 4-4D and 4-4E shows the open circuit potential change with varied cycles of CdS. As is shown, it first moves toward higher potential levels (more negative) for the first 9 cycles of CdS, and then moves toward lower potential levels (less negative) for 12 and 15 cycles. As open circuit potential is the potential difference between quasi-fermi level of TiO_2-CdS and redox potential in electrolyte,[27] a negative shift of potential suggests more electron accumulation in the photoelectrode. The first negative shift is due to more electrons generated caused by enhanced light absorption as discussed above, and the positive shift can be attributed to the decreasing band gap and hence

positively shifted fermi level. The similarities in the trends observed for photocurrent density and open circuit potential, that is, the higher the photocurrent intensity, the higher the open circuit potential, reveal that the steady state photoresponses are related.

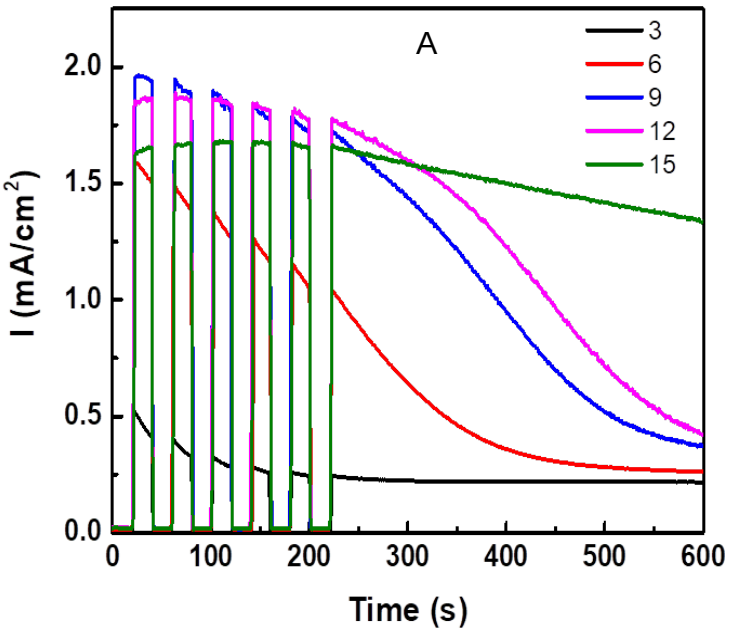

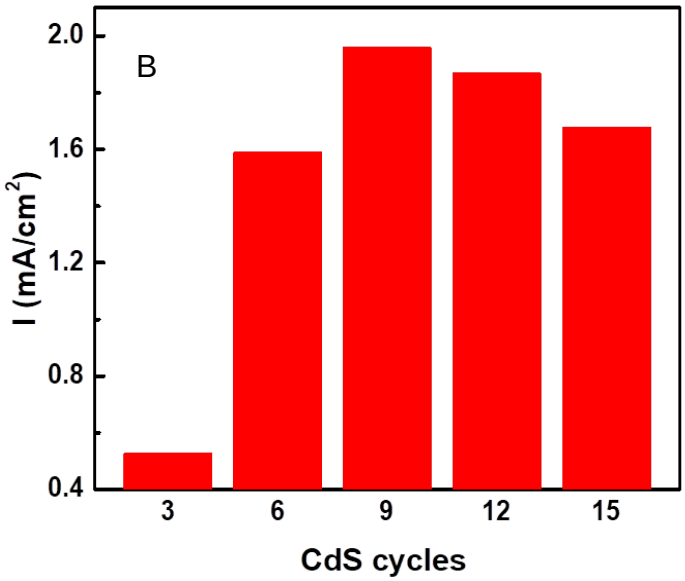

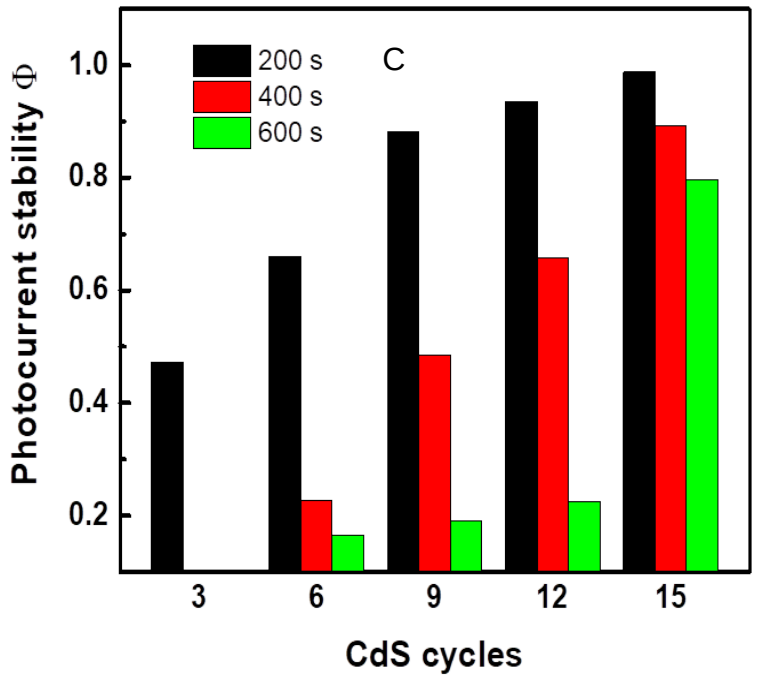
200 s
400 s
600 s
C
Photocurrent stability Φ
1.0
0.8
0.6
0.4
0.2
3
6
9
12
15
CdS cycles

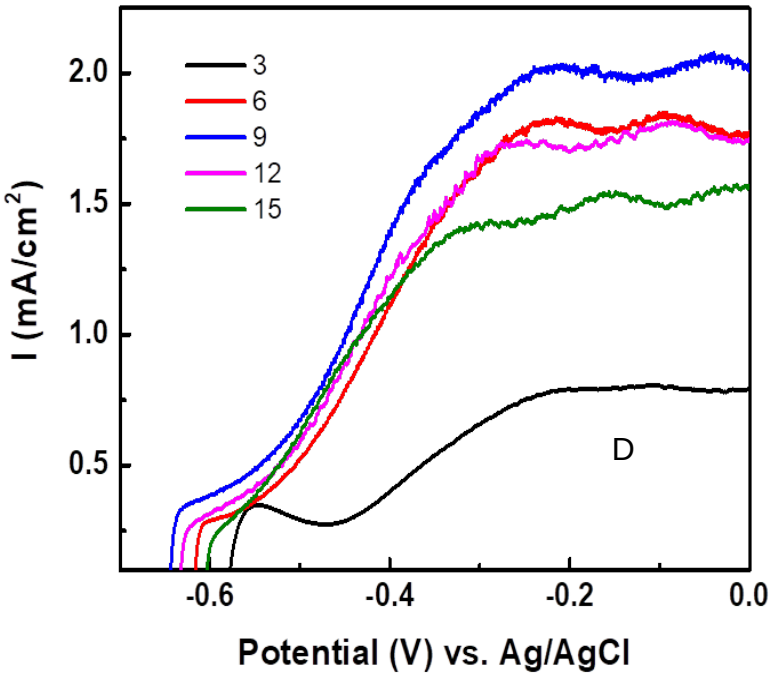
3
6
9
12
15
D
I (mA/cm2)
2.0
1.5
1.0
0.5
-0.6
-0.4
-0.2
0.0
Potential (V) vs. Ag/AgCl

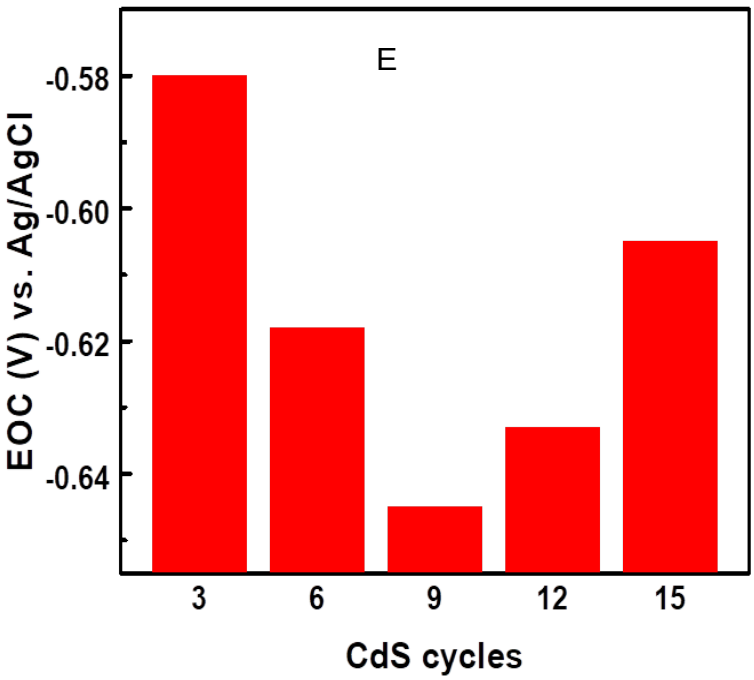

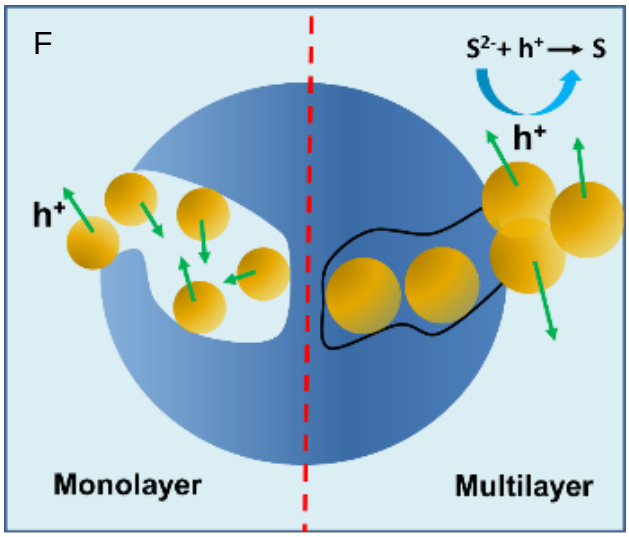

Figure 4-4. (A) Chronoamperometry results of TiO_2-CdS with different cycles of CdS, (B) initial values (highest values) of photocurrent density upon illumination, (C) photocurrent stability change after a period time of illumination for different cycles of CdS. The parameter Φ is defined as the photocurrent density divided by the initial value (the highest value) of photocurrent density, (D) linear sweep voltammetry scan of TiO_2-CdS with different cycles of CdS, (E) open circuit potential change with different cycles of CdS, (F) schematic representation of hole capture in mesopores in TiO_2 at low numbers of CdS cycles and blocking of mesopores at larger numbers of CdS cycles. All photoelectrochemical test are conducted under illumination light intensity of 100 mW/cm^2 in deaired 1 M Na_2SO_4 + 0.33 M urea solution.

4.4 Summary

CdS QDs were successfully loaded on mesoporous TiO_2 by SILAR method. Uv-vis showed the red shift of absorption peak, showing the narrowing of band gap with increasing CdS particle size due to quantum confinement effect. Transient absorption spectroscopy results showed that the trap-mediated non-radiative recombination rate was reduced with increased cycles of CdS. Electron transfer rate from CdS to TiO_2 with different cycles of CdS were probed and calculated, and the logarithm of electron transfer rate obtained was a quadratic function with respect to band gap. Photoelectrochemical tests results indicated that the photocurrent density first increased and then decreased. Stability of photoelectrode enhanced with increased cycles of CdS. Open circuit potential showed the similar trends as photocurrent density, revealing the interconnection of photocurrent and open circuit potential.

References

(1) Gerischer, H.; Lübke, M. A Particle Size Effect in the Sensitization of TiO_2 Electrodes by a CdS Deposit. *J. Electroanal. Chem. Interfacial Electrochem.* **1986**, *204* (1), 225–227.

(2) Wang, Y.; Herron, N. Nanometer-Sized Semiconductor Clusters: Materials Synthesis, Quantum Size Effects, and Photophysical Properties. *J. Phys. Chem.* **1991**, *95* (2), 525–532.

(3) Alivisatos, A. P. Perspectives on the Physical Chemistry of Semiconductor Nanocrystals. *J. Phys. Chem.* **1996**, *100* (31), 13226–13239.

(4) Tian, J.; Cao, G. Semiconductor Quantum Dot-Sensitized Solar Cells. *Nano Rev.* **2013**, *4*, 22578–22585.

(5) Vogel, R.; Pohl, K.; Weller, H. Sensitization of Highly Porous, Polycrystalline TiO_2 Electrodes by Quantum Sized CdS. *Chem. Phys. Lett.* **1990**, *174* (3), 241–246.

(6) Zhang, Q.; Zhang, Y.; Huang, S.; Huang, X.; Luo, Y.; Meng, Q.; Li, D. Application of Carbon Counterelectrode on CdS Quantum Dot-Sensitized Solar Cells (QDSSCs). *Electrochem. Commun.* **2010**, *12* (2), 327–330.

(7) Tachibana, Y.; Umekita, K.; Otsuka, Y.; Kuwabata, S. Charge Recombination Kinetics at an in Situ Chemical Bath-Deposited CdS/Nanocrystalline TiO_2 Interface. *J. Phys. Chem. C* **2009**, *113* (16), 6852–6858.

(8) Nakamura, R.; Makuta, S.; Tachibana, Y. Electron Injection Dynamics at the SILAR Deposited CdS Quantum Dot/TiO_2 Interface. *J. Phys. Chem. C* **2015**, *119* (35), 20357–20362.

(9) Zhou, R.; Zhang, Q.; Tian, J.; Myers, D.; Yin, M.; Cao, G. Influence of Cationic Precursors on CdS Quantum-Dot-Sensitized Solar Cell Prepared by Successive Ionic Layer Adsorption and Reaction. *J. Phys. Chem. C* **2013**, *117* (51), 26948–26956.

(10) Lin, K. H.; Chuang, C. Y.; Lee, Y. Y.; Li, F. C.; Chang, Y.-M.; Liu, I. P.; Chou, S. C.; Lee, Y. L. Charge Transfer in the Heterointerfaces of CdS/CdSe Cosensitized TiO_2 Photoelectrode. *J. Phys. Chem. C* **2012**, *116* (1), 1550–1555.

(11) Blackburn, J. L.; Selmarten, D. C.; Nozik, A. J. Electron Transfer Dynamics in Quantum Dot/Titanium Dioxide Composites Formed by in Situ Chemical Bath Deposition. *J. Phys. Chem. B* **2003**, *107* (51), 14154–14157.

(12) Mazumdar, S.; Roy, K.; Srihari, V.; Umapathy, S.; Bhattacharyya, A. J. Probing Ultrafast Photoinduced Electron Transfer to TiO_2 from CdS Nanocrystals of Varying Crystallographic Phase Content. *J. Phys. Chem. C* **2015**, *119* (30), 17466–17473.

(13) Yagi, I.; Mikami, K.; Ebina, K.; Okamura, M.; Uosaki, K. Size-Dependent Carrier Dynamics in CdS Nanoparticles by Femtosecond Visible-Pump/IR-Probe Measurements. *J. Phys. Chem. B* **2006**, *110* (29), 14192–14197.

(14) Liu, X.; Zhang, Q.; Xing, G.; Xiong, Q.; Sum, T. C. Size-Dependent Exciton Recombination Dynamics in Single CdS Nanowires beyond the Quantum Confinement Regime. *J. Phys. Chem. C* **2013**, *117* (20), 10716–10722.

(15) Esparza, D.; Zarazúa, I.; López-Luke, T.; Cerdán-Pasarán, A.; Sánchez-Solís, A.; Torres-Castro, A.; Mora-Sero, I.; De la Rosa, E. Effect of Different Sensitization Technique on the Photoconversion Efficiency of CdS Quantum Dot and CdSe Quantum Rod Sensitized TiO_2 Solar Cells. *J. Phys. Chem. C* **2015**, *119* (24), 13394–13403.

(16) Huang, F.; Zhang, L.; Zhang, Q.; Hou, J.; Wang, H.; Wang, H.; Peng, S.; Liu, J.; Cao, G. High Efficiency CdS/CdSe Quantum Dot Sensitized Solar Cells with Two ZnSe Layers. *ACS Appl. Mater. Interfaces* **2016**, *8* (50), 34482–34489.

(17) Banerjee, S.; Mohapatra, S. K.; Das, P. P.; Misra, M. Synthesis of Coupled Semiconductor by Filling 1D TiO_2 Nanotubes with CdS. *Chem. Mater.* **2008**, *20* (21), 6784–6791.

(18) Zhao, R.; Schumacher, G.; Leahy, S.; Radich, J. G. $Ni(OH)_2$ as Hole Mediator for Visible Light-Induced Urea Splitting. *J. Phys. Chem. C* **2018**, *122* (25), 13995–14003.

(19) Kurian, P.; Vijayan, C.; Sathiyamoorthy, K.; Suchand Sandeep, C.; Philip, R. Excitonic Transitions and Off-Resonant Optical Limiting in CdS Quantum Dots Stabilized in a Synthetic Glue Matrix. *Nanoscale Res. Lett.* **2007**, *2* (11), 561–568.

(20) Lippens, P. E.; Lannoo, M. Calculation of the Band Gap for Small CdS and ZnS Crystallites. *Phys. Rev. B* **1989**, *39* (15), 10935–10942.

(21) Brus, L. E. Electron–electron and Electron-hole Interactions in Small Semiconductor Crystallites: The Size Dependence of the Lowest Excited Electronic State. *J. Chem. Phys.* **1984**, *80* (9), 4403–4409.

(22) Brus, L. Electronic Wave Functions in Semiconductor Clusters: Experiment and Theory. *J. Phys. Chem.* **1986**, *90* (12), 2555–2560.

(23) Jin-nouchi, Y.; Naya, S.; Tada, H. Quantum-Dot-Sensitized Solar Cell Using a Photoanode Prepared by in Situ Photodeposition of CdS on Nanocrystalline TiO_2 Films. *J. Phys. Chem. C* **2010**, *114* (39), 16837–16842.

(24) Nie, W.; Tsai, H.; Asadpour, R.; Blancon, J. C.; Neukirch, A. J.; Gupta, G.; Crochet, J. J.; Chhowalla, M.; Tretiak, S.; Alam, M. A.; et al. High-Efficiency Solution-Processed Perovskite Solar Cells with Millimeter-Scale Grains. *Science* **2015**, *347* (6221), 522–525.

(25) Mics, Z.; Němec, H.; Rychetský, I.; Kužel, P.; Formánek, P.; Malý, P.; Němec, P. Charge Transport and Localization in Nanocrystalline CdS Films: A Time-Resolved Terahertz Spectroscopy Study. *Phys. Rev. B* **2011**, *83* (15), 155326.

(26) Tvrdy, K.; Frantsuzov, P. A.; Kamat, P. V. Photoinduced Electron Transfer from Semiconductor Quantum Dots to Metal Oxide Nanoparticles. *Proc. Natl. Acad. Sci.* **2011**, *108* (1), 29–34.

(27) Raga, S. R.; Barea, E. M.; Fabregat-Santiago, F. Analysis of the Origin of Open Circuit Voltage in Dye Solar Cells. *J. Phys. Chem. Lett.* **2012**, *3* (12), 1629–1634.

Chapter 5 Effect of Solvent on Charge Kinetics and Hole Transfer from CdS to Urea

5.1 Introduction

Quantum dots (QDs) of II-VI semiconductors have been extensively researched during the past two decades.[1] QDs have a large ratio of surface to volume, therefore, the surface of QDs plays a crucial role in their electronic and optical properties. One important application of QDs is their fluorescence. The first and most desirable mode for fluorescent applications is the direct band edge emission, and the second stems from trapping of holes in a midgap state that results in the non-band-edge recombination referred to as trap emission. Attachment of functional groups on surface of QDs is the most commonly used way to passivate the surface detects and trap states. Ligand functional groups that bind to the QD surface can induce or remediate trapping effects based on the electron donating or withdrawing properties of the groups.[2] For example, thiols are the most widely used ligands to stabilize semiconductors.[3,4] Surface coating with thiol molecules can obtain excellent fluorescence properties by efficiently quench surface traps. In addition to the use of thiols to passivate the surfaces of QDs, researchers employed various amines to modify the electronic and optical properties of QDs.[5–8] The electron donating amine group interact with QDs surface and fill surface traps.[9] The magnitude of the interaction between amine ligands and QDs are found to be correlated with the intrinsic basicity of the amines.

In Cd-containing semiconductors such as CdS, CdSe and CdTe, amines can coordinate with Cd atoms[10] or dissolve Cd atoms into the solvent and passivate the Cd dangling bonds on the surface.[11] The nonbonding lone pair of electrons from N atoms in amine is donated to a vacant orbital at surface Cd sites to provide the bonding interaction,[12] changing electrical or optical properties and influencing the rate of surface recombination through interactions with surface states.[2] The methylene protons on primary amine can passivate the dangling S, Se and Te trap sites and curtail nonradiative decay, leading to enhanced band edge emission and absent deep trap emission. Besides, amides were observed to form N-H dissociation structures with interdimer interactions and kinetically favored oxygen dative-bonded structures,[13] which make them possible the ligand for surface passivation. However, the related research about the passivation of amides on QDs surface is rare. Urea is a kind of amides, so it can passivate QDs surface theoretically. It has been proven that urea can accept holes mediated by electrochemical catalyst $Ni(OH)_2$ from CdS.[14] No research has been done on directly hole transfer from CdS to urea yet. This chapter will elucidate the surface passivation of urea on CdS QDs and hole transfer from CdS to urea.

5.2 Experimental

5.2.1Materials

Zirconium dioxide paste (Solaronix), cadmium sulfate (≥ 99.0%, Alfa Aesar), sodium sulfide (≥ 98.0%, Avantor), urea (99.0%, Avantor), sodium sulfate (ACS grade, Ameresco), cadmium oxide (≥ 99.998%, Alfa Aesar), sulfur powder (99.8%, Alfa Aesar), toluene (99.5%, Macron), dimethyl sulfoxide (99.9%, BDH), acetone (≥ 99.5%, BDH), oleic acid (99%, Alfa Aesar), octadecene (99%, Alfa Aesar), methanol (≥ 99.8%, EMD), All chemicals were used as purchased.

5.2.2 Preparation of CdS Quantum Dots

51mg of CdO, 1.8ml of oleic acid and 18.1ml of octadecene were loaded into a 3-neck flask and heated to 295°C under nitrogen with stirring. 6.4mg of sulfur powder were dissolved in 10ml of octadecene and injected into flask. After 3mins of growth at 250°C, the solution was cooled to room temperature and precipitated with acetone. After that, CdS QDs were then dissolved in toluene and precipitated with methanol.

5.2.3 Preparation of CdS on Microslides

DSL 18NR-T TiO_2 paste was bladed on microslides, dried at 80 °C for 1 h and then annealed at 500 °C for 1 h. CdS was deposited on TiO_2 via SILAR by dipping TiO_2 microslides alternatively in $CdSO_4$ (0.1 M) and Na_2S (0.1 M) aqueous solution for different cycles (1 min dipping and 30 s rinsing with DI water).

5.2.4 Optical Measurements

UV - visible absorption spectra of photoelectrodes were recorded by an Agilent Cary 60 spectrophotometer. Fluorescence spectra were obtained by an PTI QuantaMaster 4 under excitation with wavelength of 480nm. Transient absorption measurements were recorded using a Clark MXR CPA-2010 (fundamental wavelength 775 nm, pulse duration 150 fs, pulse energy 1 mJ, repetition rate 1 kHz) incorporating Helios software provided by Ultrafast Systems. All samples investigated were placed in a quartz cell. Based on the designed experiment, the quartz cell was pumped vacuum or filled with degassed solution.

5.3 Results and Discussions

5.3.1 Optical Properties of CdS QDs

Figure 5-1 (A) shows the UV-vis spectrum of CdS QDs in toluene, and the first excitonic peak is around 480nm, revealing that the band gap of the QDs prepared is about 2.58 eV. Figure

5-1 (B) is the normalized fluorescence spectra of CdS QDs in DMSO and DMSO-urea solution. There are two peaks in fluorescence spectra centered at 725nm and 800nm, corresponding to band-to-band emission and trap emission, respectively. On the CdS nanocrystals surface, unoccupied valence orbitals of Cd and nonbonding valence electrons of S act as electron and hole traps, respectively[15]. The trap emission is attributed to hole trapping to the dangling S bonds on the nanocrystal surface and recombine radiatively with the electron,[16] and it is an indication of the poor surface passivation of the as-prepared CdS QDs.[17] The deep trap emission is not separated to the band-to-band emission, and this is attributed to size distribution and trap energy levels lie close to the valence band in energy.[18] The radiative emission decreases more when there is urea in the DMSO, and this can be attributed to the photogenerated holes transfer from CdS to urea, which decreases the radiative recombination of electrons and holes. The trap emission also decreases with the addition of urea due to passivation of trap states. In urea, negative charges are mainly accumulated on oxygen-containing groups carbonyl (–C=O).[19] The oxygen atoms have a much stronger electronegativity than the nitrogen atom, they can attract more charges of $–NH_2$ and reduce the charge density of $–NH_2$, So the $–NH_2$ can be easily absorbed on the surface of the QDs[20] to passivate the surface and to accept holes from QDs. The surface passivation and hole transfer from CdS to urea will lead to increased and decreased radiative emission, respectively. The radiative emission obtained in this research decreases, showing that the hole transfer from CdS to urea is more significant than urea passivation on CdS QDs surface. The fluorescence quench can be explained theoretically. As discussed above, due to different electronegatively, electrons on the nitrogen is delocalized into the carbonyl, thus forming a partial double bond between N and the carbonyl carbon. The electron density near O is larger than that near N, then the binding interaction may occur between O atoms of the ligand

and Cd atoms and H atoms on S atoms on the QD surface,[21,22] indicating that electron transfer occurs from urea to CdS. The residual charges on S and Cd of CdS QDs are the main source of the radiative recombination surface state centers; therefore, the residual charges on S and Cd of CdS clusters decrease, the radiative recombination decreases accordingly.[22]

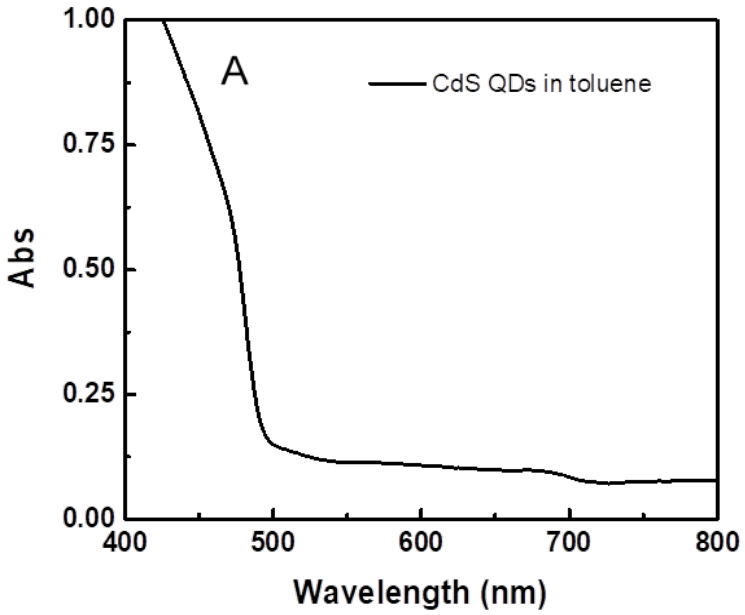

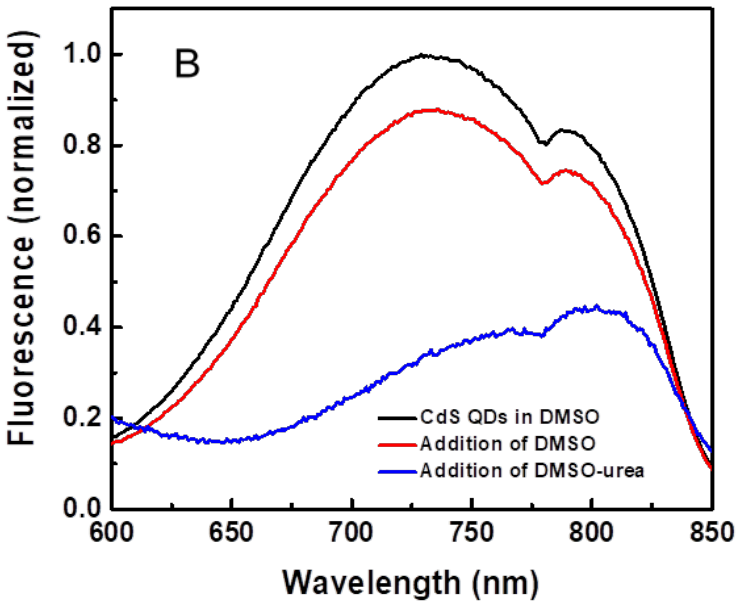

Figure 5-1. (A) Uv-vis spectrum of CdS QDs in toluene, (B) normalized fluorescence spectra of CdS QDs in DMSO and DMSO-urea. For fluorescence measurement, the initial volume of CdS QDs in DMSO solution for both DMSO addition and DMSO-urea addition is 4mL, and the addition volumes of DMSO and DMSO-urea solution are both 100 uL. The normalized fluorescence is obtained by dividing the fluorescence intensity of CdS QDs in DMSO and DMSO-urea solution by the highest fluorescence intensity of initial CdS QDs solution. The urea is dissolved in DMSO with a concentration of 2 M. The excitation wavelength is 480 nm.

5.3.2 Effect of Solvent on Electron and Hole Kinetics

Ultrafast transient spectroscopy was employed to study the effect of solvent on electrons and holes lifetime. CdS nanoparticles were deposited on TiO_2 by successive ionic layer absorption and reaction (SILAR) method on microslides. Inorganic Na_2SO_4 aqueous solution and organic DMSO were chosen as test solutions. Na_2SO_4 aqueous solution was used to dissolve urea to do the photoelectrochemical performance test in our previous research,[14] and to keep consistent, we chose solution with the same concentration of Na_2SO_4 as we used in photoelectrochemical performance test. DMSO was chosen as it is an organic solvent and can dissolve urea and is miscible with toluene, as is used in fluorescence test.

Figure 5-2 shows the transient bleach and absorption decay of CdS prepared with different SILAR cycles in different solutions. The decay kinetics of the transient bleach and absorption are fitted using linear combination of multiexponential components formula $y = \sum_i A_i e^{-t/\tau_i}$, where A_i and τ_i is amplitude and time constant of the ith component, respectively. The average time constant and corresponding rate constant for bleach and absorption decay related to electron and hole transfer and recombination can then be obtained using equation $\tau_{ave} = \sum A_i \tau_i^2 / \sum A_i \tau_i$ and $k = 1/\tau_{ave}$, respectively. Figure 5-2(A) shows the bleach decay difference of 3 SILAR cycles of CdS in vacuum, in Na_2SO_4 and in DMSO. As is shown, the bleach decays fastest in vacuum, followed by in Na_2SO_4 and decays slowest in DMSO, with a lifetime of 645.6 ps, 906.7ps and 1153.7ps, respectively. The increased lifetime of electrons in solutions can be attributed to the surface modification of solution molecules to CdS QDs. Some trap and surface states are eliminated by the solvent[23] and retard the trap-mediated recombination of electrons and holes. This result is consistent with the fluorescence in Figure 5-1 (B). The lifetime difference of electrons in Na_2SO_4 aqueous solution and in DMSO can be attributed to the different polarity, viscosity and surface passivation effect of these two solutions.[24–26] One interesting tendency noted is that in Figure 5-2(A), (B) and (C), the lifetime of electrons in vacuum increases with increased SILAR cycles of CdS, while the lifetime in Na_2SO_4 and DMSO decreases, which is shown in table 5-1. The increased lifetime in vacuum is due to the reduced grain boundaries and interfaces as well as surface states in larger size particles, which suppresses charge trapping and hence reduces the trap-mediated recombination at the particle interfaces. The decreased lifetime in solutions is attributed to different passivation effect of solutions to energy levels in CdS QDs with different size.

Figure 5-2 (D) (E) (F) show the transient absorption decay, corresponding to the deactivation of trapped holes. The transient absorption decay shows the same tendency as transient bleach decay, that is, the lifetime of holes increases with increased SILAR cycles of CdS in vacuum while decreases in Na_2SO_4 solution and DMSO, and the lifetime in solution is longer than that in vacuum for all 3, 9 and 15 cycles of CdS (table 5-1). The same lifetime change tendency of electrons and holes is because they both deactivate due to their recombination, and hence one increases or decreases the other changes accordingly.

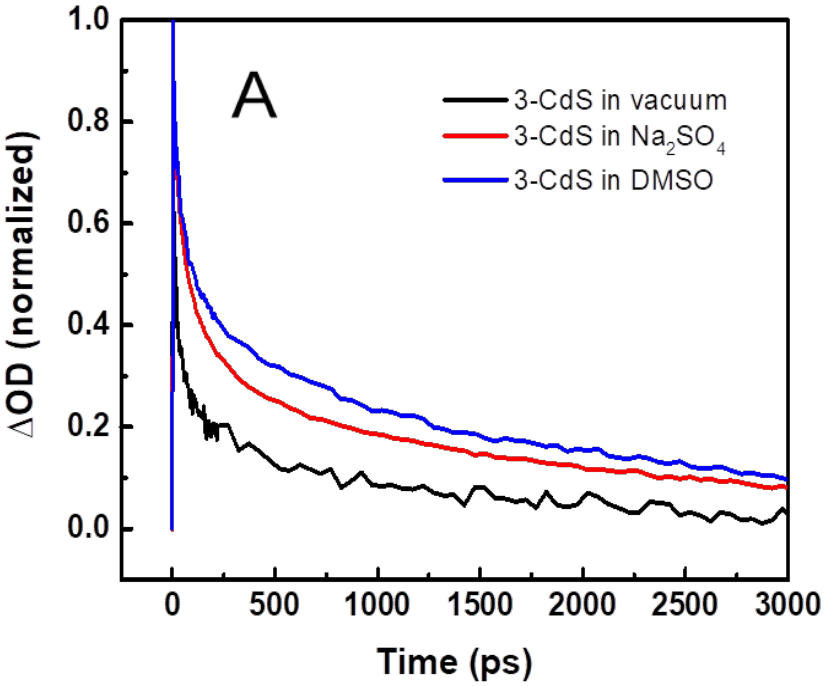

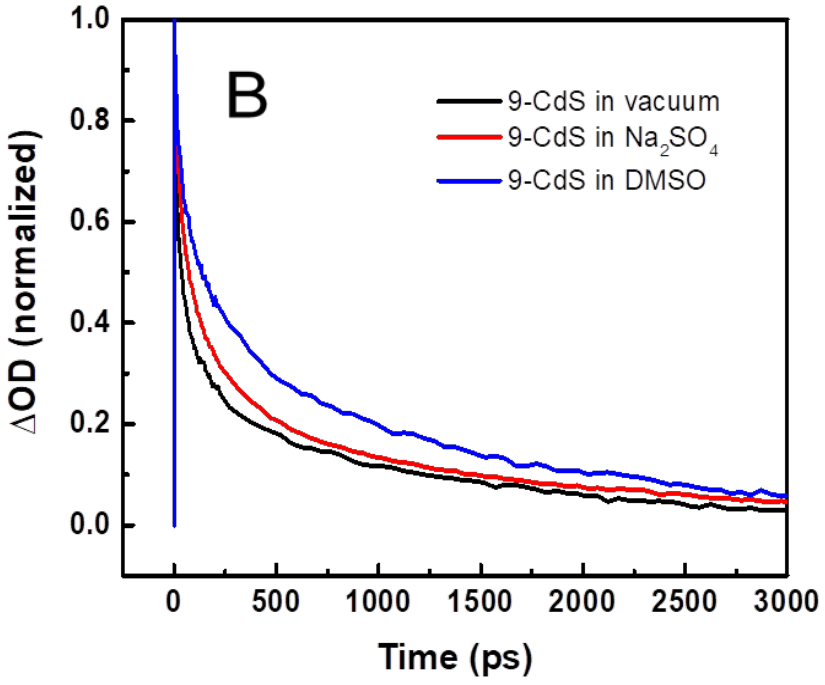
B
9-CdS in vacuum
9-CdS in Na_2SO_4
9-CdS in DMSO
ΔOD (normalized)
Time (ps)
1.0
0.8
0.6
0.4
0.2
0.0
0
500
1000
1500
2000
2500
3000

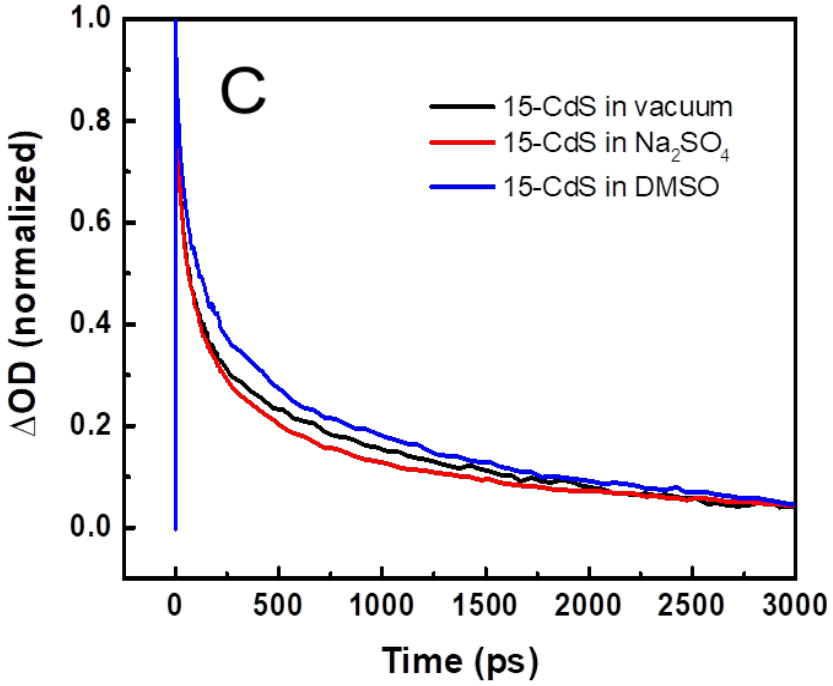
C
15-CdS in vacuum
15-CdS in Na_2SO_4
15-CdS in DMSO
ΔOD (normalized)
Time (ps)
1.0
0.8
0.6
0.4
0.2
0.0
0
500
1000
1500
2000
2500
3000

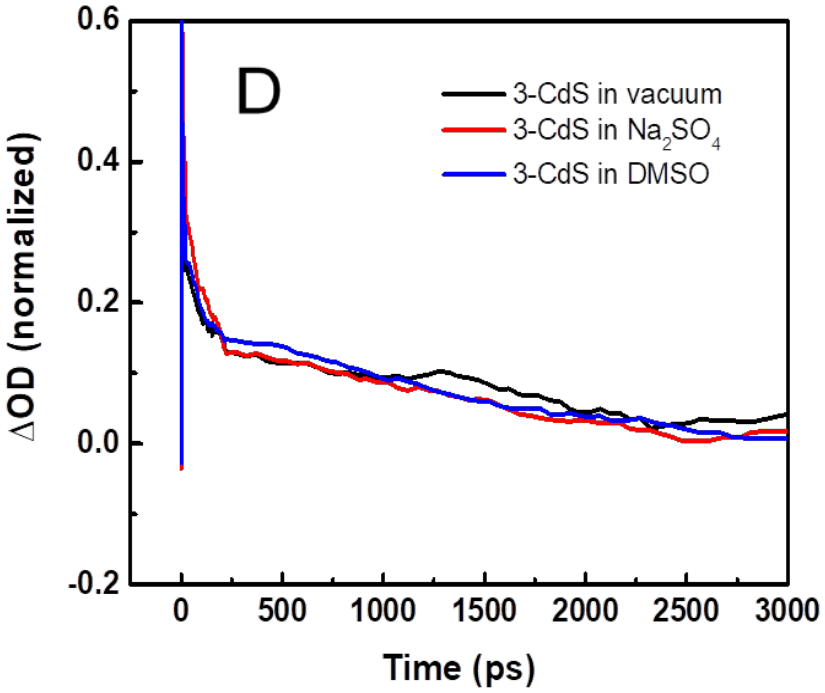
D
3-CdS in vacuum
3-CdS in Na_2SO_4
3-CdS in DMSO
ΔOD (normalized)
Time (ps)
0.6
0.4
0.2
0.0
-0.2
0
500
1000
1500
2000
2500
3000

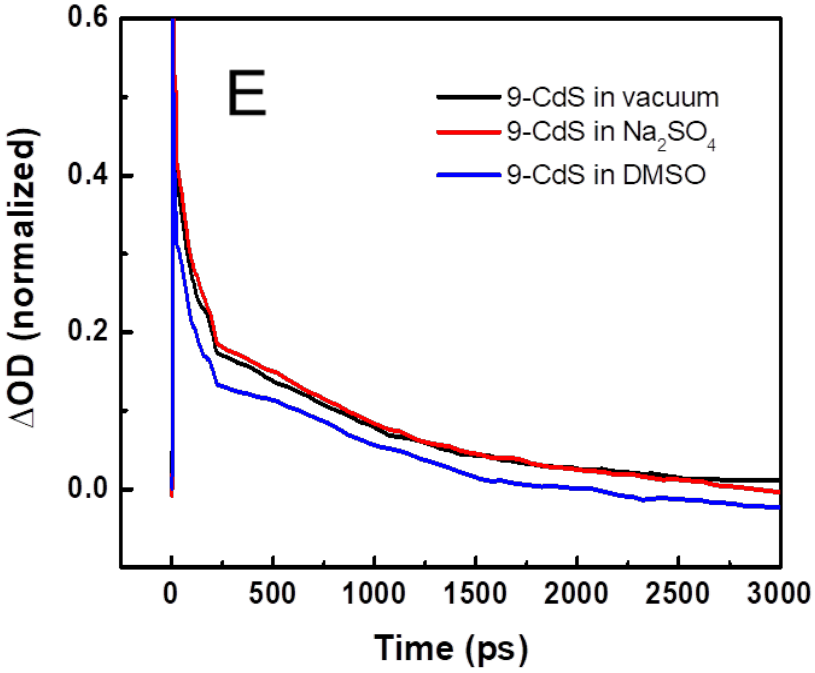
E
9-CdS in vacuum
9-CdS in Na_2SO_4
9-CdS in DMSO
ΔOD (normalized)
Time (ps)
0.6
0.4
0.2
0.0
0
500
1000
1500
2000
2500
3000

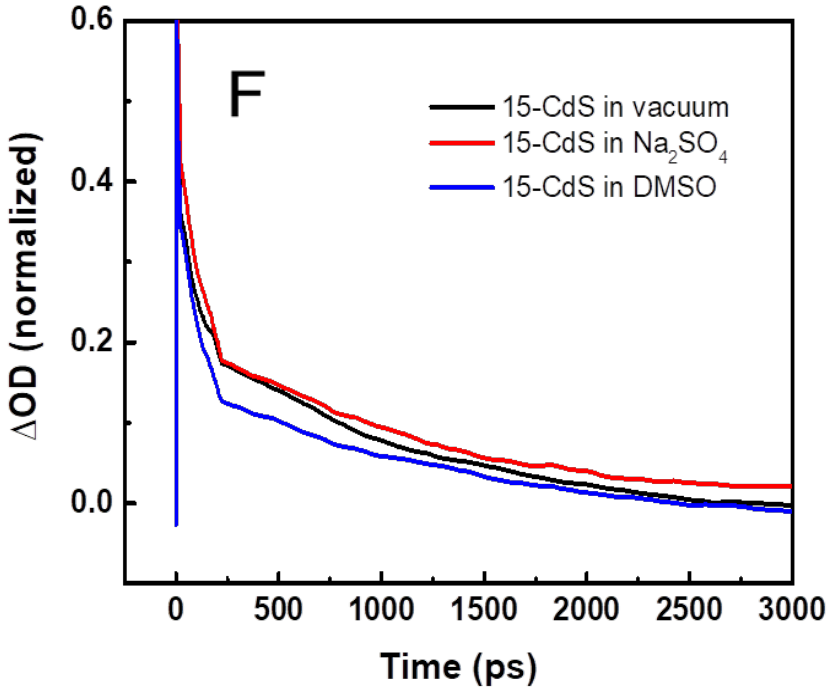

Figure 5-2. Transient bleach decay of (A) 3 cycles (B) 9 cycles and (C) 15 cycles of CdS and transient absorption decay of (D) 3 cycles (E) 9 cycles and (F) 15 cycles of CdS on microslides in vacuum, Na_2SO_4 solution and DMSO.

Table 5-1. Electrons and holes lifetime of ZrO_2-CdS in vacuum and in solutions

System	3-CdS in vac	3-CdS in Na_2SO_4	3-CdS in DMSO	9-CdS in vac	9-CdS in Na_2SO_4	9-CdS in DMSO	15-CdS in vac	15-CdS in Na_2SO_4	15-CdS In DMSO
Electrons Lifetime (ps)	645.6	906.7	1153.7	743.5	657.0	1059.8	895.1	584.8	939.2
Holes Lifetime (ps)	108.8	1136.9	1951.7	661.0	731.6	989.6	769.6	703.9	832.5

5.3.3 Hole Transfer from CdS to Urea

Figure 5-3 (A), (B) and (C) show the transient absorption decay of different SILAR cycles of CdS in Na_2SO_4 and in Na_2SO_4-urea, corresponding to the hole deactivation. As is shown, the transient absorption decays faster in Na_2SO_4-urea than in Na_2SO_4 for all 3, 9 and 15 cycles of CdS. The decay due to deactivation of holes in Na_2SO_4 is attributed to the recombination of electrons and holes, while the decay in urea-containing solution is attributed to the recombination as well as the hole transfer from CdS to urea. This result that hole transfer occurs from CdS to urea is consistent with the fluorescence result in Figure 5-1B. The hole transfer rate from CdS to urea can be obtained by calculating the difference in decay rate between in Na_2SO_4 and in Na_2SO_4-urea, that is, $k_{ht} = k_{Na2SO4-urea} - k_{Na2SO4}$, and the results are listed in table 5-3. Figure 5-3 (D), (E) and (F) show the transient absorption decay of different SILAR cycles of CdS in DMSO and in DMSO-urea. Similarly, the hole transfer from CdS to urea in DMSO-urea can be calculated by $k_{ht} = k_{DMSO-urea} - k_{DMSO}$, and the results are shown in table 5-3. From table 5-3, it is shown that hole transfer rate is faster in Na_2SO_4-urea than in DMSO-urea, which is consistent to the results obtained in table 5-3. This is because different polarities of Na_2SO_4 aqueous solution and DMSO will affect the charge distribution of the solvent molecules and urea molecules and influence the charge transfer by the redistribution of electron populations.[27]

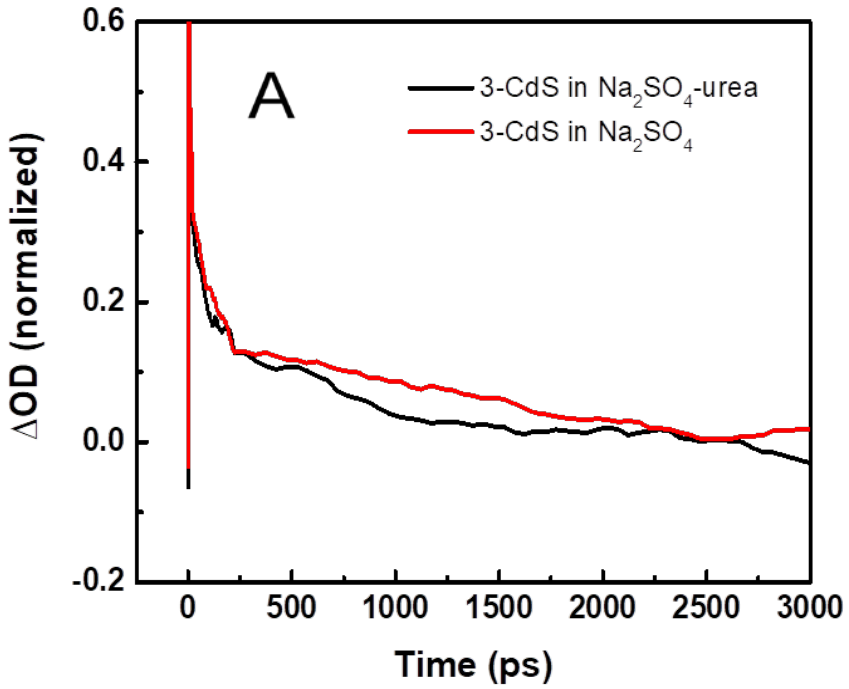
A
3-CdS in Na_2SO_4-urea
3-CdS in Na_2SO_4
ΔOD (normalized)
Time (ps)
0.6
0.4
0.2
0.0
-0.2
0
500
1000
1500
2000
2500
3000

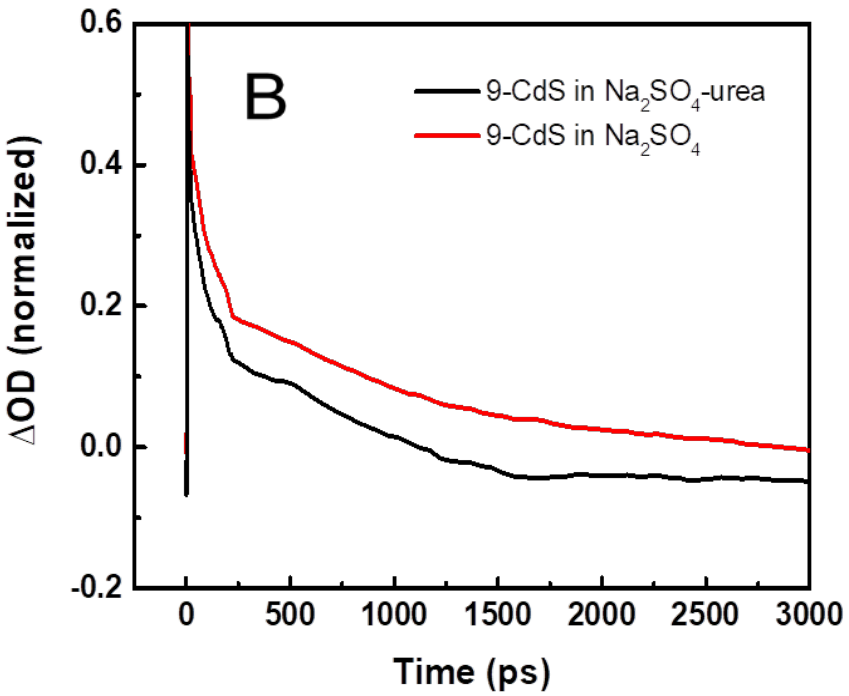
B
9-CdS in Na_2SO_4-urea
9-CdS in Na_2SO_4
ΔOD (normalized)
Time (ps)
0.6
0.4
0.2
0.0
-0.2
0
500
1000
1500
2000
2500
3000

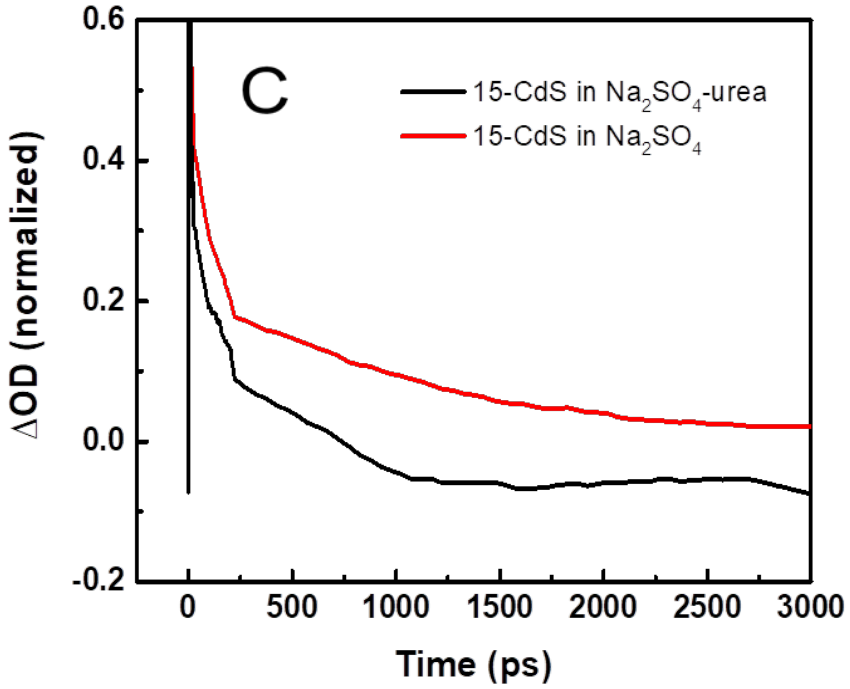
C
15-CdS in Na2SO4-urea
15-CdS in Na2SO4
ΔOD (normalized)
Time (ps)
0.6
0.4
0.2
0.0
-0.2
0
500
1000
1500
2000
2500
3000

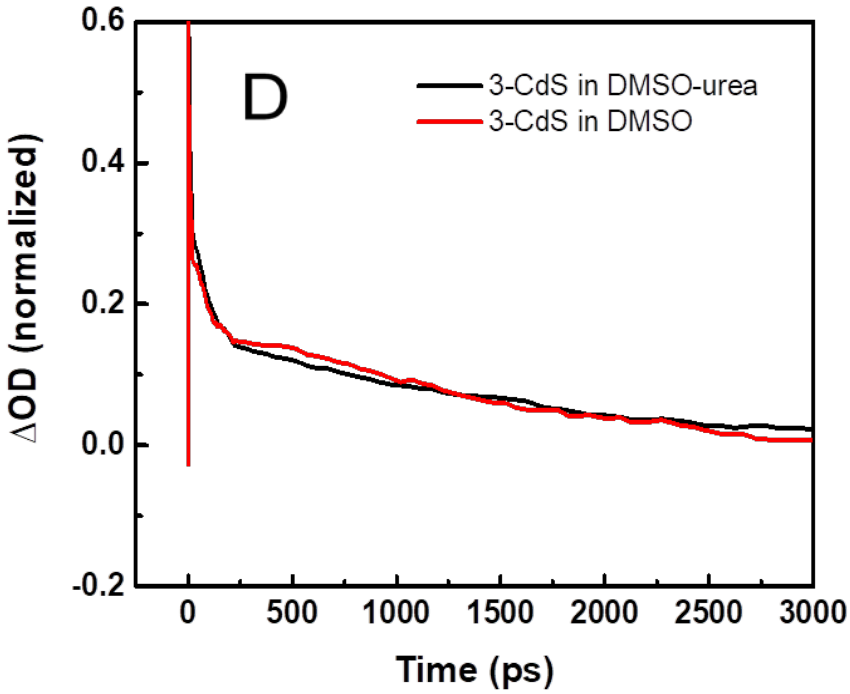
D
3-CdS in DMSO-urea
3-CdS in DMSO
ΔOD (normalized)
Time (ps)
0.6
0.4
0.2
0.0
-0.2
0
500
1000
1500
2000
2500
3000

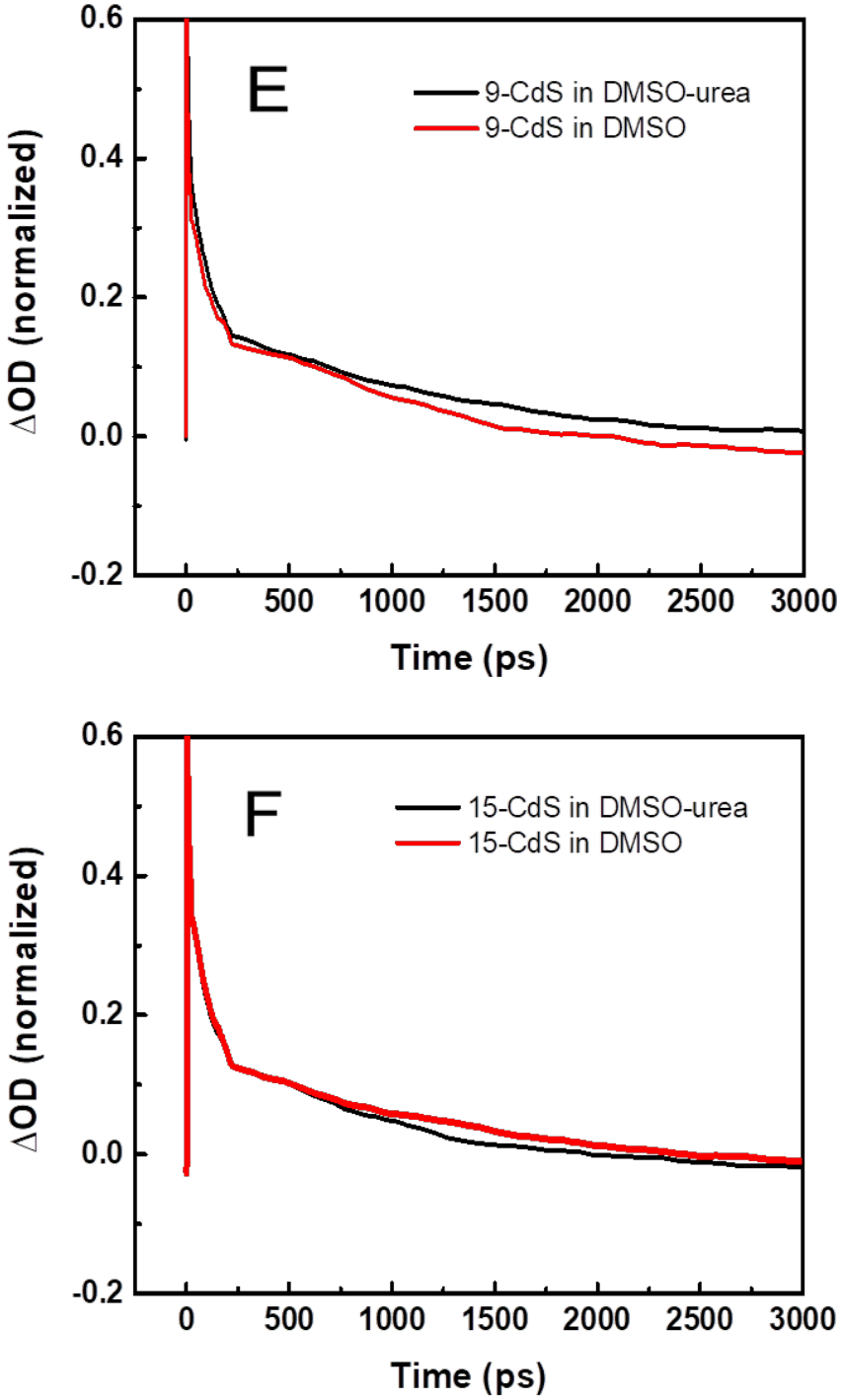

Figure 5-3. Transient absorption decay of different SILAR cycles of CdS on microslides (A) 3 cycles (B) 9 cycles and (C) 15 cycles in Na_2SO_4 and Na_2SO_4-urea and (D) 3 cycles (E) 9 cycles and (F) 15 cycles in DMSO and DMSO-urea.

Table 5-3. Hole transfer rate from CdS to urea in Na_2SO_4-urea and DMSO-urea

System	3-CdS	9-CdS	15-CdS
Rate constant (1/s) in Na_2SO_4-urea	5.4×10^8	5.6×10^8	1.2×10^9
Rate constant (1/s) in DMSO-urea	2.7×10^8	2.4×10^8	1.2×10^8

5.4 Summary

Na_2SO_4 aqueous solution and DMSO have been used as the solvent of urea to study the effect of solvents on CdS QDs charge kinetics, surface passivation of urea on CdS QDs and hole transfer properties from CdS to urea. Solvents with different polarity and viscosity affect the charge dynamics due to the surface modification of solution molecules to CdS QDs. Urea can passivate CdS QDs surface and take holes from CdS, due to the binding interaction between O atoms in urea and Cd atoms and H atoms in urea and S atoms on the CdS QD surface, as indicated in results of fluorescence and transient absorption measurement.

References

(1) Jing, L.; Kershaw, S. V.; Li, Y.; Huang, X.; Li, Y.; Rogach, A. L.; Gao, M. Aqueous Based Semiconductor Nanocrystals. *Chem. Rev.* **2016**, *116* (18), 10623–10730.

(2) Seker, F.; Meeker, K.; Kuech, T. F.; Ellis, A. B. Surface Chemistry of Prototypical Bulk II−VI and III−V Semiconductors and Implications for Chemical Sensing. *Chem. Rev.* **2000**, *100* (7), 2505–2536.

(3) Pathak, S.; Choi, S.-K.; Arnheim, N.; Thompson, M. E. Hydroxylated Quantum Dots as Luminescent Probes for in Situ Hybridization. *J. Am. Chem. Soc.* **2001**, *123* (17), 4103–4104.

(4) Peng, X.; Wilson, T. E.; Alivisatos, A. P.; Schultz, P. G. Synthesis and Isolatin of a Homodimer of Cadmium Selenide Nanocrystals. *Angew. Chem. Int. Ed. Engl.* **1997**, *36* (1–2), 145–147.

(5) Kalyuzhny, G.; Murray, R. W. Ligand Effects on Optical Properties of CdSe Nanocrystals. *J. Phys. Chem. B* **2005**, *109* (15), 7012–7021.

(6) Bullen, C.; Mulvaney, P. The Effects of Chemisorption on the Luminescence of CdSe Quantum Dots. *Langmuir* **2006**, *22* (7), 3007–3013.

(7) Munro, A. M.; Jen-La Plante, I.; Ng, M. S.; Ginger, D. S. Quantitative Study of the Effects of Surface Ligand Concentration on CdSe Nanocrystal Photoluminescence. *J. Phys. Chem. C* **2007**, *111* (17), 6220–6227.

(8) Chen, O.; Yang, Y.; Wang, T.; Wu, H.; Niu, C.; Yang, J.; Cao, Y. C. Surface-Functionalization-Dependent Optical Properties of II–VI Semiconductor Nanocrystals. *J. Am. Chem. Soc.* **2011**, *133* (43), 17504–17512.

(9) Hines, D. A.; Kamat, P. V. Quantum Dot Surface Chemistry: Ligand Effects and Electron Transfer Reactions. *J. Phys. Chem. C* **2013**, *117* (27), 14418–14426.

(10) Ko, J.-H.; Yoo, D.; Kim, Y.-H. Atomic Models for Anionic Ligand Passivation of Cation-Rich Surfaces of IV–VI, II–VI, and III–V Colloidal Quantum Dots. *Chem. Commun.* **2017**, *53* (2), 388–391.

(11) Kim, W.; Lim, S. J.; Jung, S.; Shin, S. K. Binary Amine−Phosphine Passivation of Surface Traps on CdSe Nanocrystals. *J. Phys. Chem. C* **2010**, *114* (3), 1539–1546.

(12) Meyer, G. J.; Lisensky, G. C.; Ellis, A. B. Evidence for Adduct Formation at the Semiconductor-Gas Interface. Photoluminescent Properties of Cadmium Selenide in the Presence of Amines. *J. Am. Chem. Soc.* **1988**, *110* (15), 4914–4918.

(13) Keung, A. J.; Filler, M. A.; Bent, S. F. Thermal Control of Amide Product Distributions at the Ge(100)-2×1 Surface. *J. Phys. Chem. C* **2007**, *111* (1), 411–419.

(14) Zhao, R.; Schumacher, G.; Leahy, S.; Radich, J. G. $Ni(OH)_2$ as Hole Mediator for Visible Light-Induced Urea Splitting. *J. Phys. Chem. C* **2018**, *122* (25), 13995–14003.

(15) Jasieniak, J.; Mulvaney, P. From Cd-Rich to Se-Rich − the Manipulation of CdSe Nanocrystal Surface Stoichiometry. *J. Am. Chem. Soc.* **2007**, *129* (10), 2841–2848.

(16) Underwood, D. F.; Kippeny, T.; Rosenthal, S. J. Ultrafast Carrier Dynamics in CdSe Nanocrystals Determined by Femtosecond Fluorescence Upconversion Spectroscopy. *J. Phys. Chem. B* **2001**, *105* (2), 436–443.

(17) Wang, M.; Oh, J. K.; Dykstra, T. E.; Lou, X.; Scholes, G. D.; Winnik, M. A. Surface Modification of CdSe and CdSe/ZnS Semiconductor Nanocrystals with Poly (N,N-Dimethylaminoethyl Methacrylate). *Macromolecules* **2006**, *39* (10), 3664–3672.

(18) Baker, D. R.; Kamat, P. V. Tuning the Emission of CdSe Quantum Dots by Controlled Trap Enhancement. *Langmuir* **2010**, *26* (13), 11272–11276.

(19) Pople, J. A.; Gordon, M. Molecular Orbital Theory of the Electronic Structure of Organic Compounds. I. Substituent Effects and Dipole Moments. *J. Am. Chem. Soc.* **1967**, *89* (17), 4253–4261.

(20) Mei, J.; Wang, F.; Wang, Y.; Tian, C.; Liu, H.; Zhao, D. Energy Transfer Assisted Solvent Effects on $CsPbBr_3$ Quantum Dots. *J. Mater. Chem. C* **2017**, *5* (42), 11076–11082.

(21) Chou, H.-L.; Tseng, C.-H.; Pillai, K. C.; Hwang, B.-J.; Chen, L.-Y. Adsorption and Binding of Capping Molecules for Highly Luminescent CdSe Nanocrystals – DFT Simulation Studies. *Nanoscale* **2010**, *2* (12), 2679–2684.

(22) Chou, H.-L.; Tseng, C.-H.; Pillai, K. C.; Hwang, B.-J.; Chen, L.-Y. Surface Related Emission in CdS Quantum Dots. DFT Simulation Studies. *J. Phys. Chem. C* **2011**, *115* (43), 20856–20863.

(23) Fischer, S. A.; Crotty, A. M.; Kilina, S. V.; Ivanov, S. A.; Tretiak, S. Passivating Ligand and Solvent Contributions to the Electronic Properties of Semiconductor Nanocrystals. *Nanoscale* **2012**, *4* (3), 904–914.

(24) Bhattacharyya, A.; Mukherjee, S.; Chadha, A.; Prasad, E. Diffusion of Solvent-Separated Ion Pairs Controls Back Electron Transfer Rate in Graphene Quantum Dots. *J. Phys. Chem. C* **2018**, *122* (28), 15819–15825.

(25) Barthel, E.; Martini, I.; Keszei, E.; J. Schwartz, B. Solvent Effects on the Ultrafast Dynamics and Spectroscopy of the Charge-Transfer-to-Solvent Reaction of Sodide. *J. Chem. Phys.* **2003**, *118* (13), 5916–5931.

(26) Papaioannou, N.; Marinovic, A.; Yoshizawa, N.; Goode, A. E.; Fay, M.; Khlobystov, A.; Titirici, M.-M.; Sapelkin, A. Structure and Solvents Effects on the Optical Properties of Sugar-Derived Carbon Nanodots. *Sci. Rep.* **2018**, *8* (1), 6559-6568.

(27) Ellis, J. L.; Hickstein, D. D.; Schnitzenbaumer, K. J.; Wilker, M. B.; Palm, B. B.; Jimenez, J. L.; Dukovic, G.; Kapteyn, H. C.; Murnane, M. M.; Xiong, W. Solvents Effects on Charge Transfer from Quantum Dots. *J. Am. Chem. Soc.* **2015**, *137* (11), 3759–3762.

Chapter 6 Conclusions and Future Work

6.1 Conclusions

CdS was an early candidate for solar water splitting, given its straddled conduction and valence band positions relative to the water reduction and oxidation potentials. However, the oxygen evolution reaction cannot compete with the water-mediated photocorrosion reaction of CdS at the electrode-electrolyte interface, leading to electrode disintegration and failure. Semiconductor-catalyst architecture CdS-$Ni(OH)_2$ can harness urea as sacrificial electron donor for the sustainable production of hydrogen by side-stepping the oxygen evolution reaction. CdS-$Ni(OH)_2$ architecture demonstrates proper energy alignment and rapid hole transfer from CdS to $Ni(OH)_2$ for catalyst activation.

Thin dielectric layers ZnS and SiO_2 have also been successfully deposited on CdS to reduce photocorrosion and improve performance of photoelectrodes. ZnS and SiO_2 thin layers were deposited on TiO_2-CdS photoelectrode by SILAR and sol-gel methods, respectively. The thin protective layers decreased the physical contact of CdS and the electrolyte, and hence reduced the water-mediated photocorrosion of CdS. The photocurrent stability of CdS with ZnS and SiO_2 improved 4 and 3 times respectively compared to bare CdS.

Carrier kinetics and steady-state photoelectrochemical responses of TiO_2-CdS photoelectrodes in urea are dependent on particle size of CdS. The non-radiative recombination and electron transfer rate reduced with increased size of CdS nanoparticles. The photocurrent density increased 4 times when SILAR cycles of CdS increased from 3 to 9, and then decreased

with increased size of CdS. The stability of photocurrent enhanced with increased particle size of CdS.

Solvents of urea with different polarity and viscosity affect charge kinetics of CdS. The lifetime of electrons and holes in CdS was shortest in vacuum, followed by in inorganic Na_2SO_4 and longest in organic DMSO. Hole transfer rate constant of CdS in Na_2SO_4-urea electrolyte was 10 times of that in DMSO-urea electrolyte.

6.2 Future Work

6.2.1 Quantum Confinement Effect on Hole Transfer from CdS to $Ni(OH)_2$

As the optoelectronic properties of CdS nanocrystals are strongly size-dependent, making it possible to tune the bandgap energy of CdS nanocrystals by changing the size of CdS nanocrystals. The degree of quantum confinement will affect the conduction and valence band edge positions of CdS nanocrystals. As the band position edges represent the thermodynamic driving force for electron and hole transfer, the interfacial charge transfer kinetics of CdS-$Ni(OH)_2$ will change. The valence band edges can be tuned by changing the SILAR cycles when prepare the CdS by SILAR method. The hole transfer rate of CdS of different size to $Ni(OH)_2$ can be probed by employing transient absorption spectroscopy.

6.2.2 Steady-state Photoelectrochemical Conversion of Urea to Hydrogen

The energy conversion efficiency is one of the critical performance indicators of the photoelectrochemical cell. Suppose that all the photogenerated electrons and holes are used for urea oxidation and water reduction, the overall solar-to-hydrogen efficiency is obtained by multiplying photocurrent density j_{photo} (mA/cm^2) and redox potential V_{redox} (V), and divided by incident light power P_{light} (mW/cm^2)[1], that is $STH = j_{photo}V_{redox}/P_{light}$. The incident-photon-to-carrier efficiency (IPCE), also called external quantum efficiency (EQE), is determined by

measuring the photocurrent at various excitation wavelengths $IPCE\ (\lambda) = E\ j_{photo} / P_{light}$, where E is the incident light energy in eV, j_{photo} is photocurrent density, P_{light} is the incident light power and λ is the excitation wavelength in nm.[2]

After the optimization of photoelectrodes fabrication, the steady-state conversion of urea to hydrogen will be conducted in a photoelectrochemical reactor to measure the IPCE and STH efficiencies. This reactor contains 3 parts: the photoanode, where the urea oxidation occurs; the cathode electrode Pt metal, where the water reduction occurs; and an ion exchange membrane to facilitate H^+ transfer. It will be first measured in a 3-electrode cell using Ag/AgCl as the reference electrode and Pt wire as the counter electrode to gain the photoelectrochemical performance of the working electrode. Then 2-electrode configuration will be employed to provide the most realistic photoelectrochemical reactor performance as the photocurrent under short circuit conditions relates to the charge separation in the photoanode and the overpotential of the counter electrode. The current-time, current-potential response of the electrodes, charge transfer and recombination resistances at the electrode-electrolyte interface will be measured. The H_2 generated will be gathered and measured using the gas chromatograph. The STH and IPCE of the overall process in the 2-electrode reactor will be obtained by using Equation 6-1 and 6-2.

$$STH = \frac{\Phi_{H_2} G^0_{f,\,H_2}}{P_{light}} \times 100 \qquad \text{(Equation 6-1)}$$

STH: Solar to hydrogen efficiency

Φ_{H_2} : H_2 evolution rate, mol/m^2/s

$G^0_{f,\,H_2}$: Gibbs free energy of formation of H_2, J/mol

P_{light} : Light power, W/m^2

$$IPCE = \frac{E j_{photo}}{P_{light}} \times 100$$ (Equation 6-2)

IPCE: Incident photon to current efficiency

E: Incident light energy, eV

j_{photo} : Photocurrent density, A/m^2

References

(1) Jia, J.; Seitz, L. C.; Benck, J. D.; Huo, Y.; Chen, Y.; Ng, J. W. D.; Bilir, T.; Harris, J. S.; Jaramillo, T. F. Solar Water Splitting by Photovoltaic-Electrolysis with a Solar-to-Hydrogen Efficiency over 30%. *Nat. Commun.* **2016**, *7*, 13237-13242.

(2) Kamat, P. V.; Tvrdy, K.; Baker, D. R.; Radich, J. G. Beyond Photovoltaics: Semiconductor Nanoarchitectures for Liquid-Junction Solar Cells. *Chem. Rev.* **2010**, *110* (11), 6664–6688.